



Universidad de Navarra

Facultad de Ciencias

Breath Figures Formation

José Manuel Guadarrama Cetina



Universidad de Navarra
School of Science

Breath Figures Formation

Submitted by **José Manuel Guadarrama Cetina** in partial fulfillment of the requirements for the Doctoral Degree of the University of Navarra

A handwritten signature in black ink, appearing to read "José Manuel Guadarrama Cetina".

This dissertation has been written under my supervision in the Doctoral Program in Complex Systems, and I approve its submission to the Defense Committee.

Signed on January 22, 2013

Dr. Wenceslao González-Viñas

Declaración:

Por la presente yo, **D. José Manuel Guadarrama Cetina**, declaro que esta tesis es fruto de mi propio trabajo y que en mi conocimiento, no contiene ni material previamente publicado o escrito por otra persona, ni material que sustancialmente haya formado parte de los requerimientos para obtener cualquier otro título en cualquier centro de educación superior, excepto en los lugares del texto en los que se ha hecho referencia explícita a la fuente de la información.

(I hereby declare that this submission is my own work and that, to the best of my knowledge and belief, it contains no material previously published or written by another person nor material which to a substantial extent has been accepted for the award of any other degree of the university or other institute of higher learning, except where due acknowledgment has been made in the text.)

De igual manera, autorizo al Departamento de Física y Matemática Aplicada de la Universidad de Navarra, la distribución de esta tesis y, si procede, de la "fe de erratas" correspondiente por cualquier medio, sin perjuicio de los derechos de propiedad intelectual que me corresponden.

Signed on January 22, 2013



José Manuel Guadarrama Cetina

© José Manuel Guadarrama Cetina

Derechos de edición, divulgación y publicación:

© Departamento de Física y Matemática Aplicada, Universidad de Navarra

A Dalia y Vladimir

Acknowledgements

Agradezco a mi esposa Dalia por haber aceptado este difícil reto y por haberme apoyado y acompañado todo este tiempo desde la distancia.

Agradezco a mi director de tesis Prof. Dr. Wenceslao González-Viñas por confiar en mi capacidad para la realización de la tesis, por sus finas atenciones durante estos casi cuatro años en España y su buen juicio en su dirección. A la Universidad de Navarra por recibirme y ofrecerme un espacio para realizar mi proyecto de tesis doctoral. A la beca de Asociación de Amigos por todo el apoyo brindado durante este periodo de formación tan importante. Al Profesor Dr. Javier Burguete y a los profesores e investigadores del Departamento de Física y Matemática Aplicada. En especial al Dr. Diego Maza de esta misma institución por la ayuda prestada en la realización de las fotografías que aparecen en las Figuras 4.23 a 4.25. Al Gobierno español (FIS2008-01126, FIS2011-24642) y al de Navarra por la financiación parcial de los proyectos en los que esta inscrita esta tesis.

My cordial thanks to Dr. Ramchandra Narhe for his huge collaboration and his advices on this thesis work.

My cordial thanks to Prof. Dr. Daniel Beysens and Prof. Dr. Anne Mongruel for the opportunity to work at the ESPCI-Paristech and all the rich discussion that have until now maintained.

Agradezco al Profesor Gerardo Ruiz por el apoyo recibido durante las estancias realizadas en el Taller de Fluidos de la Facultad de Ciencias de la UNAM, México. También agradezco a Sergio Hernández Zapata por su apoyo en el laboratorio.

Agradezco también a mis compañeros doctorandos y colegas: Ana, Celia, Raheema, Neus, Sara, Hugo, Iván, Manuel, Miguel, Moorthi, por las largas horas de discusión compañerismo.

Agradezco el enorme apoyo moral de mis padres y hermanas ya que sin ellos, no me hubiera sido posible concretar este proyecto. En especial, quiero agradecer a mi hermana Lourdes y a su esposo Mark Zalcik por su ayuda prestada durante la realización de esta tesis.

Agradezco a mi compañero de piso Sachi por hacerme la vida fácil en la ciudad de Pamplona.

Contents

Preface	xii
1. Breath Figures	1
1.1. Introduction	1
1.2. Stages in the Dynamics of Breath Figures	2
1.3. The Nucleation Stage	3
1.3.1. Homogeneous Nucleation	3
1.3.2. Heterogeneous Nucleation	5
1.4. The Intermediate Stage	6
1.5. The Coalescence Stage	9
1.5.1. The Scaling Laws	10
1.6. Another Model of BF Dynamics	11
2. Experimental Device and Tools for Image Analysis	13
2.1. Experimental Device	13
2.1.1. Description of the Condensation Chamber	13
2.2. Substrates, Substances, and Treatments	15
2.2.1. Physical Properties Values	17
2.3. Tools for Image Analysis	18
2.3.1. Acquisition of Images	18
2.3.2. The Threshold Problem	19
2.4. Errors	21
2.4.1. The Error of Calculations with Matlab.	24
2.4.2. The Error of Calculations with ImageJ.	24
3. Breath Figures in Presence of a Humidity Sink	27
3.1. Introduction	28
3.2. Experimental Procedure	29
3.2.1. Image Analysis	30
3.2.2. Integration Procedure for $\langle r \rangle$	31
3.3. The Humidity Sink and the Depletion Zone	33
3.3.1. The Flux and the Depletion Zone	39
3.3.2. The Difference of Pressure around the Salty Drop	40
3.4. Drops Pattern Around the Humidity Sink	43

3.4.1. Mean Radius of the BF's Droplets	45
3.5. The Profile of the Pressure Gradient	47
3.6. Concluding Remarks	50
4. Breath Figure under Solidification Temperature of Water	53
4.1. Introduction	54
4.2. Experimental Set Up and Procedures	55
4.3. Observations	55
4.4. A Salty Drop under Solidification Temperature of Water: Anisotropy on the Pressure Gradient.	61
4.5. A Model of Ice Propagation	65
4.5.1. Percolation	65
4.6. Summary and Concluding Remarks	66
5. Two Immiscible Substances Condensing on a Cold Surface	79
5.1. Introduction	79
5.2. Experimental Procedure and General Observations	80
5.2.1. First Experiment: Single Vapor Condensation	81
5.2.2. Second Experiment: Condensing one Vapor at once	82
5.2.3. Third Experiment: Condensing Two Vapors Simultaneously	83
5.3. Results	83
5.4. Summary and Concluding Remarks	102
Conclusions and Outlook	103
A. Appendix 1: Program Routines	105
A.1. Pre-analysis routines: Conversion PPM - JPEG	105
A.2. Salty-drop Analysis	108
B. Appendix 2: Characterization of the Condensation Chamber	119
B.1. Characterization	119
C. Appendix 3: HVAC Diagram	123
Bibliography	125
Summary	129
Resumen	130

Preface

Objectives

The general objective of this work is to study the dynamics of water vapor condensation over hydrophobic substrates in different conditions. Those conditions are: the presence of water vapor sink, the lower temperature of solidification and a condensable but immiscible vapors. In particular, the goal to start those studies was to build and provide an accurate image tool analysis based in Matlab, Fortran and Octave routines. Concerning the water vapor condensation in presence of a humidity sink, the goals were to describe the increment of water volume of the humidity sink, the depletion zone formed around the sink [1]. Also the vapor pressure as a function of water concentration on pattern outside of the depletion zone. We discovered a new process of ice propagation [2] and the objective is to understand the phenomenon of propagation. For the case of immiscible condensable vapors, the objective is to describe the dynamics of the drop wise production and the aggregation of the two substances process into clusters [3].

The Breath Figures

Actually, my interest in Breath Figures arose when I received a positive answer from University of Navarra to do my studies of PhD in complex systems. In addition, the idea of work with thermodynamics calculations was enough to focus all my interest. The first time I have known something of this phenomenon was after the shower, I stood in front the mirror to see the carpet of the small droplets produced by the fog. I was trying to figure out how, when, where, and what the difficulties could be on the study of such natural process. Of course, those thoughts were due to the lack of experience. Three years after, my opinion at that respect have changed. When I see a steamed mirror or a window, now I am trying to figure out what contact angle could it be.

This work is far from the assessments of thermodynamics, but it is fully formed of non linear dynamics. Elsewhere in this work of thesis when I refer to Breath Figures (BF), I am referring to water vapor condensing drop wise over a cold surface, and cold means the surface is kept at lower temperature than the environment. I will remark the difference when I am talking about other vapor substance different than water. Henceforth, Breath Figure will be (BF) and will be exclusively for water vapor. The BF formation has three stages: 1) nucleation, 2) growth of droplets only by condensation and no more nucleation appears, and 3) where coalescence events rules the behavior of the dynamics and some time after, the growth, the renucleation of new droplets which grow by condensation appear. Very good researches have done theory of high level also, they have established the basis to describe a wide range of experimental observations. In

addition, this work exhibits new design of configurations where is indispensable to apply many resources of complex systems theory to explain the observations.

Context

The study of BF started in 1893 by the meteorologist J. Aitken [4, 5], and in 1911 by John William Strutt (Lord Rayleigh) [6] "After breathing on a window-pane we wrote our names on the glass with the point of a finger. Now rater having waited until the moist deposit have disappeared, and again breathing on the glass, the written characters became quite legible". Perhaps this was the first experiment related with hydrophobic surfaces and Breath Figure with following conclusion "This seems quite to agree with Lord Rayleigh's explanation, grease on the fingers causing the phenomenon." At that time, to publish in Nature Journal appeared not to be so complicated. However the really important issue to highlight is the fact that some serious researches have begun to ask to themselves about what variables could be involved in this phenomenon. Other interesting antecedent appeared in 1913 by John Aitken. He has explained an experiment on surfaces carefully treated [7]. Nowadays, because huge efforts of many people, some applications have been developed and technology of physical vapor deposition and also technology of water vapor around its behavior.

Scope

The Breath Figure production is by itself an irreversible thermodynamic phenomenon outside of equilibrium. However, I am not handling my measurement and my analysis to give a thermodynamic perspective. It is affordable of course but, to use the increment of the size of the droplets, the variations of the temperature, as well, the boundaries conditions values of supersaturation pressure. With all these information we try to describe the growth and its time evolution with meaning depth into the complexity of this phenomenon. The experiment features can fit on chemistry, physical chemistry, engineering applications, physics theory, simulations, or farthermost pure mathematics. The main feature of this work is the application of dynamics to provide descriptions of liquid-solid interface interactions.

Some questions have arisen when the BF about the gradient vapor pressure distribution on the vapor atmosphere close to the BF when interacts with a humidity sink. From the experimental observations, we have carefully proceeded the image analysis in order to obtain geometric measurements from the phenomenon. The values of partial pressures which are very difficult to measure or detect, can be revealed by such analysis and throw diffusive equation. The low dispersion on data let us to work with fittings and more imaginative and bold models. A new configurations let us to observe and report a non discovered process on frost formation. The properties of the evolution BF's patterns under freezing water's temperature at standard conditions lead us to observe ice propagation as percolation process. This occurs when the three water phases interact in small region. In other experiments (to following the logic stream) the humidity sink is tested under frost phenomenon's conditions to observe and afterward discover the anisotropy of patterns can affect directly the salty drop's growth.

It is a high priority to understand the mechanism of mixing two immiscible substances through

the population analysis of BF and condensation of other substance in the same cold surface from image data. This phenomenology is very rich, because the population of droplets are sensitive to heterogeneity or homogeneity on the spatial distributions. Actually, the coalescence's theory is very powerful and helpful to give ground to non classical growth's laws and the complexity behavior less studied on the specialized literature. Some theoretical already obtained results can explain our own experimental observations. I am very confident on that theory with their scaling laws and distributions functions help to understand the behavior and the tendencies. However not all discoveries match with those results, and is where I am confident on my own observations and measurements and, the wide possibilities to explain facts. With the philosophy "the nature has the last word overall cases", I will to emphasize this study with only direct observations. I will use the theory always to compare and to understand, and sometimes as a starting point of analysis. Nevertheless, for some experiments, the results will not agree with theoreticians and their calculations.

Outline

Concepts that belong to undergraduate level are left outside of this dissertation. There are excellent bibliography almost anywhere. Instead, I pass directly to the substantial concepts. Each chapter of this thesis work are thought in order to stand alone, and each one provides enough information of the experiments, as well, as the theory used on the study.

In the introductory chapter 1, I display the content of general physics theory of Breath Figures and I give a retrospective highlighted the results provided by the models and previous experiments. In Chapter 2, I do the description of the experimental device used in this research. In the same Chapter is signalized the troubleshooting on image analysis to extract a good (in statistical way) amount of data. In Chapter 3, I give the physical description of experiment when a BF is evolving in presence of a humidity sink. I use a simple model of flux to try to explain the depletion zone around a salty drop. I report interesting results about the values of vapor partial pressure obtained from direct measurements. In chapter 4, I report observations of a new discover process on frost formation observed during a stage at the ESPCI-Paristech in Paris, France. When a BF is produced over a surface at below temperature of solidification of water ($-9\text{ }^{\circ}\text{C}$). The water droplets condensed are in a metastable phase of supercooled and by some perturbation a phase transition occurs. The relevant observation is the percolation mechanism of ice propagation. As well, evaporation of liquid droplets and vapor deposition are observed too. In Chapter 5, I report experimental result when the vapor of two immiscible substances condense on the same repellent surface. The measurements of the average radii and the coverage of the drops for each one evolve with non classical growth laws. This situation is explained on the basis frame of scaling universal relations.

Chapter 1

Breath Figures



Figure 1.1: *Breath Figures on my window in a cold morning.*

1.1. Introduction

The phenomenon of Breath Figures (BF) is commonly found in nature and in our daily life. It occurs when water vapor (WV) condenses as a dropwise process on a cold surface. When we grab a bottle of some cold beverage out of the fridge in a hot day, we will immediately notice that small droplets cover the surface of the glass. Another example is when we try to observe ourselves in the mirror of the bathroom after taking a shower. The mirror will be covered with "fog". Physically, factors like the difference of the saturation pressures and the difference of the temperatures between the water vapor and the glass can produce the transition onto liquid phase. The next sections of this chapter are dedicated to explain the BF production. Theories, simulations, and experiments have been done since the beginning of the 20th century. Nowadays, solid-liquid interaction has been taking a rising interest in the discussion of this complex world of BF's patterns. The content written in this section is a compilation of those relevant studies. In this chapter, the theory will provide the basis of understanding to obtain new results. Beyond the theory described, other concepts will be cited and discussed later on.

1.2. Stages in the Dynamics of Breath Figures

The properties of the surfaces play an important role in the formation of films and patterns. Such properties are the surface dimension (can be modified) and the contact angle achieved at the interface solid-liquid. The surface hydrophobicity ($\theta_c > 90^\circ$) depends on the coatings, the micro or nanometric etched patterns. The properties of wetting will also change if instead of a surface, it is a porous medium, or a wire, like a spider web. As we will see, the phenomenon develops in three general stages. There are exhaustive researches based on experiments and simulations since 1973 [8]. Those observations are affordable to develop in laboratory. I will not be the exception here, all experiments reported in this work are related to the two stages of BF. I will give a summary of what happens with those stages in a sequential order.

- 1. Nucleation stage.** There are two kind of nucleation processes: homogeneous and heterogeneous. The heterogeneous nucleation concept is fundamental to understand the formation of dew. Now, it is considered the vapor at partial pressure P_{ss} , which is larger than its saturation pressure. It means that the vapor is in a metastable state and it will condense into liquid phase, which is the state of minimum energy. The formation of liquid drops starts by thermal fluctuations with the formation of thermodynamically stable small nuclei. The small formed droplets are more stable than the water vapor and they do not evaporate. The difference of temperatures between the supersaturated and the saturated vapor boosts the system to pass an energy barrier and the water vapor condenses. The free energy ΔG for spheric droplets can be written as [9]

$$\Delta G = -\frac{4}{3}\pi r^3 \rho \frac{RT}{\mu_v} \log\left(\frac{P_s}{P_{ss}}\right) + 4\pi r^2 \gamma \quad (1.1)$$

where r , ρ , R , and T are the cluster radius, density, the gas constant and the temperature define the change on volumetric energy required for the phase transition, μ_v , P_s , P_{ss} and γ are the molar mass, the partial pressures of saturation and supersaturation, and the surface tension at the liquid vapor interface.

- 2. Growth stage.** Here, all the nucleation sites have been occupied. The clusters formed during the first stage, have formed drops. The new droplets will adsorb vapor on their vicinity because of the difference of pressures with the atmosphere. The small droplets grow without direct interaction (physical contact) among them and this is another characteristic of the second stage of BF. The classical growth law¹ for the average radius is [10],

$$\langle r \rangle \sim t^{1/3} \quad (1.2)$$

- 3. Coalescence stage.** The third stage is governed by drop coalescence events. The main characteristic is the self similar behavior. The drop's law of growth is proportional with t . When droplets reach a certain size r , they start to interact with each others. They coalesce and give away new droplets with new size [11],

$$r = (r_1^D + r_2^D)^{1/D} \quad (1.3)$$

¹In Chapter 5 an experimental study of BF pattern with different growth law is included.

where D is the drop dimension (usually three) and their mass center is the geometrical mass center of two droplets. This is not totally true since it is possible to observe the coalescence of more than two drops during the experiments. Even non spheric shape droplets can be observed. In spite of this, the data analysis of many simulations and experimental observations fit very well with this assumption. After the coalescence of two drops, there is space released on the surface and a new BF could form among the bare spaces. The surface occupation factor $\epsilon^2 = (2\langle r \rangle / \langle a \rangle)^2$ behaves asymptotically towards a constant 0.55. That means, that the distance distribution of droplets is $(0.55\langle a \rangle)^{1/2} = 2\langle r \rangle \approx \bar{d}$

Another interesting proposal exists to describe the BF evolution such that, it is necessary to include a fourth stage for long times [12]: after long times, many generations of droplets coexist in this stage. The next section is a concise review of the nucleation process.

1.3. The Nucleation Stage

There are two types of nucleation²: the heterogeneous and the homogeneous nucleation. The BF is an example of heterogeneous nucleation because the WV molecules nucleate on specific sites on the substrate. The difference of pressures produces the impinging of the water molecules which stick and aggregate on preferential sites. Concerning the homogeneous nucleation, the process is totally different because there are not preferable sites to form the bulk.

1.3.1. Homogeneous Nucleation

Joseph Katz [13] has explained that homogeneous nucleation refers to the spontaneous creation of a new phase³. The phase change may come from a parent metastable phase. Another interesting example is the solidification of supercooled water. On this topic, A. Saito et al [14] and Tsutomu Hozumi et al [15] have done research about this kind of nucleation. The solidification is also observed in colloidal suspensions [16] and in the globular formation of proteins by hydrodynamic mechanisms [17]. The homogeneous nucleation occurs within the supersaturated phase (gas, liquid or solid) by the growth of embryos that have crossed a critical size. The size of those embryos can achieve their super-critical size because of the impingement of monomers. A stationary condition is assumed in order to explain that the reaction can occur at equilibrium concentration. In this reaction the embryos and the monomers from the parent phase stay at the same temperature. In classical theory of nucleation, the phenomenon can be interpreted with help of thermodynamics and statistical physics.

$$\Delta G = \Delta G(\text{phase change}) + \Delta G(\text{surface tension}) \quad (1.4)$$

If we consider the simplest case for vapor condensation, the partial pressure and the supersaturation pressure provide boundary conditions for the nucleation process. The radii of clusters and their surface energy can be determined by the free energy (Equation 1.1) which behaves as a monotonically increasing function when $(P_s/P_{ss}) < 1$. The vapor pressure under saturated condition is lower than the vapor pressure at supersaturated condition. If $(P_s/P_{ss}) > 1$, condensation

²The analysis of nucleation process along the thesis work is not used because it is not in the goals and in the perspective of this work. Withal, it is important to do a review to understand what the phenomenon of Breath Figures is.

³This refers under the supersaturation condition.

occurs. The initial increment of the cluster energy is due to the large value of the surface term. When the clusters begin to increase this value becomes less important and the phase change is imminent. The maximal free energy drives clusters to reach a critical radius r^* [18],

$$r^* = [2\sigma u_v] / \left[\rho R T \ln \left(\frac{P_v}{P_\infty} \right) \right], \quad (1.5)$$

and this last (Equation 1.5) is known as Kelvin's equation[16].

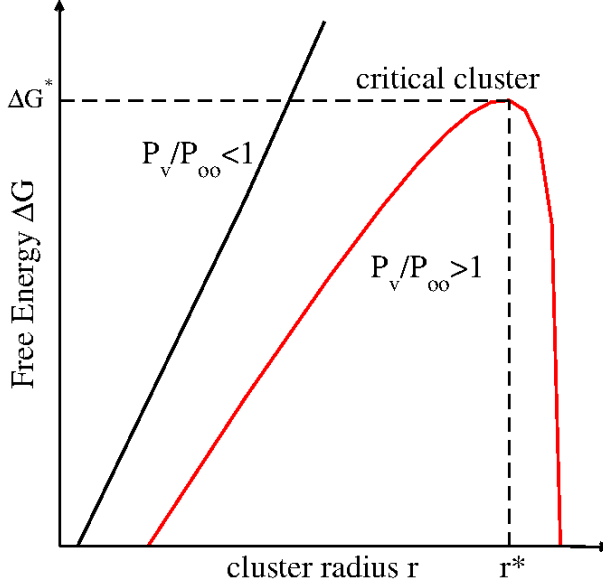
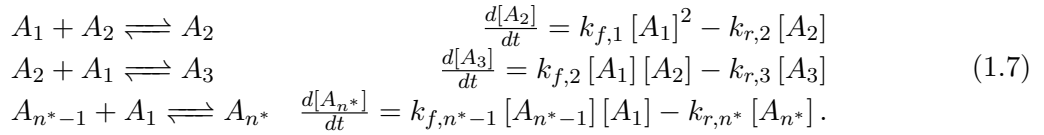


Figure 1.2: A phase transition takes place when the ratio between the pressures is $(P_s/P_{ss}) > 1$. For free energy, the relevance of the surface energy factor diminishes and the ratio of partial pressure and supersaturation pressure term increase due to the critical size, hence r is reached by the system.

The concentration $n^*(i)$ of embryos of size r^* may be defined as follow:

$$n^*(i) = n(1) \exp(-\Delta G(i)/kT), \quad (1.6)$$

where $n(1)$ is the concentration of the monomers, i is the number of clusters of size r^* in the parent phase and $\Delta G(i)$ is the Gibbs free energy of formation of an embryo. The embryos can be considered as a result of the molecular reactions where A_i, \dots, A_{n^*} are the clusters involved on the reactions, $k_{f,1}, \dots, k_{f,n}$ are the monomers addition rates, $k_{r,1}, \dots, k_{r,n^*}$ are the monomers loss rate and t the time [16]. These reactions can be written as,



The free energy depends on the ratio of the pressures for the cases where $P_v < P_\infty$ and $P_v > P_\infty$ in (Figure 1.2). Homogeneous nucleation can be found on the initial stage of the frost formation

process (This can be linked to the topic of solidification of supercooled water in Chapter 4). In meteorology, the clouds formation is a remarkable example of homogeneous nucleation because all above conditions are present. In clouds, the phases of vapor, liquid and solid may coexist. This means the cloud's system presents activity when the liquid phase transforms into solid and the vapor phase transforms into liquid. This process is called WBF since it was discovered by Wegener, Bergeron, and Findeisen [19].

1.3.2. Heterogeneous Nucleation

Heterogeneous nucleation models require the establishment of embryos population at the equilibrium of concentration of embryos and monomers in specific sites. The nucleation occurs on liquids or solids that are in contact with surfaces or particles. The condensation and the diffusive events are understood as the monomers' aggregation to big molecules occupying a surface. Some interesting observations of the heterogeneous nucleation stage have been performed through electron microscopy [20, 21]. In those references, the authors describe the nucleation by the Gibbs energy as a function of the surface tension and geometric parameters (Equation 1.8 and Figure 1.3). The observations were done over superhydrophobic's surface tension, low pressures (~ 100 Pa) and a temperature of -13 °C.

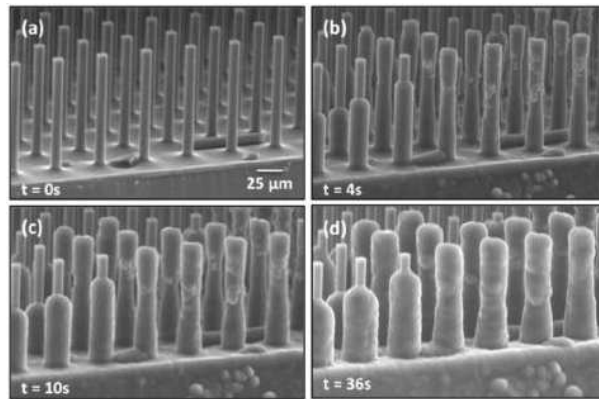


Figure 1.3: Taken from K. Varanasi, et al [21]. ESEM images of frost formation on a superhydrophobic surface. The authors show the stages of frost formation on the pillars. The superhydrophobic surfaces commonly are micro (or nano) patterned surfaces.

$$\Delta G = \pi \sigma_{IV} r^{*2} (2 - 3 \cos \theta + \cos^3 \theta) / 3 \quad (1.8)$$

where r^* is the critical radius and σ_{IV} is the liquid-vapor surface energy. Hence, the nucleation rate is

$$J = J_0 \exp(-\Delta G/kT). \quad (1.9)$$

The Gibbs energy establishes the conditions of surfaces energies for the deposition process (gas-solid phase transition).

To summarize, the definition of homogeneous nucleation can be applied when there are not preferential nucleation sites for condensation. Otherwise, the heterogeneous nucleation is affordable to study the phase transition when embryos are around.

Concerning the BF, the radius of a droplet r_s in the nucleation stage is much smaller than its distance neighbors r_d . The new droplets collect vapor from the surroundings by surface diffusion. This reduces the molecular concentration of the vapor. Thus, the droplets form an inhibition region where no more nuclei of condensation can be found, so no new droplets appear there.

1.4. The Intermediate Stage

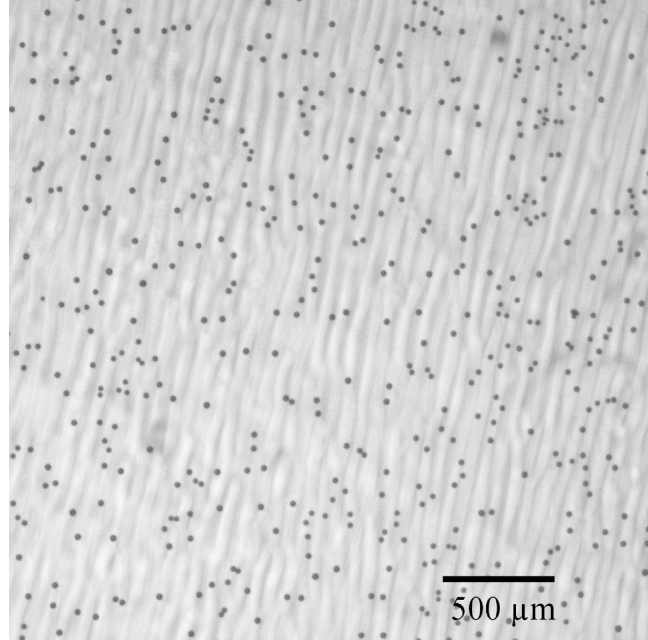


Figure 1.4: This picture corresponds to a BF in the growth stage. The BF pattern appears just 10 seconds after a constant flux of water vapor at room temperature has flown over the surface at 5 °C. The contact angle is about 92°.

The nucleation process is very important for experimentalists and theorists, because it lets us to understand further stages of evolution of the BF. Once the first cluster stable of molecules is formed on the surface, it follows a transient stage of the system. The growth of the droplets is done at expenses of the monomers surrounding the recently nucleated drops. A. Steyer, D. Beysens and C. M. Knobler [22] proposed a diffusive model that could be set out in a very convenient way to understand what happens on the intermediate stage. The model studies the flux of monomers, in particular for condensing water vapor into an isolated droplet. Several interesting investigations have done about how a single droplet grows by condensation. J. D. Ford in 1973 proposed an experiment of an isolated pending droplet that grows because a difference on the temperatures between the droplet and the heated water vapor has flown [23]. Assuming that the droplets are perfect spheres and that the process of vapor condensation is an unsteady state, the change of temperature depends on the radius of the droplet as

$$\frac{\partial T}{\partial t} = \alpha \left(\frac{\partial^2 T}{\partial r^2} + \frac{2}{r} \frac{\partial T}{\partial r} \right) \quad (1.10)$$

with the boundary conditions $T(r, 0) = T_b$ for $r \ll R$ (the initial radius $r \neq 0$) of the droplet. $T(R, t) = T_s$ $t > 0$, where T_s is the saturation temperature and $\frac{\partial T}{\partial r} = 0$ when $r = 0$ (for symmetry). The authors have considered the heat flux at the condition $r = R$ in order to solve the Equation 1.10 by an approximation. The balance equation for heat at the interface liquid-vapor is

$$k \left(\frac{\partial T}{\partial r} \right)_{r=R} = \lambda \rho \frac{dR}{dt}. \quad (1.11)$$

The Equation 1.11 is valid only at the singularity defined by the vapor-liquid interface. This assumption is necessary to solve the problem of growth as a function of the temperature T . This is very interesting because, there is no assumption of molecules concentration at any place. The formal solution for T is

$$T = T_s + (T_s - T_i) \frac{2R}{\pi r} \sum_{n=1}^{\infty} \frac{(-1)^n}{n} \sin \frac{n\pi r}{R} \exp \left\{ -n^2 \pi^2 \frac{\alpha t}{R^2} \right\}. \quad (1.12)$$

Solving the Equation 1.11, and applying Equation 1.12, at $t = 0$ and $R = R_i$ it has been found the ratio $\frac{R}{R_i} \sim 1 + (1 - \exp f(t))^{1/2}$, where $f(t)$ is the exponential function for $n = 1$. For $t \rightarrow \infty$, the ratio $\frac{R}{R_i} \sim \left(1 + C_p \frac{T_s - T_i}{\lambda} \right)^{1/3}$ describes the growth of an isolated drop pendant on air and surrounded by vapor. This article [23] provides several experimental data of testing initial radii and several differences of temperature. Another interesting investigation about the case when an isolated drop settled on a surface and surrounded by vapor is given by Sokouler [24] the condensation of a single drop can be treated as an inverted evaporation process. The growth law for that drop should be $V \propto t^{3/2}$ without the effects of convection. In this case, the assumptions require an environment of oversaturate constant vapor source, and volume relations require the dependence on the spacing between the drops. When the reservoir of vapor is placed at a distance similar to the mean drop separation d , in a steady state, the vapor flux through any area parallel to the surface. The change of volume is,

$$\frac{dV}{dt} = J_0 V_m \bar{d}^2 \quad (1.13)$$

where V_m is the molar flux, \bar{d}^2 is the mean square distance of the droplets. This agrees with D. Beysens [25] who describes the growth of a drop's carpet by surface diffusion. However, when he considers an isolated drop, the Equation 1.14 describes the flux for certain radius outside the drop.

$$2\pi \frac{d(r^2 J_r)}{dr} = 0 \Rightarrow \frac{dJ_r}{J_r} = -2 \frac{a}{r} dr. \quad (1.14)$$

Here J_r is the total vapor flux, a is the radius of the droplet, and r is a radius whose starting coordinate coincides with the center of the drop and its magnitude is comparable to \bar{d} . The essential idea is to set drop's volume rate of change as a function of the vapor flux per unit of area, but first, it is necessary to apply the relation of flux J_r on the Fick's diffusion relation $\vec{J} = -D \nabla C$ to obtain

$$J_r = J_0 \left(\frac{a}{r^2} \right) \Big|_a^b = D \frac{a}{r^2} (C_a - C_\infty), \quad (1.15)$$

where J_0 is the flux at the drop surface on a radial geometry a , C_∞ and $C_a < C_\infty$ is the relation of bulk concentration near and far from the drop. Again, the change of drop's volume is analyzed at the gas-liquid interface.

$$\frac{dV}{dt} = \int J_r dA, \quad (1.16)$$

then,

$$V = \eta \left[\frac{4\pi DM}{3\rho RT} (P_\infty - P_a) \right]^{3/2} t^{3/2}, \quad (1.17)$$

hence $r \sim t^{1/2}$. The experiments support this result. A. Steyer and D. Beysens [22] assume there is a flux of monomers entering through the contact line of an isolated droplet,

$$\frac{\partial n}{\partial t} = D \left(\frac{\partial^2 n}{\partial r^2} + \frac{1}{r} \frac{\partial n}{\partial r} \right). \quad (1.18)$$

The droplet is a 3-dimension object and it is surrounded by monomers on a 2-dimension surface, this assumption is also supported by T. M. Rogers, K. R. Elder and Rashmi C. Desai [26], where the concentration gradient is depicted as,

$$V \left(2\pi RD \frac{\partial n}{\partial r} \right) = R^2 \frac{dR}{dt} \quad \text{with: } \begin{cases} n(r, t) = n_0 \\ R(t=0) = 0 \\ n(R, t) = 0 \end{cases} \quad (1.19)$$

The Equation 1.18 is evaluated at the liquid-gas interface with the boundary conditions in Equation 1.19, where V contains information about the contact angle and the volume of one monomer. Far from the drop (at infinity), the flux of monomers ϕ is assumed constant. The spatial distribution of monomers around the drop can be obtained from the steady solution of Equation 1.18,

$$n = A + B \ln r, \quad (1.20)$$

where A and B are constants. After applying the conditions (Equation 1.19), the explicit form of monomers distribution becomes

$$n = \frac{\phi}{2\pi D} \ln(r/R) \quad (1.21)$$

and as a consequence of constant flux ϕ , the right side of the Equation 1.19, we have

$$R^2 \dot{R} = \phi V, \quad (1.22)$$

and right away the relation is obtained,

$$R \sim t^{1/3}. \quad (1.23)$$

Similarly, other authors support the idea of the monomers that run in a 2-dimension surface like P. L. Krapivsky [27]. This implies that the contact line plays the main role on the growth by condensation. Based on a quasi static approximation, he predicts that the radius increases as $(t/\ln(t))^{1/3}$. Some other aspects involved on heat and mass transfer can be reviewed on [28]. As I mentioned above, something common during the early stages of condensation is that the droplets are formed and grow very separated from each others $R_d > R_s$ (R_s is the radius of a droplet

and R_d the distance between neighbors). The droplets collect vapor by a diffusive process. This reduces the concentration of the molecules of vapor adsorbed in those sites that have not been occupied. Under this circumstances, the number of droplets is almost always constant.

$$\frac{dS}{dt} \sim \frac{1}{N} \simeq \text{const.} \quad (1.24)$$

where S is the average size of the droplet and N the number of droplets. In case of $d = 2$ and $D = 3$, $dR_s/dt \sim R^{-2}$ or $R_s(t) \sim t^{1/3}$.

1.5. The Coalescence Stage



Figure 1.5: After some dew have formed on my window, more humid air still is condensing.

Coalescence is a very complex phenomenon in the BF evolution [29]. We cannot only find condensation, but also, the interaction of the droplets and new generations of them in the empty spaces. As we will see, most of the models assume that the coalescence of two droplets of D -dimension, over a d -dimension, over a d -dimension hyper-surface, gives a new droplet with radius

$$r = (r^D + r^D)^{1/D}, \quad (1.25)$$

where the new center of the drop is the resultant of the other two drops' centers. The projection of the droplet over the surface has a radius $r \sim S^{1/D}$ with S the hyper-volume of the droplet. P. Meakin mentioned in [30] that the other rare event is the coalescence of more than two drops. Experimentally, these events are not rare. However, this assumption is taken to simplify algorithms and perform simulations. There is a very important dependence between the dimensions of the droplet and the surface, for example, if $D = d$, it is not possible to assume the process of coalescence will continue until to obtain an isolated droplet.

The coalescence events can be described in terms of the size s as following

$$\frac{ds}{dt} \sim s^{2/3}, \quad (1.26)$$

where s can be related with the drop's radius as

$$\frac{dr}{dt} \sim \text{const.} \quad (1.27)$$

1.5.1. The Scaling Laws

Fereydoone Family and Paul Meakin in [11] have established more general distribution functions to describe the stage of coalescence. The authors remark the distinction between the homogeneous or heterogeneous nucleation on the analysis of the mean growth of the droplets. This distinction is done because the referred work is based on simulation results. For those simulations, the authors define an area substrate as L^d to condense vapors, to condense a defined number of droplets in two configurations: in random and determined sites. Nevertheless, the following equations are valid for homogeneous nucleation and they are similar for a heterogeneous nucleation. Here, the homogeneous term means the droplets are distributed on random sites and the term heterogeneous is due to the selected sites for distribution of droplets. The difference between the both points of view will be displayed below. Meanwhile, the mean size of droplets is

$$S(t) = \frac{\sum_s s^2 N_s(t)}{\sum_s s N_s(t)}. \quad (1.28)$$

The size relation with the average radius is $R(t) \sim S(t)^{1/D}$ and this diverges as $S(t) \sim t^z$, and

$$R(t) \sim t^{z/D} \quad (1.29)$$

where z depends on the droplet dimension D and the surface dimension d . The total number of droplets $N(t)$ decreases with the exponent z'

$$N(t) = \sum_s N_s(t) \sim t^{-z} \quad (1.30)$$

It is possible to assume [31] that the number of droplets of size s at time t scales as

$$N_s(t) \sim s^{-\theta} f(s/S(t)), \quad (1.31)$$

where $f(x)$ is a bell-shaped function centered in $x = 1$ and with the form [30]

$$f(x) = x^{(\theta-\tau)} g(x) + h(x). \quad (1.32)$$

where $g(x)$ decreases rapidly at any power of x as $x \rightarrow 0$ and τ denotes the decay on smaller droplets and θ is the scaling of the whole distribution and depends on d and D . The density function proposed is

$$\rho = \sum_s s N_s(t) \sim \int s^{1-\theta} f(s/S(t)) \sim S^{2-\theta} \int x^{1-\theta} f(x) \sim t^{z(2-\theta)}, \quad (1.33)$$

Using the scaling form (Equation 1.31) in the definition of the density (Equation 1.33), we can obtain directly that $\theta = 1 + d/D$. The relation between θ and z is $(\theta + 1)/z = 2$ for $\theta \leq 2$ with $z > 0$. As R is the only relevant parameter on the system, the exponent z is defined as

$$z = \frac{D}{D - d}. \quad (1.34)$$

In case of heterogeneous nucleation, the equation which satisfying the defined initial sites are pretty similar

$$\frac{dr}{dt} \propto r^w \quad (1.35)$$

and the growth of a single drop is $r' = (r^\xi + \delta\xi)^{1/\xi}$ with $\xi = 1 - w$ and r' as the new value of the radius, and $w = 1 - D + d$. The density function, now is re-written as $\rho \sim R^{D-d} \sim t^{z(D-d)/D}$. An experimental discussion about this theory can be found in the R. D. Narhe and S. B. Ogale [32]. This investigation shows some discrepancies on the analysis of the droplets size s and $S(t)$ obtained by two different mechanism of condensation.

1.6. Another Model of BF Dynamics

An analytic model for droplets growth consists in observing the diameter of droplets D_A and to consider three features of the self-similar regime.

For Briscoe and Galvin [33–35], the three stages of BF evolution are: the nucleation and growth of the droplets just by condensation, and the coalescence with re-nucleation. The most important aspect of this theory is the establishment of a differential equation to connect the occupancy with the mean growth rate of the droplets. The drops diameter D_i of intrinsic growth can be generalized as

$$\phi_{Ii} = \frac{dD_i}{dt} = kD_i^{-\beta} \quad (1.36)$$

with β as the intrinsic growth law exponent and k is assumed constant. Then, the fraction occupation of the substrate in a certain area is

$$\epsilon^2 = \sum_{i=1}^N (\pi/4) D_i^2 = N (\pi/4) D_A^2, \quad (1.37)$$

and taking into account Equation 1.36

$$ND_A \phi_{IA} = k \sum_{i=1}^N D_i^{1-\beta} \quad (1.38)$$

Hence, the intrinsic growth is obtained from $d\epsilon^2/dt$ (from Equation 1.38),

$$\frac{d\epsilon^2}{dt} = \frac{\pi}{2} (ND_A) \phi_{NA} + (\pi/4) D_A^2 \frac{dN}{dt}. \quad (1.39)$$

The following assumptions are necessary to establish the above differential equation:

- a The geometry of the droplets is governed by the capillarity and the surface tension forces.

- b There is no hysteresis on the contact angle.
- c The coalescence events are instantaneous.
- d A coalescence event only involves two droplets.
- e The initial size of the droplets is the same, their sites are random and there is not overlap of droplets.

The Equation 1.39 and the relation $\frac{\pi}{2} (ND_A) \phi_{NA}$ describe the increment of the occupation ϵ^2 by the intrinsic growth, $N\phi_{NA}$ and D_A are constants related to the growth of intrinsic droplets in a respectively area. $(\pi/4) D_A^2 \frac{dN}{dt}$ denotes the growth due to the coalescence effect. The constant $(\pi/4) D_A^2$ is the expected change value on the area due to the coalescence events.

Chapter 2

Experimental Device and Tools for Image Analysis



Figure 2.1: Experimental set-up

This chapter provides a description of the experimental device, and of, the physical properties of the substances used to perform the experiments. The image analysis proceedings are described too. We show on detail, the calculation of geometric properties and their uncertainties using programs like ImageJ, Octave and Matlab.

2.1. Experimental Device

2.1.1. Description of the Condensation Chamber

The device can be described as a closed non hermetic chamber. It has three parts:

- (1) In the top cavity, there is a cover with a non reflecting window. There are four inlets too (or outlets, depending on the utilization). The inlets are placed every 90° . The vapor flows in a laminar flow regime at rates between 100 and 250 ml/min: the two faced inlets are used to flow gases at the internal part of the chamber to have a stagnation point in the center. At that place can be found established conditions and it is where the samples are set. The

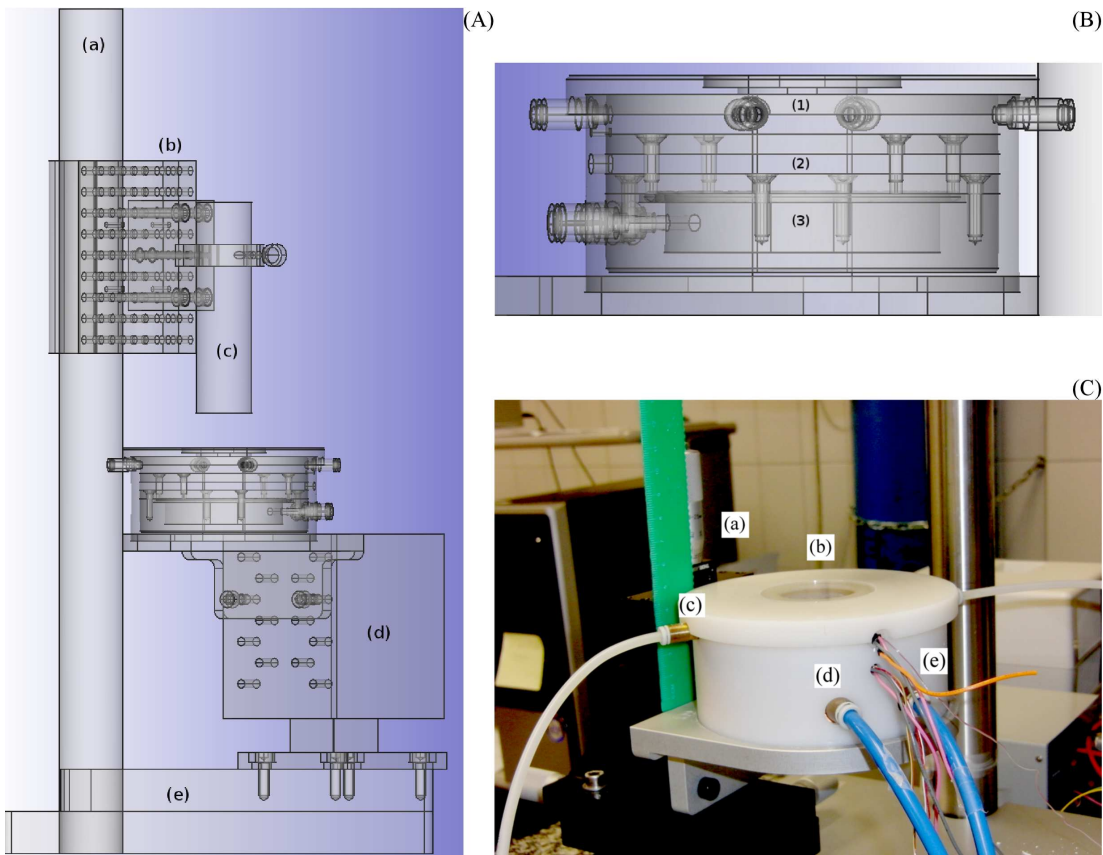


Figure 2.2: The Condensation Chamber. **(A)** Schematic view: (a) A post support of the microscope. (b) The holders and supports of the in-line microscope and digital camera. (c) The main tube to mount the microscope. (d) Translation stage X, Y, Z. (e) Weight to give stability. **(B)** The schematic view of the condensation chamber: (1) Workplace to set samples and to stream vapors. This places are divided by copper (good thermal conductor) plates. (2) Room for a Peltier element. (3) A tank of recirculating water made of copper to dissipate the heat extracted from the workplace. **(C)** The exterior of the chamber made of Delrin: (a) The cover. (b) Window of anti-reflective glass. (c) There are two inlets and tubes to stream vapor into the chamber, (d) And two inlets to do recirculation of cold water. (e) Thermocouples and power source connections.

air flux is supplied by two AALBORG flux controllers which operate on the range of 0 to 500 ± 0.2 ml/min. The inlets have an inner diameter of 2 mm and the associated Reynolds number is ≈ 318 . Moreover, in the Appendix 2 we show measurements of the velocity field inside the chamber in order to characterize the hydrodynamical effects. Those measurements were done by hot-wire velocimetry.

- (2) There is a Peltier element inside of a small compartment that is beneath the workplace and a copper tank. In the tank there is recirculating cold water (Figure 2.2B). With this device the operation temperature can variate in a range -13 to 60 ± 0.5 °C. The operation temperature depends on the polarity of the voltage operation. The Peltier element is a solid-state device

that uses the Peltier's effect to create a heat flux across the junction of two different types of materials. This electronic component can be utilized as a heater or cooler. It transfers heat from side to side against the temperature gradient when it is applied a electrical current. The Peltier element on operation has an efficiency of an ideal refrigerator of 5 or 10 %. In comparison with a reversible Carnot cycle it is very poor. Withal, its performance is enough to keep constant on established operation temperatures. The size of this electronic component are $3.4 \times 3.4 \times 0.4 \text{ cm}^3$ and the input power to produce temperature difference of 65°C at 35 Watts (Figure 2.3).

- (3) The chamber is mounted on a steel structure consisting of a post supporting an in-line microscope with a support table base with possibility of micro metric stage X , Y , Z (Figure 2.2A). Even though it is non a complex mechanism to operate, the system provides exceptional stability condition to develop experiments of condensation of gases. The Delrin material and the treated copper are resistant to the acid attacks and deformations (Figure 2.2C).

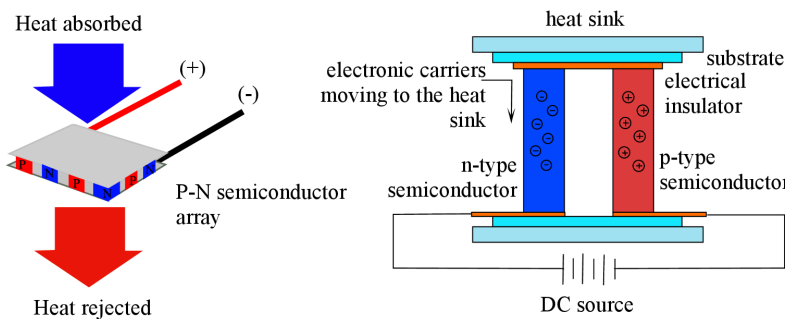


Figure 2.3: Peltier element extracts heat from a hot source to a sink by the action of electrical current (left). An individual $P - N$ solid-state array is shown (right).

2.2. Substrates, Substances, and Treatments

Many materials are hydrophobic like the polyurethane, and other plastics, silicon wafers, wax, solid benzene, some carbon fibers, the zircon glass, the silane coated glass, etc. The chemical etched metals or surfaces and the structured surfaces may increase the contact angle reducing the contact area of liquid droplets. The glass has been coated with ITO (Indium Tin Oxide). Also, it is a transparent conductive coating which can be used several times. Other substrates used are glass cover slips coated with 3M EGC-1700 (or 3M). Due to its thinness, this substrate is good to avoid thermal isolation effects. The 3M coated substrate and water develop a contact angle of 92° . The contact angle between the HMDSO $\text{C}_6\text{H}_{18}\text{OSi}_2$ and 3M coating is 65° . The coating procedure is simple; just dipping the glass into the 3M and then wait for few minutes to dry at room temperature. In some cases it is necessary to clean the substrates before using them. In the specialized literature are many procedures and recipes for the substrate cleaning [36, 37]. Sometimes, those procedures are required to give an aggressive chemical thermal bath in order to reorganize or alter the chemical bounds. For example when an ITO sample is cleaned with a

basic piranha bath, the hydrophobic property disappears awhile because the surface loses atoms of oxygen therefore the contact angle is reduced. Other methods of cleaning substrates consist only in washing the substrates with acetone, ultra-pure water or just ethanol in an ultrasonic bath, then rinsing with ultra-pure water. Those are not chemically aggressive and work well enough for our purposes.

The piranha based cleaning method (until the step 4, the other points are the common proceeding used to wash and clean samples) can be summarized in the next few steps:

1. Set the temperature of the thermal bath at 63°C.
2. Put the samples (ITO's) into a vessel. Add acetone (% 99) and cover the vessel. Wash in an ultrasonic bath for 15 minutes.
3. Remove the samples from the acetone and rinse the samples with ultra-pure water (or distillate water without organic residuals).
4. Set the samples in another clean vessel where there is ultra-pure water, peroxide and ammonia in concentration 5:1:1 (50/30/30 ml). Cover the vessel and put into the bath at 63°C for 40 minutes. This is called the basic piranha technique. This step is very aggressive and should be done with extra care.
5. Rinse the samples with ultra-pure water.
6. Dry the samples blowing nitrogen of % 99.99 (or dry filtered air) to avoid the production of nucleation sites with the impurities of the common air.
7. Put the samples on a clean and closed vessel and wait at least 14 hours to recover the hydrophobic property.

There are different methods to measure the contact angle of a droplet, but I focus only on the Sessile's method. This consists into obtain a high contrasted profile of that the drop interacts with a surface. To obtain it, the droplet is set in the middle of a back light source and in front of a recording camera. The result can be seen in Figure 2.4. The advancing and the receding angle can be observed too by adding and removing substance to the droplet with help of a syringe. More data can be found on Table 2.1.

As it has been said, to find the receding θ_R and the advancing θ_A angles, some liquid must be subtracted from and added to the droplet. The contact angle is reported as $\theta_s = 1/2(\theta_R + \theta_A)$ (Figure 2.4). It is very difficult to do those measurements if the droplet spreads over the surface. To measure the receding or the advancing angle, the droplet lets to evaporate or it makes to condense to obtain the receding and the advancing angles. The reason to measure those angles is that the droplet is in a state of non equilibrium with the environment. The explanation of this non equilibrium may lay in the follow citation: "Why do the drops evaporate? The reason why a droplet is not at equilibrium is because the its vapor pressure is higher than the pressure of the vapor in its surroundings" [38]. The mean of the advancing and receding angles give us an approximation of how the contact angle would change. Just in the case of non condensing and evaporating, the Laplace-Young relation is valid.

Substance	Common Glass	ITO	3M EGC-1700	$\theta_A \pm 0.2^\circ$	$\theta_R \pm 0.2^\circ$
Tap Water	★			54	34
Tap Water		★		54	34
Tap Water		★		54	34
NaCl solution	★			94	31
NaCl solution		★		92	61
NaCl solution			★	108	77
ultra-pure Water	★			108	82
ultra-pure Water		★		93	57
ultra-pure Water			★	108	82
$C_6H_{18}OSi_2$		★		13	—
$C_6H_{18}OSi_2$			★	29	24

Table 2.1: Advancing and receding contact angles for substances on different substrates.

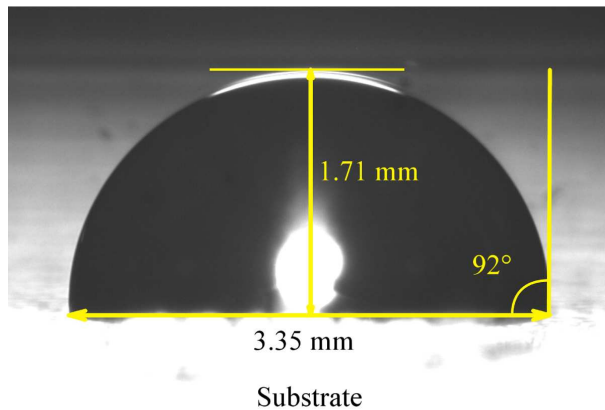


Figure 2.4: A droplet of ultra-pure water is set over a ITO substrate to determine its contact angle. The drop's profile is contrasted by the illumination according to Sessile method.

2.2.1. Physical Properties Values

The values of vapor pressure for WV in a range of temperature (-14 to 10 °C) can be consulted [39] (Appendix C, Figure C.1). The density of water is $\approx 0.99970 \text{ gm}\cdot\text{cm}^{-3}$ [40] and its surface tension of 74.23 mN/m (at room temperature $\approx 22^\circ\text{C}$). For WV, the thermal condensation is 580 mW/K·m. Other substance used on the experiments is the hexamethyldisiloxane ($C_6H_{18}OSi_2$ or HMDSO) with density 0.7638 g·cm $^{-3}$ [40]. For some experiments, it is necessary to measure the dew point for the saturated vapor at room temperature. To do this, the temperature of the chamber is reduced slowly until the vapor starts to condense, then the temperature of the chamber increases until the droplets were evaporated and again, the chamber's temperature is decreased until the condensation is observed. The dew point temperature of the supersaturated water vapor is 1.5 °C below at room temperature (24 °C). In case of HMDSO, the dew point temperature is 10 °C below of the room temperature. To perform experiments of condensation, the work temperature must be set under the minimum dew point of the two substances.

2.3. Tools for Image Analysis

Image analysis is an important tool for this work. Frequently, it is found in the literature that only simulation works offer many data to depict this kind of systems and about the experimental work, only few reports can depict very well the evolution profile of complex systems. Some calculus operations can be performed using routines for Matlab (mostly) from the data obtained.

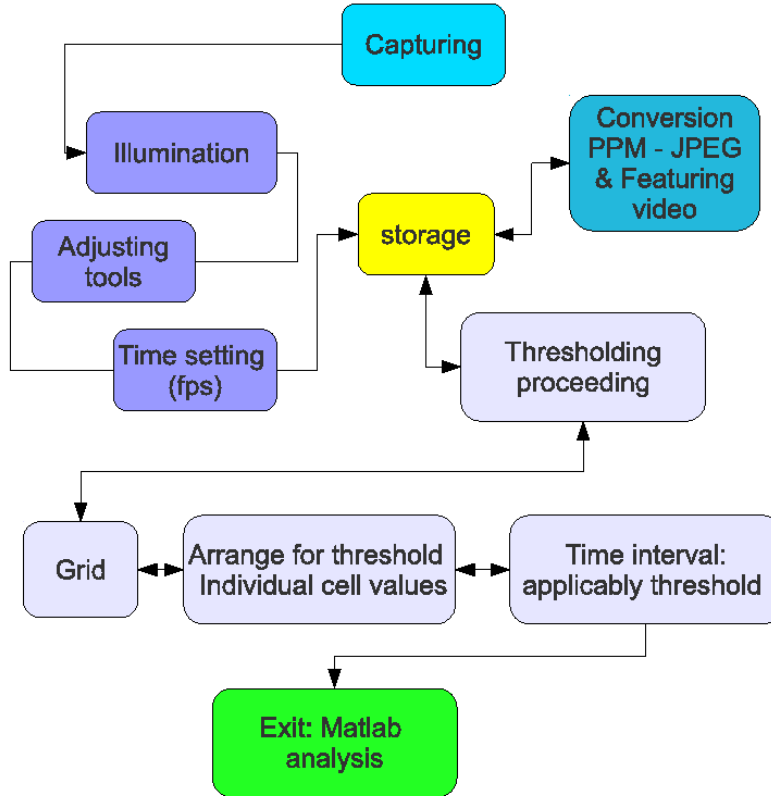


Figure 2.5: Flow diagram for images analysis. The previous image analysis routines appears at Section A.1 and are applied to all image stacks of all experiments. Before acquiring images, it is necessary to set an appropriate illumination, then handle the setting the acquisition program to capture the images. Those images are saved and then converted from the raw or ppm format to jpeg and selected color channel or grayscale. To extract the values of the radii of the pattern droplets, a treatment of thresholding is applied. This methodology is described below.

2.3.1. Acquisition of Images

A scheme of the analysis and calculus procedures is shown in Figure 2.5. Before performing the acquisition of images, the light source is adjusted, but also the settings of the camera (mentioned above) are adjusted. The parameters of capturing video of images are selected. The images are acquired with a in-line microscope. We apply axial illumination by an optical fiber bundle. The snapshots have been acquired with a digital color camera PixeLink model PL-B776F with

variable resolution from 800×600 to 2048×1536 pixels. The camera is mounted at the end of the optics system of the microscope. The recording of images is done by a free Linux software "Coriander". The previous analysis starts with routines of "FFmpeg" in order to separate colors, modify formats (ppm to jpg, or others), or transform the stack of images from color to grayscale. This Linux command is used to make videos of the experiments. The acquisition rate can variate from 0.1 to 1 Hz depending on each experiment. depending on each experiment. In some cases is desirable to use a high speed camera with a rate of 1000 fps for short times to observe certain phenomena. In Appendix A a compendium of programs related with the image analysis can be found.

2.3.2. The Threshold Problem

In observations, the light is reflected by the surface and by the droplets of the BF. When some droplets reflect the light, they lead to caustics. Depending on the kind of experiment, these reflections could be in benefit of the analysis or not. For example, the salty drop in the middle of the observable area (see next chapter) reflects the light to the rest of the BF around. For this case, a silicon wafer was set below the sample to increase contrast. At the limit of this observable area the illumination is poor, and when we apply a thresholding process to images¹ what we have noticed is that the threshold values cannot be used as invariant values for all images. The values of the thresholds may change with time and size of the drops too. A previous work of calibration must be done before using Matlab's routines [41, 42]. We partition one image into cells, then select the befitting thresholds values and test them for other images.

For example, in Figure 2.6, the thresholding applied considering the whole area of the picture cannot preserve the original size of the objects. We may think in another procedure of thresholding to treat the images:

- (1) We proceed to partition the images into cells to assign individual threshold values for individual as following:
 - We partition the image's stack into cells (Figure 2.7). For example, for one image of 2048×1536 pixels we can partition into cells of 256×256 pixels and we obtain eight columns per six rows.
 - The cells are tagged. To analyze the image stack, it is necessary to check how many changes of threshold has a cell. Programs like ImageJ or Fiji work very well on testing the threshold values.
 - Once the thresholding history is obtained, it is necessary to assign those values per cell and per image on time (Appendix A.1).
- (2) If we would have need to analyze a small area of an image we can avoid the last point. First, it is needed to know the boundary of the object to analyze. Then, this part of the image is cut and two values of threshold are applied ("the object is skeletonized") within the minimum and the maximum threshold values. The difference between the large and small bodies is, the large objects do not present great variations on their threshold values. The small bodies are very sensitive to those changes. Once a large body is thresholded (Figure 2.8), we project

¹The interpretation of 0s and 1s on the statistical calculations.

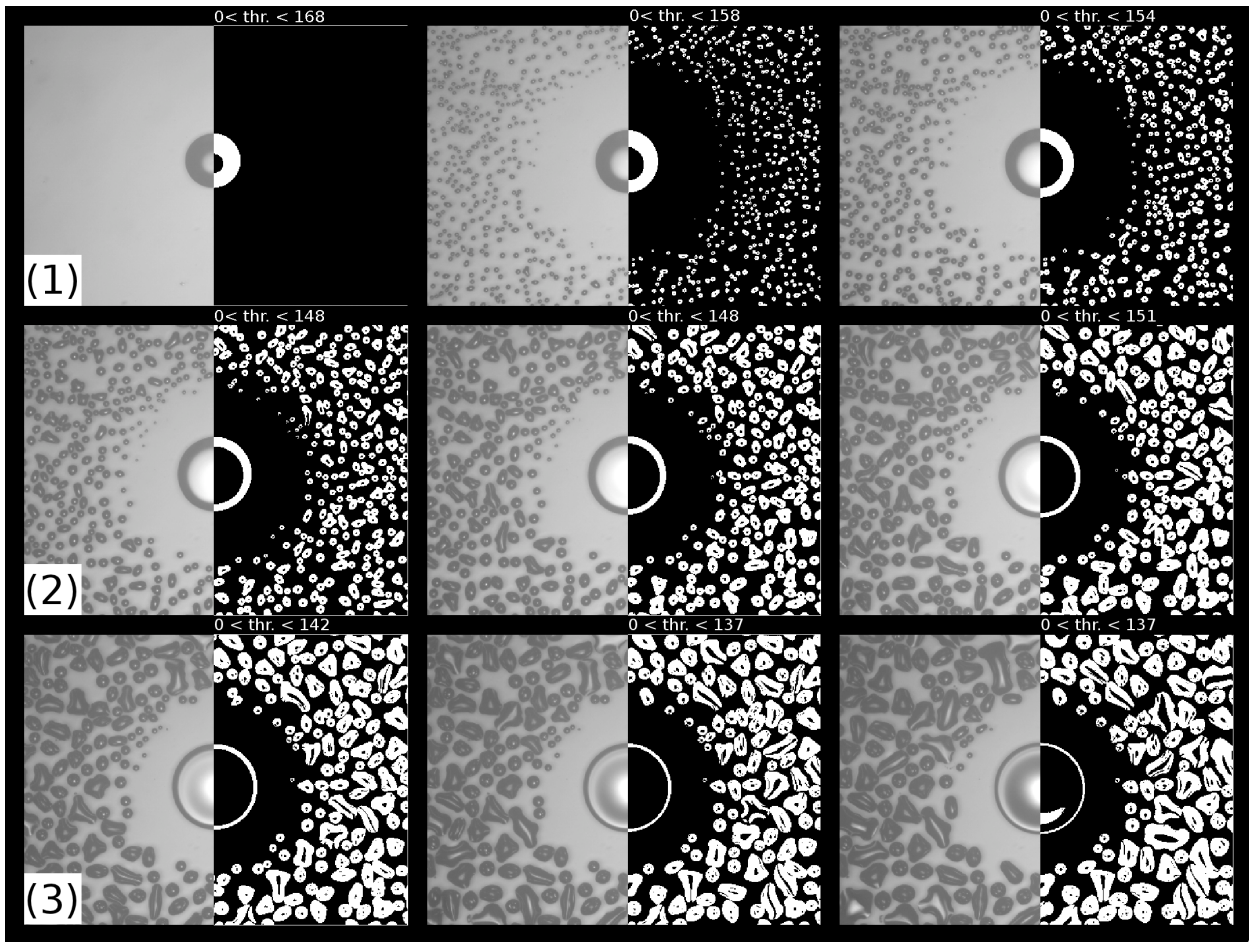


Figure 2.6: The drop in the center corresponds to a salty drop of a saturated solution of NaCl on water at 10 °C. This object reflects the light backward to the camera and the fiber optic leading caustics all around. The center of the image is brighter than the edges of the snapshot. Each snapshot represents 25 s in time of experiment observation. The row (1) with the snapshot taken from 1 to 50 s and their labels of the different values of threshold give a good idea of the variability of the threshold as a function of luminosity. The variations of the threshold are not linear (2) and (3) different thresholding is compared.

over the X-axis and Y-axis (Figure 2.9). The radius and the geometrical center of the body are calculated by a Fortran routine and the information with physical meaning is written in a ASCII file.

- (3) Sometimes is convenient to come back to hand made analysis to obtain information from very complex images. We refer as complex images to those where there are two condensed substances, or for the icing process where no spheric geometry is found. For those cases, it is advisable to use programs like Fiji or ImageJ which allow to record on a file positions of pixels by just clicking a button. Once all the information is acquired, it is very useful to complete the interpretation by the utilization of routines for Matlab, Octave or Fortran.

- (4) In depth, for amorphous objects, instead of marking the edges of the objects in the picture, it works very well to draw masks over them. The thresholding process is accurate during the calculation of the areas and the counting the number of objects. The limitation is, the work area is reduced and that the time spent drawing masks takes long time. This procedure is applicable when it detected a special interesting area.

There are no straightforward measurements or/and computation of geometric amounts of the droplets in the image stacks. Apparently, the method to choose depends on what part of the system is sought after to apply one or other procedure of information extraction. The manual methods rather than automatic processes are preferable when the shape of objects in the pattern are not clearly defined. Otherwise, the automatic processes are good options when the analysis of the objects in the pattern have geometric symmetries. For this last option, it must be done a short previous procedure of preparation. In principle, it is necessary to choose the region where the object is, and to know what maximum size it reaches. That means, to observe the maximum time its size and to choose the limits to cut the image and reduce the image complexity. Before the thresholding, it is possible to apply filters of fast Fourier transformations (FFT) too. Concerning the measurements of the droplets of the BF, it is important to remark that not all the experiments are candidates to apply an automatic analysis. Just few experiments can be treated with the cell thresholding assignment. The option for those systems is the usage of a graphic tablet with a digital stylus to mark the coordinates of the ends of the droplets, or to draw masks. After that, it is recommended to run programs over the results to find the radii and other geometric values. A very good example of the automatic image analysis is the BF in presence of a salty drop.

2.4. Errors

The different methodologies explained above have advantages and drawbacks. The procedures for complex² measurements can increase the error propagation. As it is mentioned before, it is not desirable that the data have too much dispersion. Also it is suitable to have a balance among the uncertain and the amount of data. In this section, I show a very basic protocol to compute uncertainties for measurements obtained by programming in Matlab and ImageJ. With GNU programs like Gimp, the maximum aspect of resolution for an image of 1536×2048 pixels. Taking into account that this is the maximum the camera pixeLink's resolution. At this respect, if we use a microscope objective of 2X, the maximum size observable is $\approx 10 \mu\text{m}$, which corresponds to ≈ 4.65 pixels for clearest observation³. The possibility that is left, is to consider an initial error due to the noise and other non controllable factors during the experiments. We consider the uncertainty is in a range of admissibility from 20 to 10 % of the mean area of the objects. The error associated to the Matlab's analysis comes from the process of binary thresholding. The selection of thresholds values to represent a binary image are compared always with the size of objects measured directly from original images. This measurement has assigned a $\approx 10\%$ as the error of the appreciation of the bodies. Figure 2.8 shows the values of droplet radius (Figure 2.8) obtained at different values of the threshold. The measured value of the central drop's radius is 213 ± 21.3 pixels or $459 \pm 45.9 \mu\text{m}$. The value reported (the program is in Section 2) is 213.25 ± 38 pixels,

²With many intermediate steps.

³When the light contrasts, illumination, in the range of camera's work temperature ,etc. are optimal.

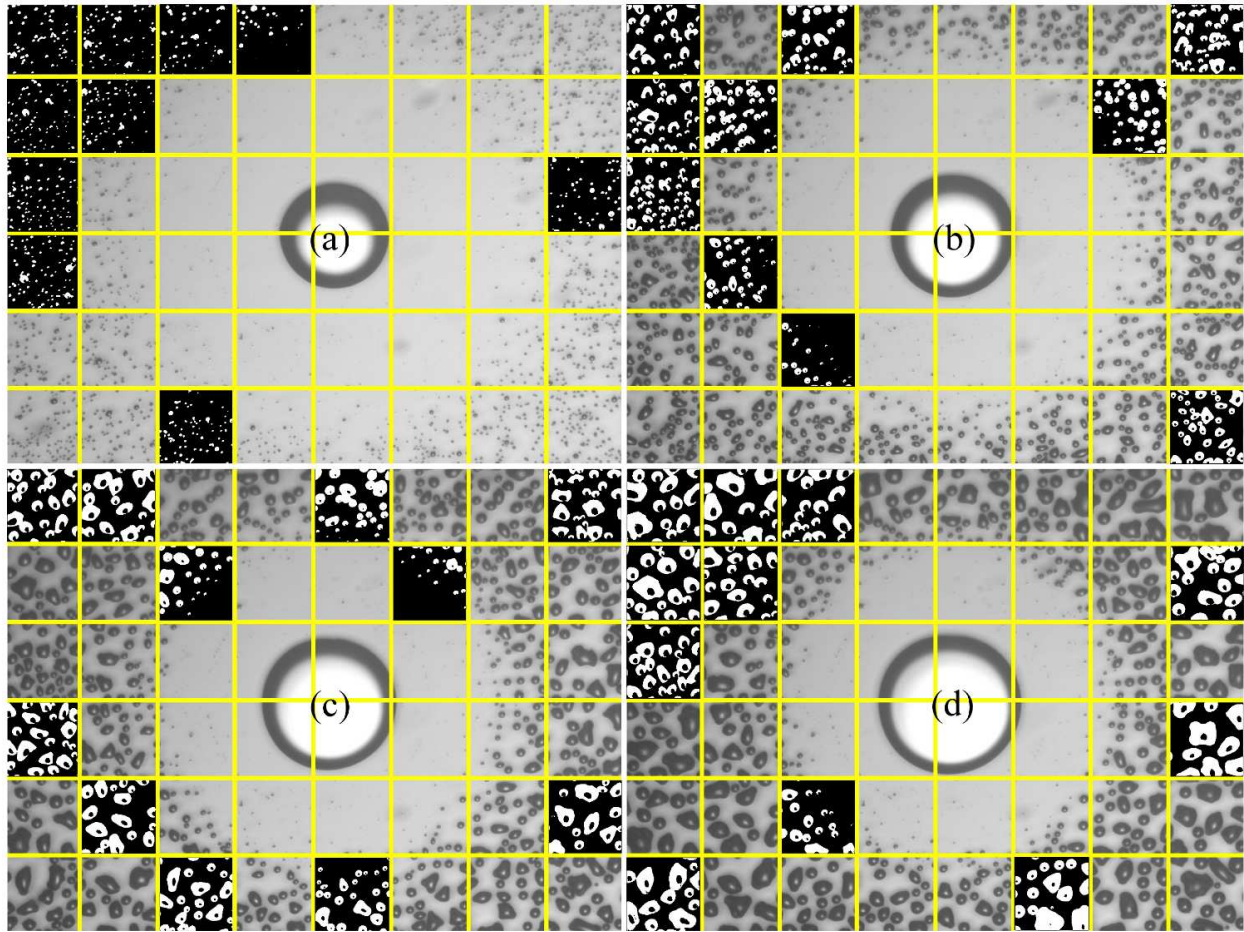


Figure 2.7: The snapshots have been partitioned and a thresholding has been applied according to the methodological analysis described above. The change of the threshold value depends on the position and the size of the droplets. The threshold is defined between upper and lower limits to not blur the objects and preserve the number of droplets per cell. For this example, we refer to the salty drop experiment. The corresponding series time of the experiment is: (a) to the time $t = 30$ s, (b) to $t = 250$ s, (c) to $t = 500$ s and (d) to $t = 900$ s.

the interval where the peak has also an uncertainty, then is necessary to add the 10 % to the uncertainty, thus 213.25 ± 42 or $459 \pm 90 \mu\text{m}$. In case of this example, the threshold value is 130 (Figure 2.9).

The uncertain associated with the Matlab's analysis come from the process of binary thresholding. The selection of thresholds values to represent a binary image are compared always with the size of objects measured directly from original images. This measurement has assigned a ≈ 10 % as the uncertainty of the appreciation of the bodies. Figure 2.10 shows the values of droplet radius (Figure 2.8) obtained at different values of the threshold. The measured value of the central drop's radius is 213 ± 21.3 pixels or $459 \pm 45.9 \mu\text{m}$. The value reported (the program is in Section 2) is 213.25 ± 38 pixels, the interval where the peak has also an uncertainty, then is necessary to add the 10% to the uncertainty, thus 213.25 ± 42 or $459 \pm 90 \mu\text{m}$. In case of this

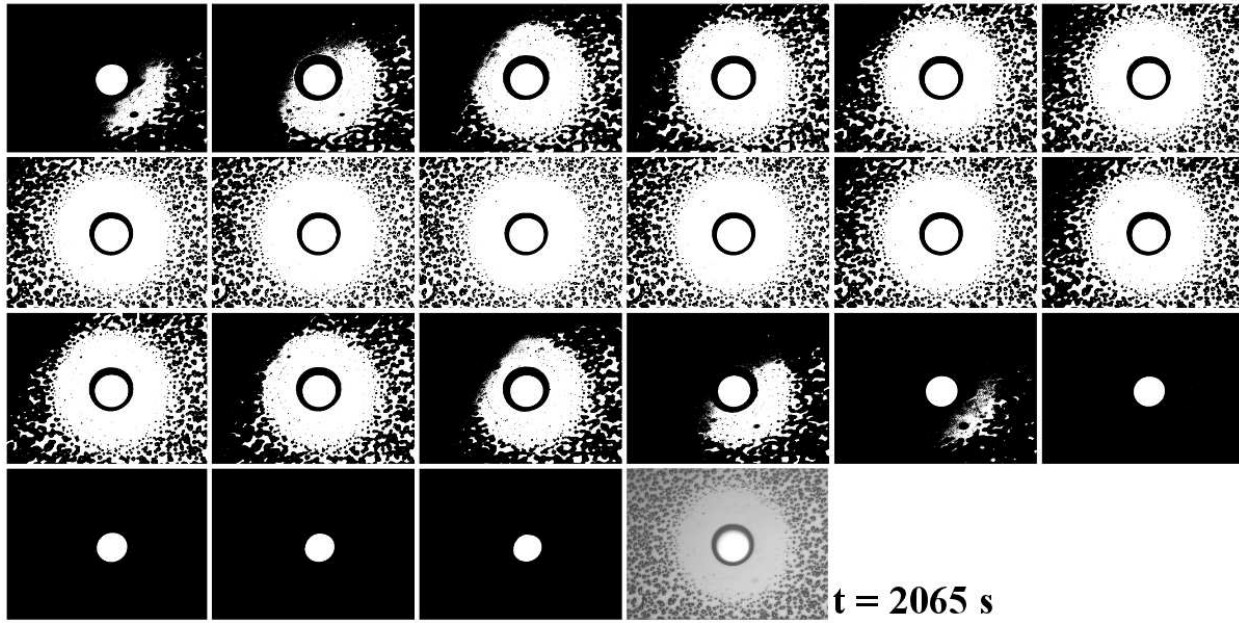


Figure 2.8: Different thresholding (from 40 and with an increment of 10 until 240, from left to right) has been applied to the same image in order to describe how to find the proper value threshold. The central drop is chosen as an example for uncertainty calculation.

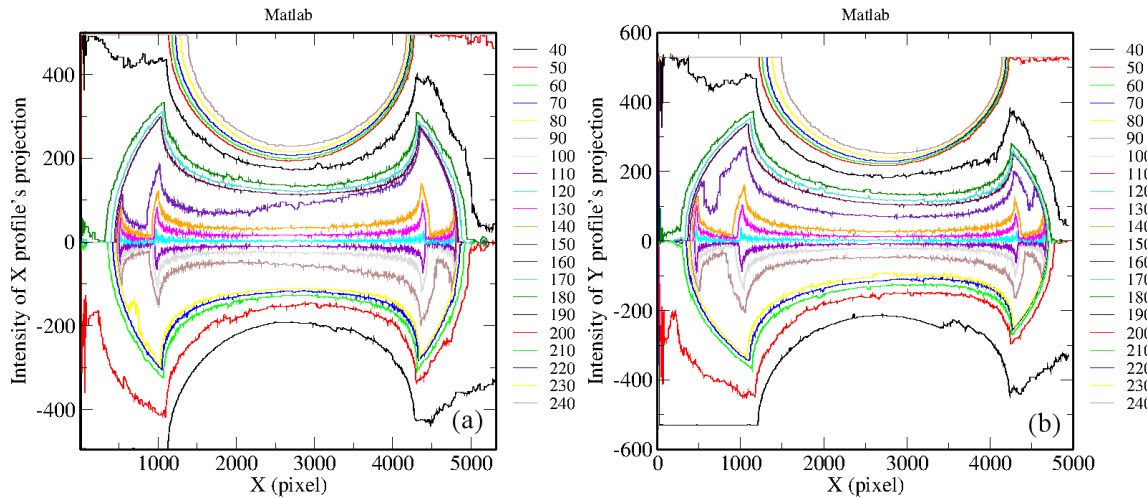


Figure 2.9: (a) The projection's droplet in horizontal orientation. (b) The projection on vertical orientation. The limit of the central drop (for example) is chosen by applying different thresholding. Then they are compared with the measure obtained from the original image. The entire images with the threshold application are shown in Figure 2.8.

example, the threshold value is 130 (Figure 2.9).

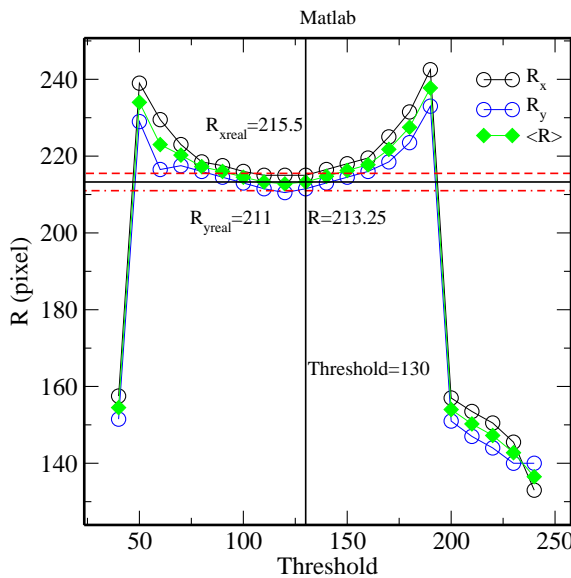


Figure 2.10: The proper threshold value is 130 which corresponds well with the value of the radius measured on the original image. In pixels, the value of the radius found is 213.25 pixels (459 μm) which is obtained from $(R_x + R_y)/2$.

2.4.1. The Error of Calculations with Matlab.

The uncertainty of an individual measurement can be obtained with the following criteria: in case of large drops, it is visible that the illumination produces an effect of lens and the center of the droplet is reflecting light⁴, while the borders are not (Figure 2.8). To determine the real size, we look for on the last fringe (where the border ends). This geometrical place is detected as a peak. Then, the width of that peak is the associated error of the drop's border (Figures 2.11).

2.4.2. The Error of Calculations with ImageJ.

The ImageJ and Fiji softwares were also used to analyze certain experiments. For example, measurements of the crystals' size, the distances between droplets and crystals, and the small increments of growing ice (Chapter 4). Those programs are a very useful tool where the geometry of the system is extremely complex to deal with it, by means of programs dedicated to follow spheric shapes (Chapter 5). ImageJ and Fiji have options to automatize the thresholding, isolate objects, and to apply FFT in 2-d (Fast Fourier Transform). Commonly, the thresholding, contrast, and brightness are enough for the definition of images. The drawback of those softwares is the memory required and the difficulties that any non programmer of Java could find trying to write scripts to do specific statistic analysis and making plots to report. Also, we need a secondary software to do the data analysis. The error related to the utilization of ImageJ is shown in Figure 2.12. A few steps, a value of R is ready to report an uncertainty like 213.25 ± 21 or $459 \pm 45 \mu\text{m}$.

⁴Leading caustics.

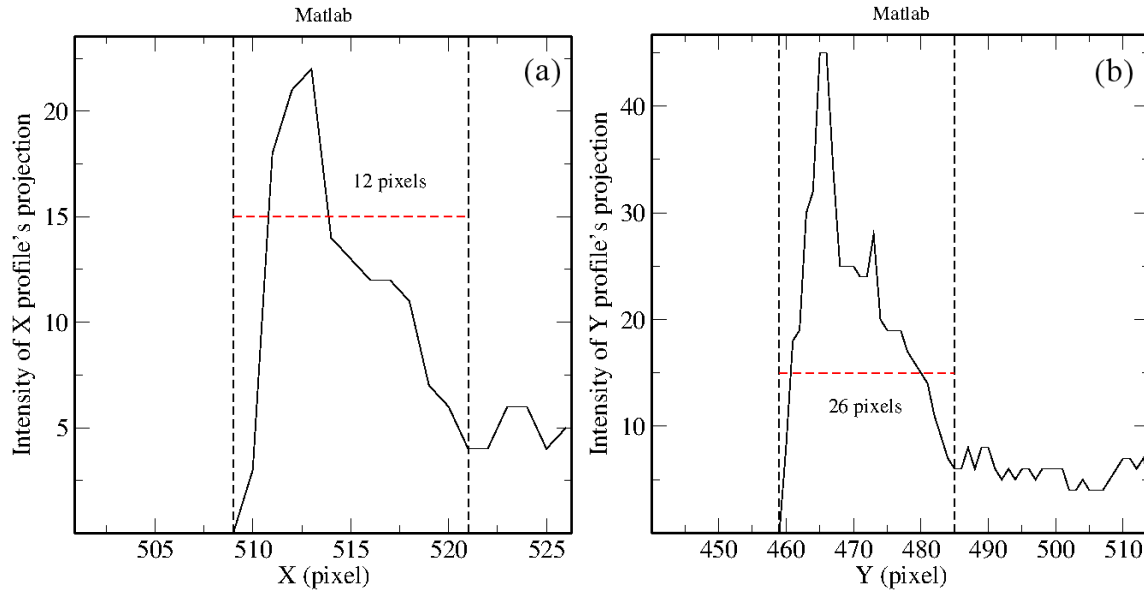


Figure 2.11: (a) and (b) Projections of on axis X and Y of the drop's profile. The drop's profile is obtained for horizontal and vertical orientations and then, both measurements are averaged to report the mean radius R .

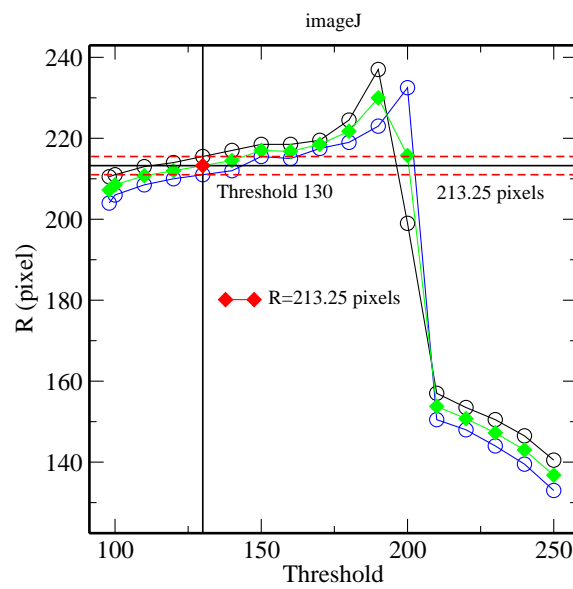


Figure 2.12: Similar than Figure 2.10, the radius in horizontal and vertical direction were averaged to report the radius R .

Chapter 3

Breath Figures in Presence of a Humidity Sink

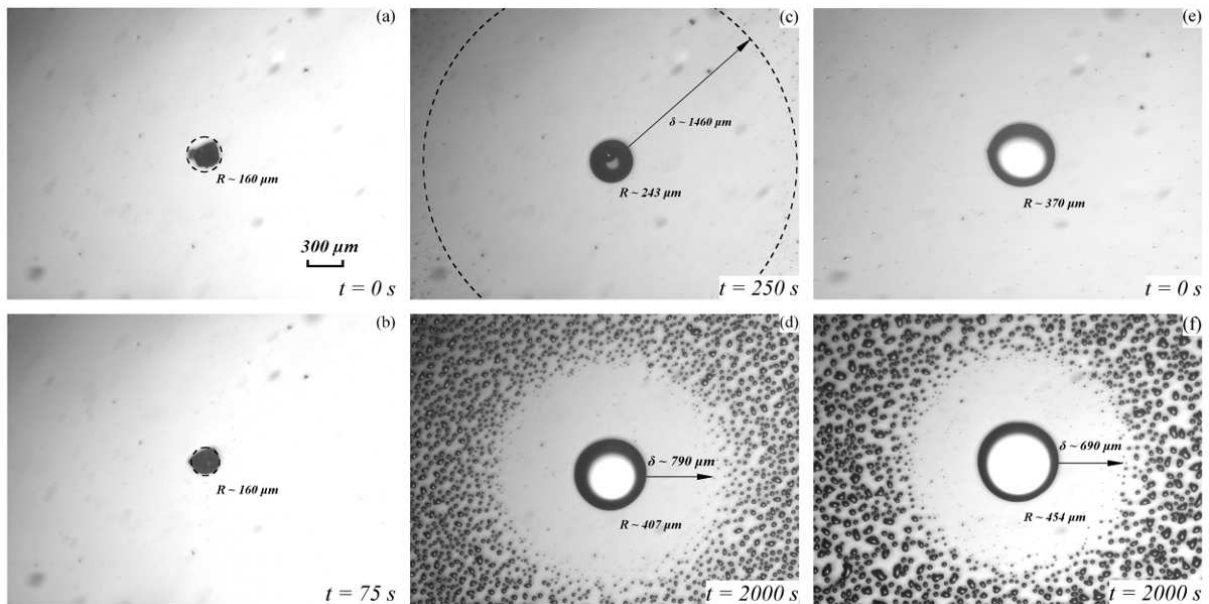


Figure 3.1: (a) A crystal of NaCl (radius $\approx 160 \mu\text{m}$) is set over a cold ITO substrate ($T = 10^\circ$). (b) Immediately, a flux of water vapor (165 ml/min) produces dissolution. Far from the observable region, some droplets appear. (c) The crystal becomes a salt aqueous saturated solution. (d) The Breath Figure covers almost all the substrate. In another experiment, (e) a salty drop of a saturated solution is set over a substrate under similar experimental conditions to (c). (f) The final stage is similar to (d).

3.1. Introduction

For the life in general, water is very important. In many processes water plays the main role in life of human beings, animals and plants. Water on Earth is interconnected with the atmosphere, oceans, aquifers by hydrological cycles. From global point of view, the water resources and the recollection are becoming a matter of strategy to supply of national security in developed countries. So the studies of water properties should have priority.

At physical chemistry level, when water plays the role of solvent or catalyst, it may modify the thermal and chemical properties of the substances. The aim of this chapter is to understand the BF formation process in presence of a humidity sink. The physical chemistry problem is studied from the point of view of the dynamics where the volume change on time as water is added to the salt crystal by WV condensation. Once the salt solution has reached a certain water concentration, the BF is visible (on the observable area) and the average size of the water droplets can be measured at certain distance of the salty drop. This information can be used as an indicator of the values of the partial pressures distributed around to the humidity sink, as well, the amount of water condensed. The research on the interaction of WV with a salty drop started by J. S. Owens in 1922 [43]. Some decades, R. Williams and J. Blanc [44] have attempted to explain what it is the influence on the surrounding of a crystal collecting WV. The subject of the study it is a NaCl crystal in presence of condensing WV. They argued that the temperature is the main variable and it could be related with the difference of pressures of supersaturated WV. However, they have not offered a description of the entire process of condensation evolution. Furthermore, C. Schäfle, et al. [45] have said the BF formation is due just to a heterogeneous nucleation without deep in the analysis and just by the examination the depletion zone of an arrangement of sinks.

The initial idea of this research work is due to Dr. Ramchandra Narhe in 2007. He suggested an experiment to create a concentration gradient by setting a humidity sink on a BF like a salt crystal. The very well known growth laws of BF are used to understand the evolution of the system in this configuration. The sink used to perform the experiments (Figure 3.1) is a NaCl+H₂O salt solution in a hemispheric droplet shape. The sink capacity to adsorb vapor will decrease as a function of time, while the depleted zone between the BF will shrink. All the challenges have come when we have tried to extract information from the visualizations. At the beginning of this research, we have done the experiments to follow in time the BF formation and simultaneously the salty drop evolution. That meant, the objective of the microscope was moved in all directions trying to scan parts of the salty drop, parts of the depletion zone, and the drop's carpet. The first difficulty of this methodology was to match the images at different positions and at different times. So, we have decided to set over the substrate a very small salty drop to observe the three regions of the system. At that time, this resulted a very good idea but in practice was not so easy, because not very small drops could be obtained using syringes and micropipets. The constant problem has still been the size of the salty drop. To have control on the micro scale was not so easy as we have thought. We have found that the way to set a small salty drop was to put a drop on the substrate, then evaporate it and separate the small crystals with a needle. Once a small crystal has been separated, a drop was obtained again by the humidity and because the temperature of the substrate was decreased. After this, it was necessary to pay attention at the

water vapor source. As a reservoir of vapor we have used a wet cloth. It resulted a not very stable source as humidity decreased upon time. The solution to this was to install a pump to flow N_2 (or dry filtered air) through a flask bubbling ultra-pure water. The other improvement was to install a temperature controller to avoid high variations of the temperature. Once all those improvements have been applied, we noticed that we have not had any reference of what should be the amount of salt on the solution. We prepared a salt saturated solution at $T = 10^\circ\text{C}$. Now, finally the ideas of how to perform this experiment were completed, it was left improve the image data processing. A lot of time we have spent in writing code, testing it and comparing the results. The first difference between the old perspective and the new is, that with the new procedures we could reduce the data dispersion and increase the time resolution. Now, we could do conjecture about the phenomenon like the physical reference mentioned above. The exactly moment when the crystal salt is totally dissolved is the time and radius reference. At this time, the salty drop reaches the condition of saturated solution at the operation temperature. We have found that the growth law of the salty drop depends on this value. The depletion zone evolution can be explained using those references. We will see that the radius and time are useful to obtain the partial pressures at the perimeter of the salty drop, on the depletion zone and where it ends.

How the vapor concentration is distributed around the salty drop is also a question to solve in this work. The physical process of "Breath Figure in presence of a humidity sink" has begun to be observed with more detail. We have developed a methodology to do measurements and to gather accurate information. At the same time, other questions have arisen from the calculations like for example which could be a suitable analysis to understand the WV concentration and to describe the system. This question has driven the analysis of $\langle r \rangle$ as a function of time t and an area defined on the rings zone $R + \delta < d < \delta + \Delta\delta$ where $\Delta\delta$ is the maximum value of the diameter of a droplet in the BF and d is the width of the ring. Other question arised like: What are the best spatial contour to compute $\langle r \rangle_t$ to give the best and realistic depiction of the BF? Other questions have emerged too. What is the relation between R and δ ? and, what is the difference of pressures between the salty drop perimeter and the beginning of the BF? I will deal with these questions in the next sections.

3.2. Experimental Procedure

The description of these series of experiments is based on the Chapter 2. The ITO was chosen for the experiments and two possibilities to set the salty over the substrate were done: a submillimeter salty drop is set over the substrate to do the experiment. Previously, it was made a salt solution (for 10°C , the proportion of NaCl is 35.72 g on 100 g of water [40]). The other procedure consists into set a salty drop, evaporate it by heating the substrate, spread the small crystals, and focus the microscope over the smallest crystal, set the temperature at 10°C and flow the water vapor. Both cases are very similar and the results are comparable (Figure 3.1). The first methodology is easy to follow but the salty drop set over the substrate cannot be controlled properly and during the observations the time reference and initial radius are missed. With the second methodology, the references can be set. There is another benefit in the latter method. It is easy to recognize the time where the crystal salt is dissolved and in consequence, the exact time where the salty drop reaches the saturated condition.

3.2.1. Image Analysis

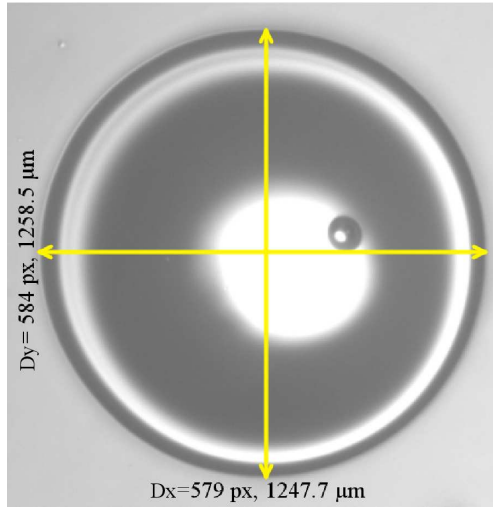


Figure 3.2: Previous to data extraction, the salty drop's maximum size is used as a limit to crop all the images.

In Section 2.3 the main image analysis procedures have been mentioned. Also, it has been discussed how to treat the stack of images depending on the conditions. To compute the salty drop radius, we have taken the largest diameter to crop the area (Figure 3.2) for all snapshots. After, each image is zoomed (10 times) on X and Y direction to improve the accuracy on the measurements. Then, by the thresholding process it is obtained the pixel intensity and the coordinate profile of the salty drop in two Cartesian projections X and Y (see Section 2.4). By a simple Fortran's program, we measure the starting and the ending points of the salty drop. Once, the length between the start and the end coordinates are found for all the observations, the diameter for X and Y are averaged $R = (D_X + D_Y)/40$ (see Figure 3.3). Then the calculation of R is checked against some original snapshots. The next step is to determine the length of the depletion zone. This zone is the empty space between the perimeter of the salty drop and the very beginning of the BF's droplets. The original space of the snapshots must be transformed again. Now with the computed center of the salty drop C_{xy} the entire snapshot have been centered at C_{xy} . A black frame around the original snapshot has filled with values of -1, which provide an apparent square observable area. We choose a threshold with a condition: $a < pixel$ and/or $b > pixel$ where a and b are limit values to recover the edges of the salty drop in ones and zeros. The corresponding array for the image's frame is filled with the -1s (Figure 3.4). This value will help the programs to discriminate just the frame during the calculations, coinciding the center of the salty drop and the coordinate's origin which is very convenient to transform Cartesian to polar coordinates (Figure 3.5). The corresponding pixel coordinate values for the perimeter of the salty drop until the start points of the BF had been averaged to obtain δ which it is the width of the depletion zone. This procedure lets to obtain description on time of this part of the system to get some relevant results.

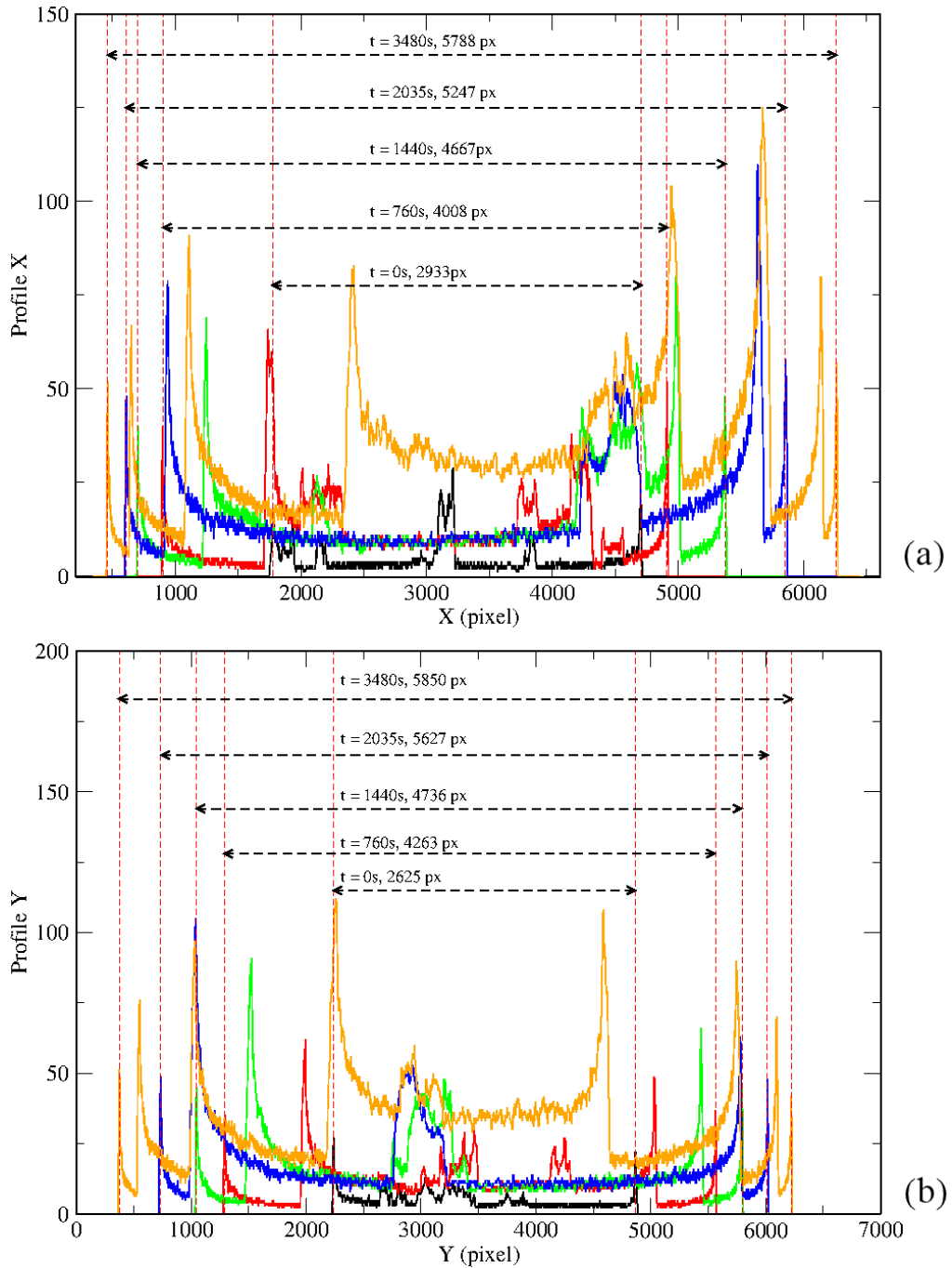


Figure 3.3: From Figure 3.2, all images have been enlarged 10 times. The salty drop's radius and center C_{xy} are measured from the profile projection of horizontal (a) X and (b) vertical Y orientation.

3.2.2. Integration Procedure for $\langle r \rangle$

All the necessary parameters have been calculated at this point. To analyze the BF pattern, the space of the image 2048×1536 has been partitioned in 48 (8×6) cells with assigned threshold

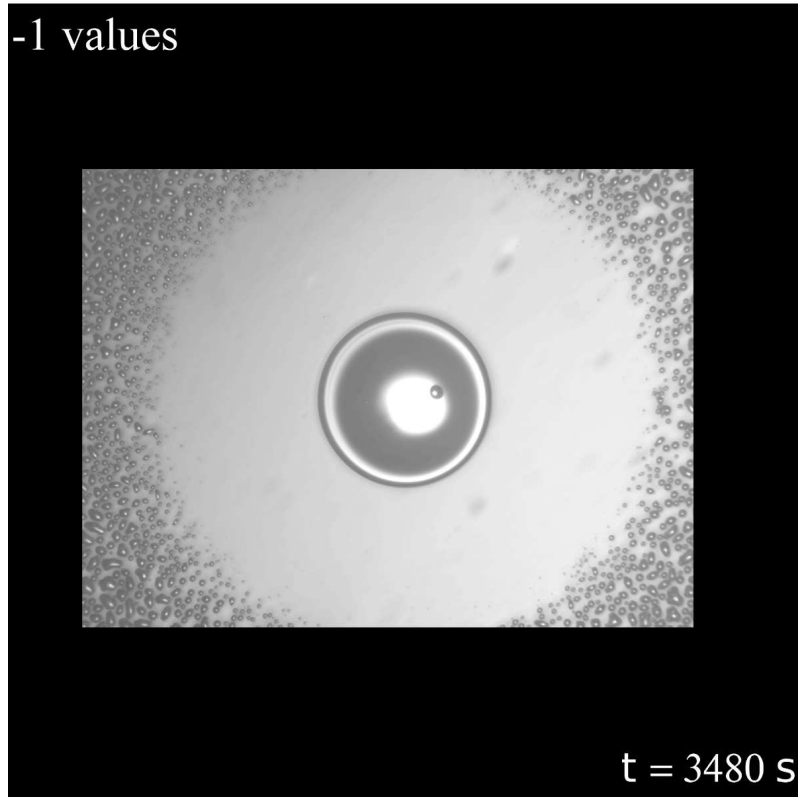


Figure 3.4: The geometric center values of the salty drop are taken to set re-center the whole size of the pictures over a black square frame.

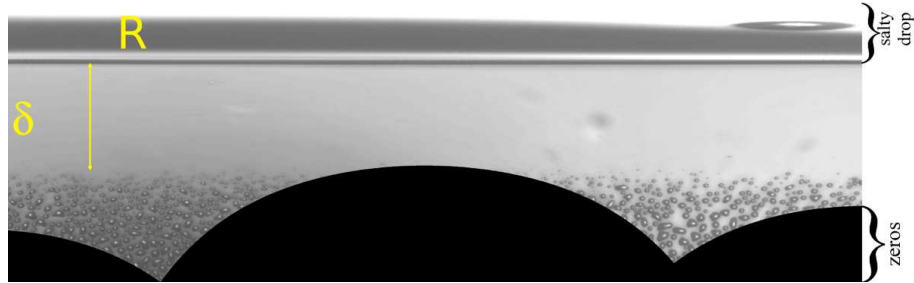


Figure 3.5: Once the whole image stack has re-centered, and the spatial transformation from Cartesian to polar coordinates proceeds. The salty drop became a rectangle (above), the depletion zone is the rectangle in the middle, the droplets of the BF are below the depletion zone. The black arcs correspond to the corners. A running average of the height of middle rectangles provides the δ 's values.

number in ${}_t T_{ij}$ where the arranged T contains the threshold values, t is the time where those values are valid, i is the column index and j the row index for the number of the cells (see Figure 2.6). The variables of the system are the radius of the sink R and the depletion zone δ which define inner radius of a ring of length $R + \delta$ from the center of the salty drop as a geometric

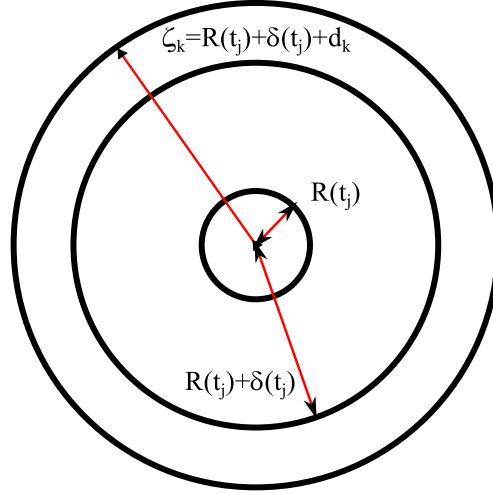


Figure 3.6: The average radius $\langle r \rangle$ is computed as following: (1) extraction of drops centroids and radii for all observational time. (2) Definition of the computational domain $[\zeta_k, R + \delta]$ at time step t_j , with $j = 0, \dots, n$ and d_k , with $k = 0, \dots, m$, where d_0 = drop's maximum diameter on BF's second stage. (3) Obtaining $\langle r \rangle(t_i)_{\zeta_k} = \frac{1}{m} \sum r$ on the defined area at observational time t_i .

reference of measurements (Figure 3.6). The exterior radius is defined as

$$\zeta_k = \delta(t_j) + R(t_j) + d_k \quad (3.1)$$

where d_k is the width of the ring and also it can variate until 2 times δ . We must notice while the R is increasing, the area defined by δ is shrinking. We are going to define the time t_k to refer only as the time of those lengths. Concerning the breath figure evolution inside the ring, the time will be tagged as t_i , hence the average of the radius $\langle r \rangle$ is a function of t_i , ζ_k and d_k . In terms of the image analysis, once the values of R and δ are obtained, (Figure 3.7). The results of these operations, a discussion of the possible interpretations of ζ , as well, a profound discussion of the physical meaning will be discussed in Section 3.4.

3.3. The Humidity Sink and the Depletion Zone

Several experiments were tried to test the importance of the variations of the flux and the initial radius of the salty drop. The volume of the droplet at the exact instant when the crystal salt is totally dissolved in water is $V_0 \approx 6.1 \times 10^{-8} \text{ cm}^3$ (Figure 3.1c). The mass of water on the salt saturated solution is 5.23×10^{-8} g. Due to this insignificant amount, henceforward, I am just going to deal with the radius because it is the main parameter in the description of BF dynamic. The volume of the salty drop can be treated as hemispherical because during the experiments lateral observations have done and the contact angle have not significantly changed (Figure 3.8). A more convenience description is necessary to do. There is a flux of water molecules (or monomers) what will be adsorbed by the salty drop. Assuming the number of those molecules is very large because of the flow into the chamber is constant during all the experiment. And by applying the

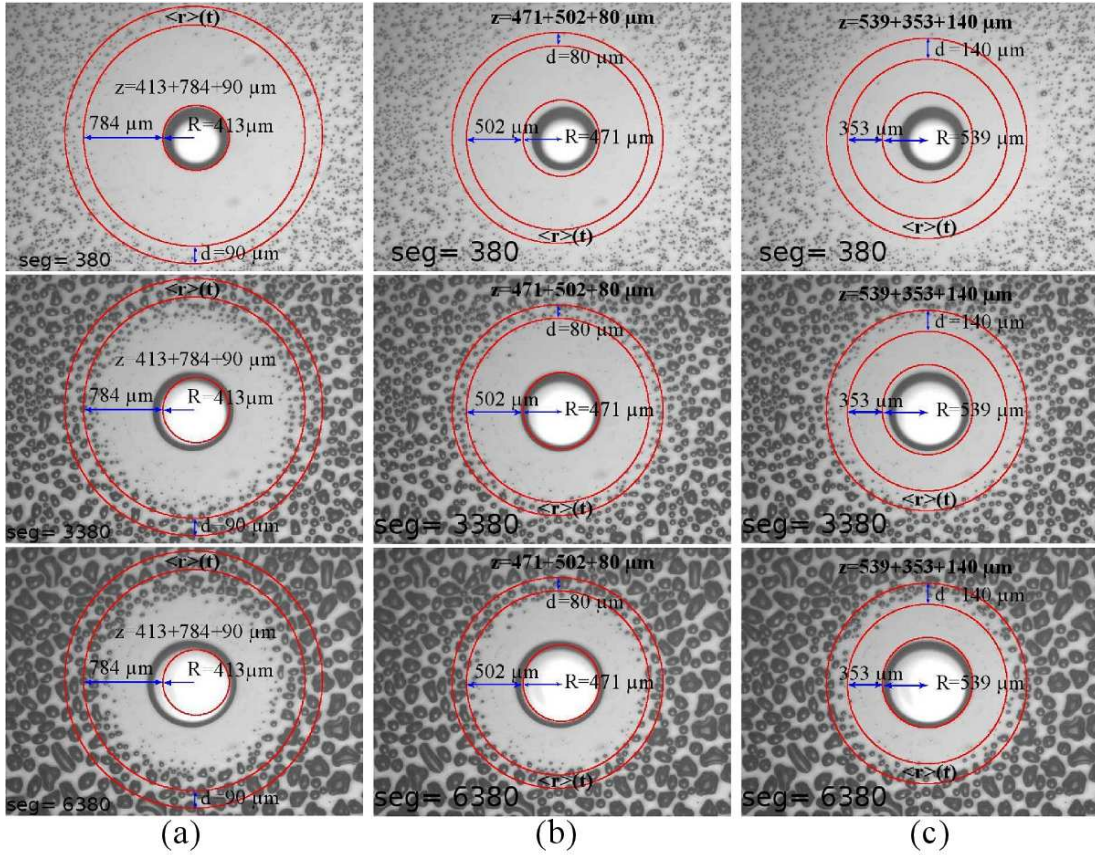


Figure 3.7: Representation of how to compute the $\langle r \rangle$ in terms of the values of $\delta(t_j)$, $R(t_j)$, and d_k . After that, the BF evolution inside the ring is analyzed. The columns (a), (b) and (d) show the $\langle r \rangle(t_i)$ for different rings.

Raoult's law, we write the difference of partial vapor pressure between the salty drop and the surroundings as $\Delta P = P_s - P_{ss} + P_{ss} - \chi P_{ss}$, where the partial pressure for water vapor at room temperature T_R is $P_s = P_{T_s}^{\text{H}_2\text{O}}$. The corresponding partial pressure at the perimeter of the salty drop is proportional to P_{ss} as $\chi P_{ss} = P_{T_s}^{\text{H}_2\text{O}+\text{NaCl}}$. This difference of pressures can be compared with the water vapor flow as:

$$P_s - \chi P_{ss} \simeq \phi, \quad (3.2)$$

where $\chi = (R_0/R)^3$ is related to the salt concentration on the solution, R_0 is the initial radius of the salty drop at the temperature of salt saturation solution ($T = 10^\circ\text{C}$). We assume the flux of molecules ϕ in one instance can be represented by the Equation 3.2 which becomes into $\Delta P \simeq (R_0/R)^3 P_{ss}$ or,

$$\phi \simeq \Delta P. \quad (3.3)$$

The rate change of the number set as a function of the distance to the perimeter of the salty drop is

$$D \frac{\partial n}{\partial r} \Big|_R = \phi \quad (3.4)$$

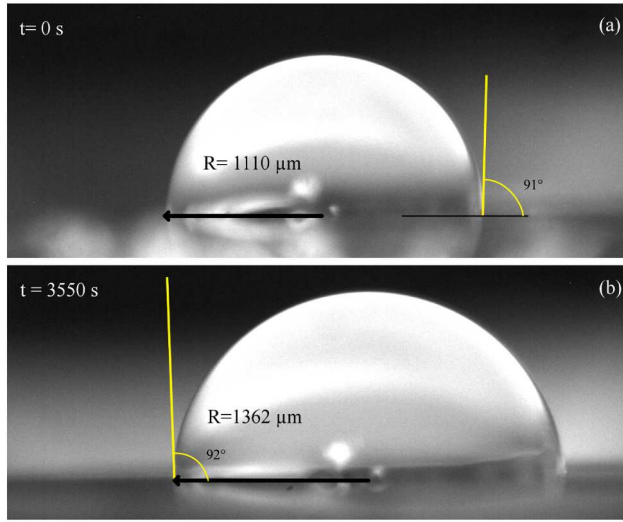


Figure 3.8: This is the lateral observation of the growing salty drop during an experiment with a substrate (ITO) at the temperature of 10°C and a flux of WV of 250 ml/min . A variation of contact angle of $\approx 1^\circ$ took almost 1 hour.

as a consequence, the increment of volume as a function of time is

$$R^2 \frac{dR}{dt} = 2\pi R \Delta P. \quad (3.5)$$

The expression obtained from Equation 3.5 to depict the growth profile of the salty drop is

$$R = (R_0^5 + Bt)^{1/5} \quad (3.6)$$

or

$$R = R_0 (1 + t/\tau_{SD})^{1/5} \quad (3.7)$$

where τ_{SD} is a characteristic time. If we consider the initial time $t_0 = 0$ and $[B] = L^5 \cdot T^{-1}$. This links partial pressure with the increment of water on the salty drop's solution. This last Equation describes very well the salty drop growth (Figure 3.9).

Concerning the depletion zone, we found that it depends on the value of the salty drop radius and time. To obtain this dependence, it is necessary to establish the conditions for the incoming flux from the interior of the depletion zone. Assuming ϕ_o as the flux reservoir of vapor flux ($\phi_o \gg J_{rd}$), now we define the incoming flux for a radial distribution around a half sphere as

$$\frac{2\pi d(rJ_{rd})}{dr_d} = 0 \quad (3.8)$$

and

$$\frac{dJ_{rd}}{J_{rd}} = -2 \frac{dr_d}{r_d}. \quad (3.9)$$

Hence,

$$J_{rd} = J_0 \left(\frac{R_i}{r_d} \right)^2. \quad (3.10)$$

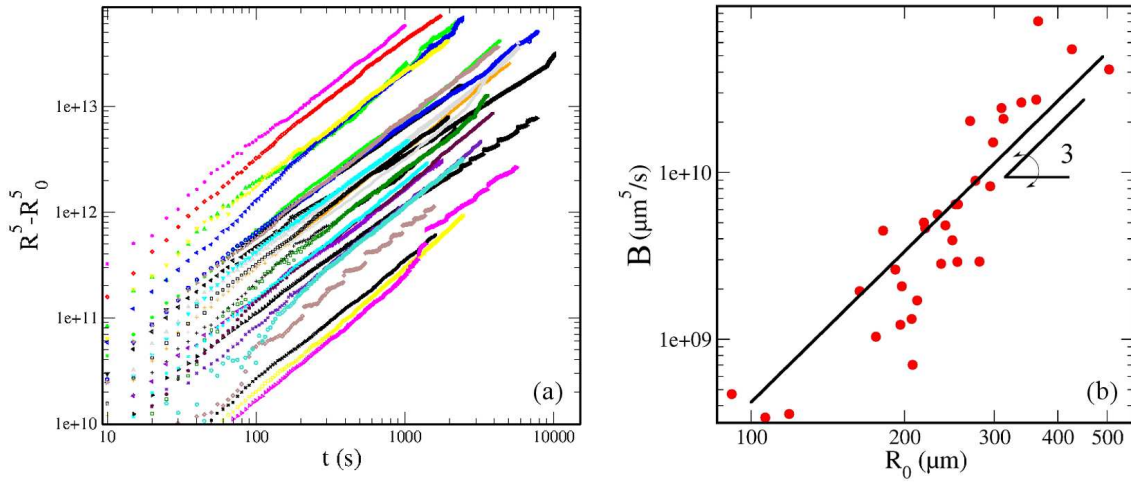


Figure 3.9: (a) The Equation 3.7 was tested on several experiments with successful results. The law of growth fit well. (b) The rate of adsorption of the sink is strongly linked with the initial concentration of NaCl solution and apparently, not with the exterior flux of vapor applied.

where $[J_0] = L^3 \cdot T^{-1}$ is the flux of water molecules incoming to the depletion zone. The rate of change of monomers on the surface can be expressed as the rate of change of the distance δ between the limits of the singularities (perimeter of the salty drop) of the salty drop and the BF pattern. We say $\delta = |r_d - R_i|$ is measured from the center of the droplet at some value of R . It follows to consider the incoming flux expression as the reservoir $[\phi_o] = L^3 \cdot T^{-1}$.

$$J = \phi_o - J_{rd}, \quad (3.11)$$

from this last Equation, I propose add the total flux J which represents the total incoming flux of water molecules to the diffusion equation. The solution of this equation will depict the dynamic of the depletion zone in radial coordinates and time. We can assume that the number of molecules is proportional to the volume of the depletion zone like $n(r_d, t) \propto \delta(r_d, t)$. Also, we assume that those molecules are occupying a volume around the salty drop and the diffusive mechanism is not happening only on the drop contact line, but on all its surface. The boundary conditions to solve the Equation 1.18 are

$$\text{with initial conditions: } \begin{cases} n(r_d = r*, t_0) = n_0 \\ n(r_d = R, t) = 0 \\ n(t = t_\infty) = 0 \end{cases} \quad (3.12)$$

where r^* corresponds to the distance between the center of the sink and where the BF begins. At the initial time, the number of molecules is maximum. Due to the flux at the contact line R , the number of monomers is zero. When a long time has passed, the depletion zone is small because the concentration of salt in the drop has reached a minimum, and the salty drop behaves like any other drop in the BF pattern. The radial part of the diffusive Equation can be written

$$r_d^2 \frac{\partial^2 R^*}{\partial r_d^2} + r_d \frac{\partial R^*}{\partial r_d} + r_d^2 (\phi_o - J_{r_d}) R^* = 0, \quad (3.13)$$

where R^* is the distance between the perimeter of the salty drop and the beginning of the depletion zone. We have dealt with the form of n in the Equation 1.18 as

$$\delta = R^*(r_d)T(t). \quad (3.14)$$

This function δ times a constant represents the number of molecules as a function of r_d . As we will see, δ is the width of the depletion zone as a function of the salty drop's radius and time. Solving the radial part for the Equations 3.14 and 1.18 we obtain directly the Bessel's function. So, the expression for R^* is becoming,

$$R^* = \delta_0 r_d^k \left(1 - \frac{r_d^2}{2^2 1!(k+1)} + \frac{r_d^4}{2^4 2!(k+2)} - \frac{r_d^6}{2^6 3!(k+3)} \dots \right) \quad (3.15)$$

with $k = 1, 2, 3, \dots$ those values could be interpreted as how J_{r_d} is compared to ϕ_o , and taking into account, the vapor is totally saturated 100 % and $J_{r_d} < \phi_o$. Also for calculation purposes, r_d is defined as a dimensionless variable and the only physical meaning is δ_0 . The time function is easily obtained from

$$\frac{dT}{dt} + T(\phi_o - J_{r_d}) = 0 \quad (3.16)$$

and immediately is obtained,

$$T(t) = A \exp \{-\alpha J t\} \quad (3.17)$$

and $[A] = T$. The complete solution is obtained by multiplying the Equations 3.15 and 3.17

$$\delta(r_d, t) = A \delta_0 \exp \{-\alpha J t\} r_d^k \left(1 - \frac{r_d^2}{2^2 1!(k+1)} + \frac{r_d^4}{2^4 2!(k+2)} - \frac{r_d^6}{2^6 3!(k+3)} \right). \quad (3.18)$$

To fit this solution with our observations of δ , on this last equation we have substituted $r_d = C((R_i - e_0)/r^*)$ where $e_0 > R_i$, C is the intensity of J_{r_d} and $r^* = 1 \mu\text{m}$ a unit length. It has been assumed that the distance e_0 corresponds to the distance where the flux reservoir ϕ_o is. For our purpose is enough to take into account the third expansion of the Bessel's polynomial, and to abbreviate, I write the solution as

$$\delta(r_d, t) = A R^*(r_d) \exp \{-\alpha J t\} \quad (3.19)$$

The Equations 3.7 and 3.19 fit well on R and δ as it is shown in Figure 3.10. The initial value of the salty drop's radius R_0 is very important to determine further stages of the system and to determine the difference of the partial pressures inside the depletion zone. Likewise, the initial value establishes how long the humidity sink will take for the adsorption of WV. It could matter an important aspect of hygroscopic property of a given substance or solution. A sketch of the results corresponding to those Equations are presented in Figure 3.11. With the relations of the fitting parameters and the physical measurements we are going to start to take in account which

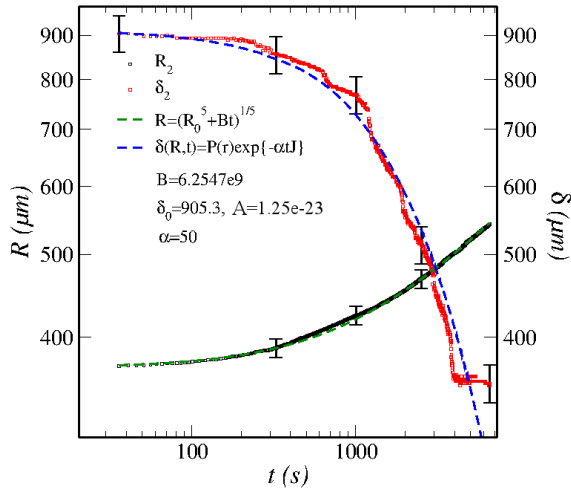


Figure 3.10: The evolution of the salty drop radius and the depletion zone are depicted and fitted. α and A are fitting parameters.

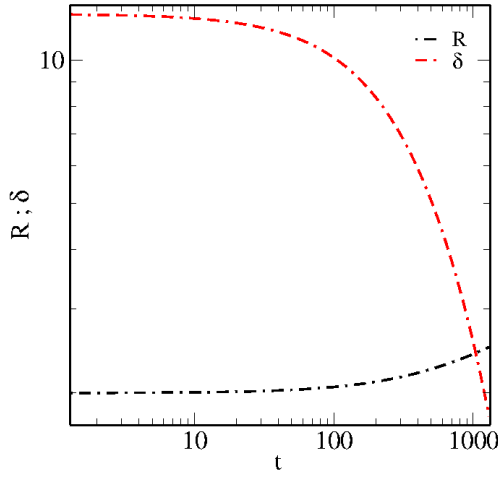


Figure 3.11: The parameters for R (Equation 3.7) are $R_0 = 2$ and $B = 5 \cdot 10^{-2}$. For δ = (Equation 3.19) are $i = 1$, $A = 0.1$ and $\alpha = 9 \cdot 10^{-3}$ and $\delta_0 = 110$.

of those values are relevant to describe the flux and the pressure gradient. It is left to compare all the parameters to reject or consider them. For example, one may think that the flux of mass should be related with the total amount of vapor flux. Otherwise, if we look onto the parameters displayed on the Table 3.1 we cannot say too much about whether there is a tendency or not. Perhaps, the interaction with fluctuations of temperature or with the roughness of the substrates are the main cause. Nevertheless, this understandable and simple model gives a first insight to the problem.

3.3.1. The Flux and the Depletion Zone

The last reasoning and its interpretation (from Equation 3.8 to Equation 3.19) are results that lets us to discuss about the relevant parameters for the depletion zone and the flux of mass to the humidity sink. Besides, this analysis let us to link the flux of WV ϕ_o with the time crossing time t_f when $\delta = R$. For this, it is necessary to distinguish what the values of ϕ_o are unknown while the values of Φ_0 are for the experimental settings (vapor flow). Other interesting possibility is to compute the values of the pressure as the distance is changing on the interval δ . The solution of Equation 3.19 (or more general, the Equation 3.18) fits fine for many complex situations where the δ profile is not easy to understand. The Figure 3.12 shows values of R and δ obtained from measurements of the initial conditions and passed through the Equations 3.7 and 3.19. It follows to introduce the difference of pressure as a part of the description of the depletion zone by the parameter B (Equation 3.7) and the values of vapor saturation for water HVAC-CVC (Figure C.1). The vapor pressure for WV at room temperature (23°C) is $P_s = 2.9 \text{ kPa}$ and near the substrate where the WV condenses at 10°C is $P_{ss} = 1.3 \text{ kPa}$. The pressure for a salt saturated solution at 10°C is 0.921 kPa . The relation for partial pressure $\Delta P = P_s - \chi P_{ss}$ will be computed through the values of the position on the depletion zone as a function of R^* .

Even though, we still do not have experimental information about how exactly ϕ_o , J , and the rest of the parameters are. However, from the fitting values we can estimate how may be the relation between the flows, pressures and the dynamical measurements. We can look into the crossing time t_f between δ and R to find a relation with the experimental vapor flux. Meanwhile A , and α are free fitting parameters. The pressure gradient profile is computed in the spatial domain. The spatial domain is understood as the space between R_j and δ_j measured at time t_j (evaluated on Equation 3.15). If the value of the pressure at the perimeter of δ_j is the vapor pressure at room temperature, the corresponding value is $P_s = 2.9 \text{ kPa}$. Towards the salty drop perimeter, the partial pressure decreases until the value χP_s .

The proposed model and the hypothesis used here worked fine. The parameters for t_f and α (Table 3.1) are sketched. They represented the evolution of depletion region around the salty drop (see Figures 3.13 to 3.17). We compared the other fitting parameters, and the stronger relations are the constant diffusion A vs Φ_0 , R_0 , and the values of α and the crossing times t_f . The fitting parameters and the experimental values are shown in the following Figures 3.18 to 3.20.

Despite some parameters do not present a perfect recognizable tendency, that does not mean that any relation does not exist. In such cases, other measurement would have been required. The inset of Figure 3.18 it is shown a value totally out from that tendency. Other non-linear parameters like dimensionless A (Figure 3.19) whose physical meaning comes out with the product $A\delta_0$ on the Equation 3.19. The cut off time t_f must be related with the water vapor flow. The Figure 3.20 exhibits how t_f increases too. The corresponding fitting parameter on the time solution decreases systematically. It means that, there is a clear tendency which agrees with the experiments.

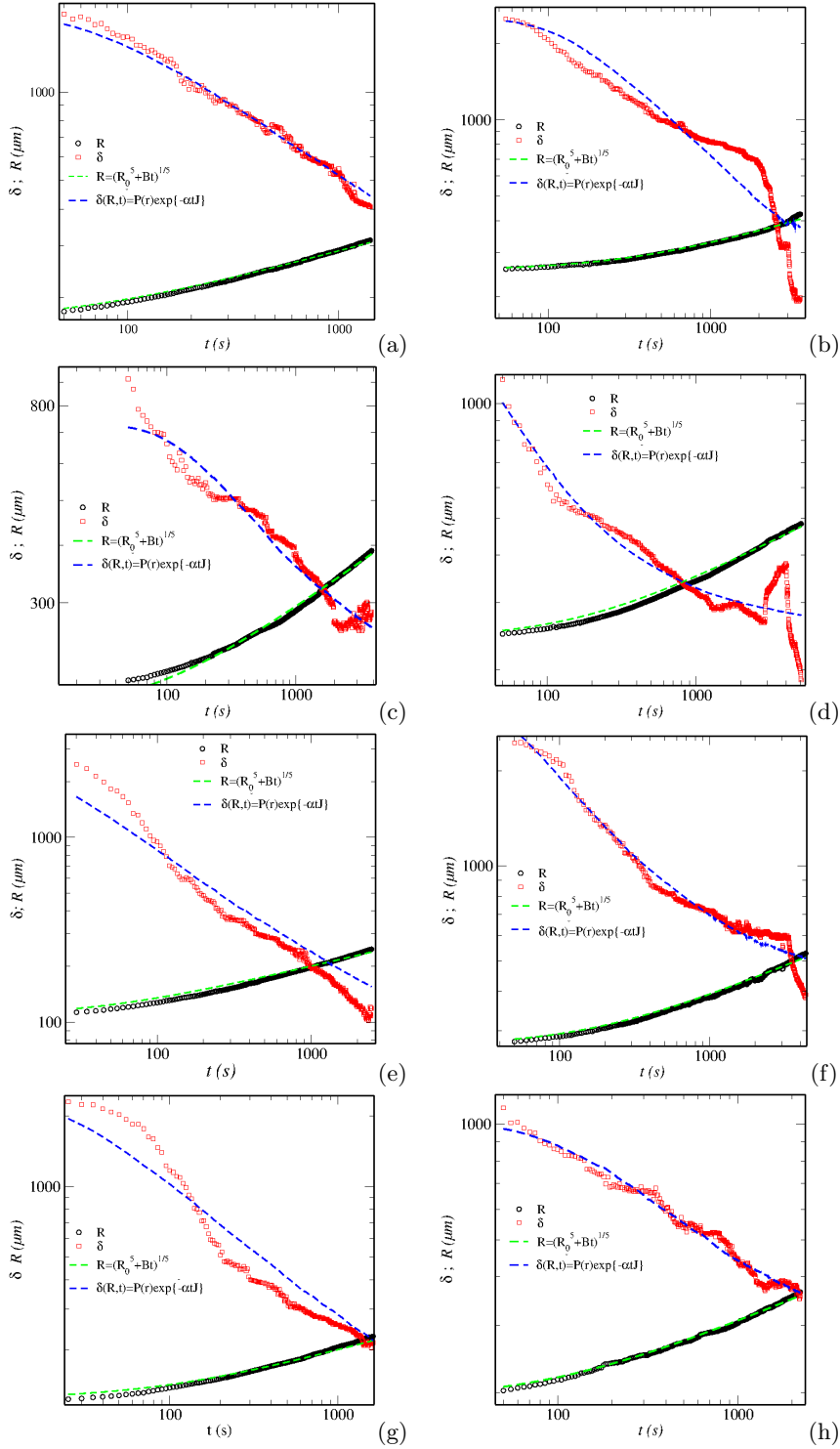


Figure 3.12: Measurements of R and δ are shown with their respective fits . From (a)-(h) the flow is respectively 200, 165, 155, 150, 135, 125, 120, and 115 (ml/min).

3.3.2. The Difference of Pressure around the Salty Drop

We are going to use the spatial part solution of δ to obtain the profile of the pressure inside the depletion region (Figures 3.21). The spatial domain has been redefined per each time and

No.	R_0 (μm)	δ_0 (μm)	$B \pm 0.3 \cdot (10^9 \mu\text{m}^5 \text{s}^{-1})$	$t_f \pm 0.5 \text{ sec}$	α (m^{-3})	$A \cdot 10^{-14}$	$\Phi_0 \pm 0.5$ (ml/min)
1	113 \pm 11	2478 \pm 245	0.3	1000	74.84	0.633	135
2	123 \pm 12	2302 \pm 230	0.3	1400	57.67	0.346	120
3	203 \pm 20	1101 \pm 110	25.3	2220	21.044	0.609	115
4	204 \pm 20	2000 \pm 200*	20.7	1630	51.107	0.616	155
5	208 \pm 20	1857 \pm 186	0.0	125	770.73	0.645	140
6	215 \pm 20	2472 \pm 247	16.4	1645	72.82	0.670	145
7	220 \pm 22	3000.0 \pm 300*	41.0	2350	28.06	6.939	190
8	243 \pm 24	5000 \pm 500*	52.8	4120	11.02	0.834	140
9	248 \pm 25	981 \pm 98	45.8	830	31.06	0.863	150
10	249 \pm 25	2332 \pm 233	38.8	1750	53.63	0.877	170
11	257 \pm 26	2505 \pm 250	27.6	2550	43.09	0.932	165
12	276 \pm 28	5000 \pm 500*	78.5	3570	10.02	1.090	125
13	306 \pm 31	2000 \pm 500*	173.3	585	140.29	1.404	180

Table 3.1: Constants and parameters used to reconstruct the $\delta(R, t)$ function. The headings mean the initial radius, the initial observable length of the depletion zone which are physical measurements, B has been discussed above: the value in the fourth row is reported as it was computed. t_f is the time of crossing of the δ and R values. α is used as a cutting parameter on the timing part of the Equation 3.19. A is related to the diffusive coefficient. δ_0 is the initial separation between the salty drop perimeter to BF. Φ_0 is the vapor flow. The values of δ^* were replaced in order to fit the curves, the real values are: 700.5, 1032.5, 2379.6, 2461.5 and 681.13 μm respectively.

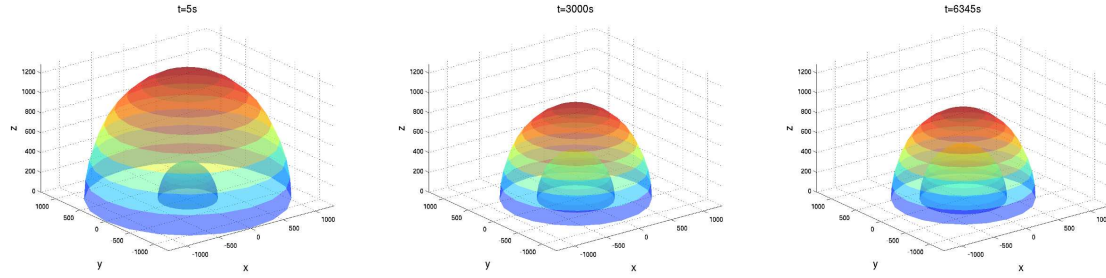


Figure 3.13: If we assume the water molecules can be distributed around the salty drop, this view may describe such distribution of monomers. The images are produced with the experimental values of the Figure 3.12.

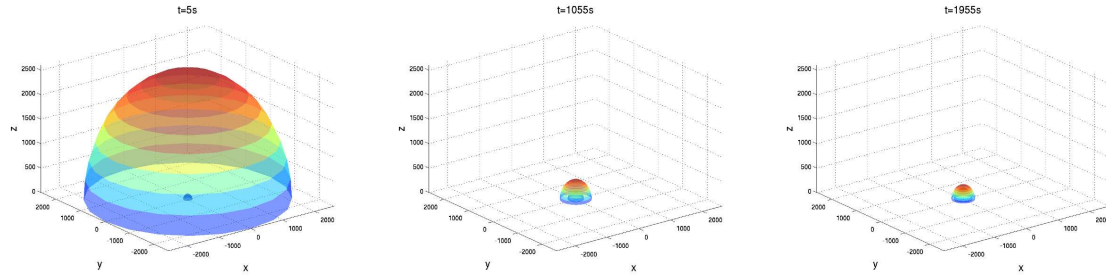


Figure 3.14: View with experimental fitting parameters correspond to the Table 3.1 (row 1).

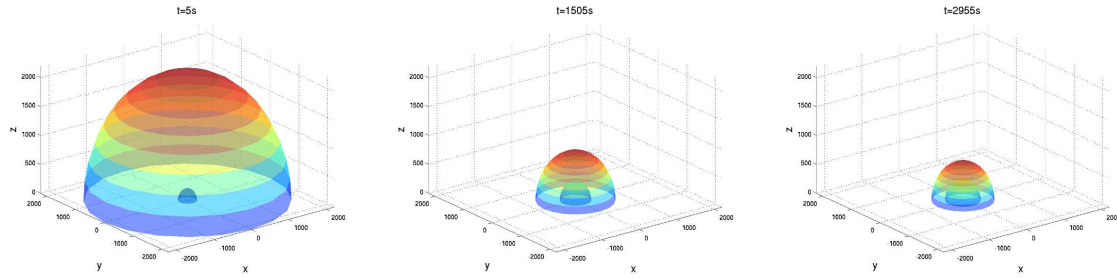


Figure 3.15: View with experimental fitting parameters correspond to the Table 3.1 and row 3.

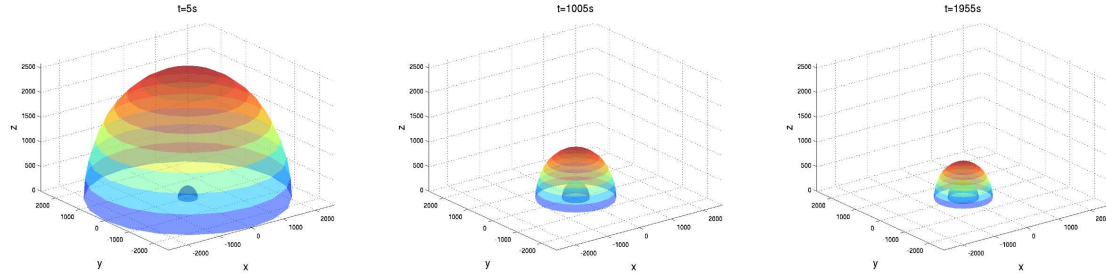


Figure 3.16: View with experimental fitting parameters correspond to the Table 3.1 and row 10.

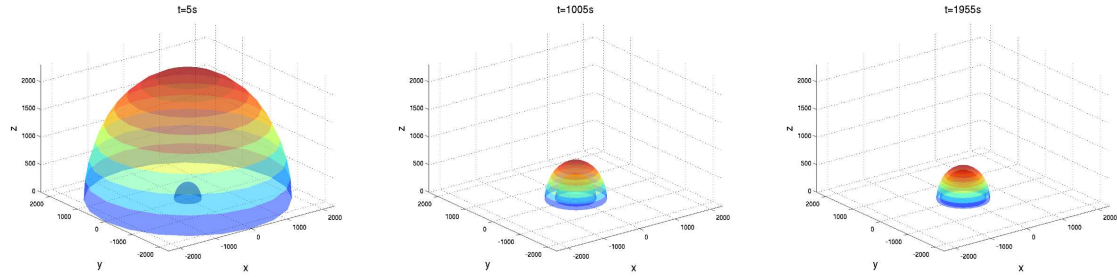


Figure 3.17: View with experimental fitting parameters correspond to the Table 3.1 and row 13.

the minimum encountered values of the pressure correspond to the partial pressure for the salt solution. The Figure 3.23 shows the solution of the gradient of n for δ 's profile. Also, it can describe the distribution of the values of the pressure (Figure 3.22).

The initial values of the pressure at the beginning of the curves (Figure 3.22) represent the values of the partial pressure (Figure 3.23) at the perimeter of the salty drop. As this perimeter increases, the partial pressures χP_{ss} increases until it reaches the value of P_{ss} .

To finish this section, I should add that even the relation of χP_{ss} as a function of time (Figure 3.24) is unknown. Right now, an affordable explanation is to say, that the phenomenon of condensation with this characteristics is very complex, and the relations between the descriptives parameters are not totally obvious. Such is the case of the flux and the temporal constant in the

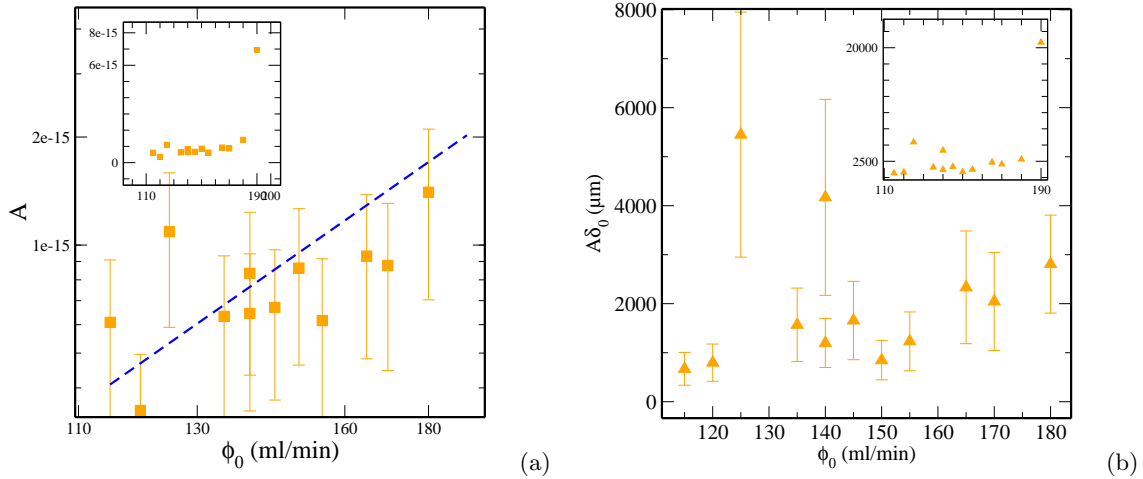


Figure 3.18: Initial δ_0 is observed when the water vapor flows Φ_0 into the condensation chamber. (a) and (b) exhibit a relation. For some part of the fitting values we can appreciate an increasing tendency (blue dashed line), but we are not totally sure to have a solid relation. Inset: we show whole the plot to signalize there is a value totally out of range of the parameters.

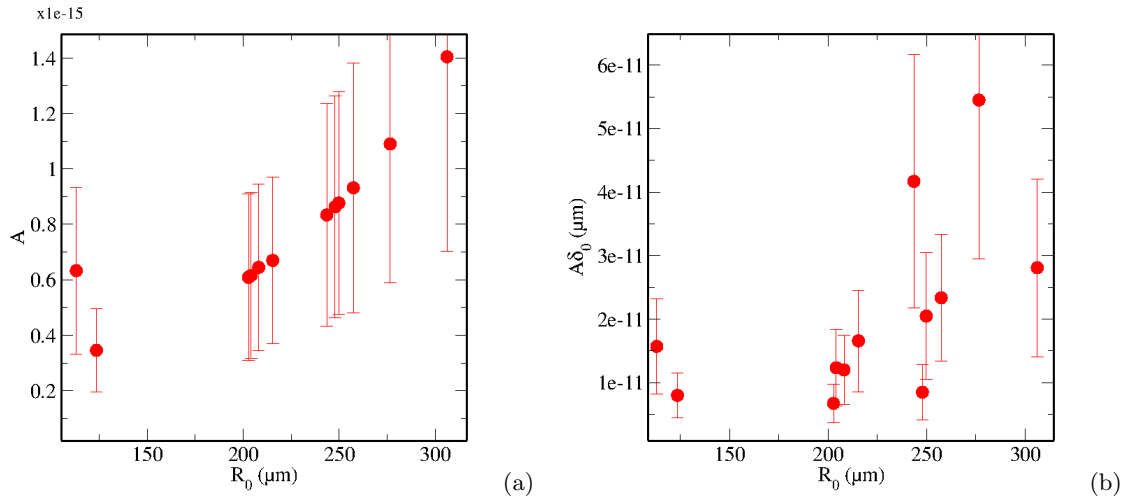


Figure 3.19: As a function of R_0 , fitting parameters (a) A and (b) $A\delta_0$.

description of δ where the values are related but far from the linearly tendencies.

3.4. Drops Pattern Around the Humidity Sink

In one limit of the depletion zone occurs the BF's pattern formation. According to the last section, the value of the vapor flux is higher on the vicinity on the salty drop than in other places. As a consequence of this, the partial pressure of saturation inside is smaller than the pressure outside. Of course, the salty drop pressure is smaller than any other droplet of the BF's at the limit of the depletion zone. That means, the necessary pressure conditions to produce

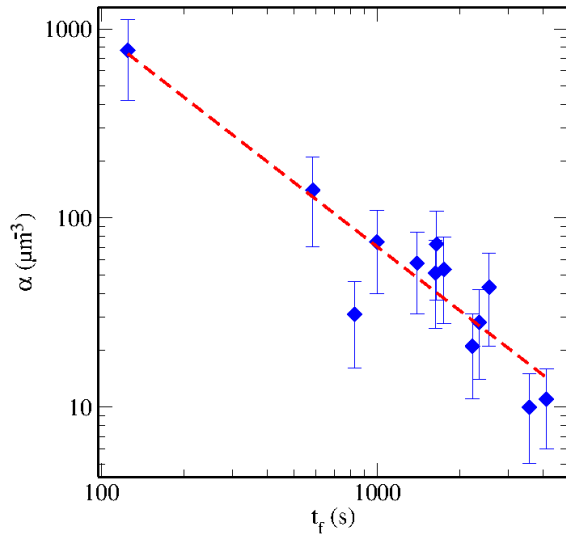


Figure 3.20: The crossing time t_f and the parameter α . From the Equation 3.19 as the mass transferred reduces the time.

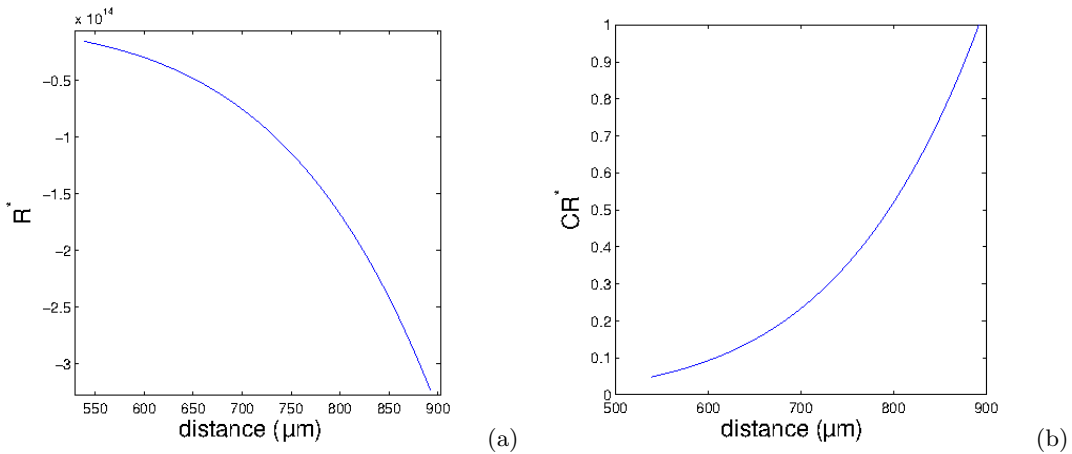


Figure 3.21: (a) The polynomial function (Equation 3.15) is evaluated on the domain $(R_0, R + \delta_0)$. (b) This function fits with boundary conditions where the pressure at the end of depletion zone is 1.3 kPa and the beginning of the salty drop is 0.921 kPa.

condensation and to form droplets over the substrate is given exactly at the end of this area. The analysis is discussed in [22] and in the Chapter 1. The values of the pressure over the BF pattern can be represented through the concentration values (inverse of the mean radius of the droplets during the second stage of growth). In this section, we study the mean radius inside a certain area out from the depletion zone.

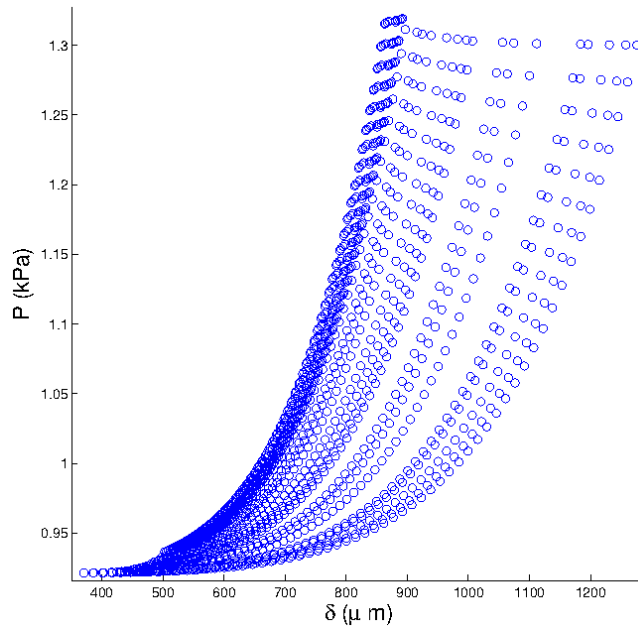


Figure 3.22: Profile of the pressure between the perimeter of the salty drop R and the limit of the depletion zone δ is obtained for different times (Figure 3.10)

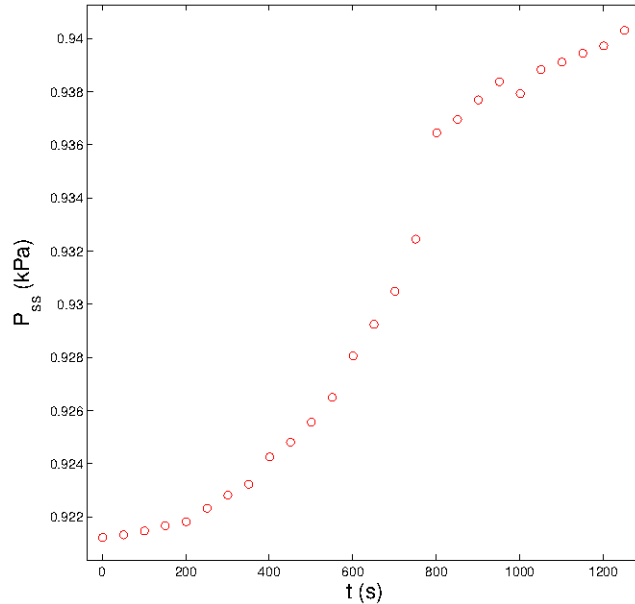


Figure 3.23: Values of the vapor pressure of the salt solution.

3.4.1. Mean Radius of the BF's Droplets

At the end of the depletion zone, the droplets grow normally. Their average radius for the second and third stage remain like $\langle r \rangle \sim t^{1/3}$ and $\langle r \rangle \sim t$ respectively. However, they do at different times. This is because, as the depletion zone is shrinking while the BF gains area. We

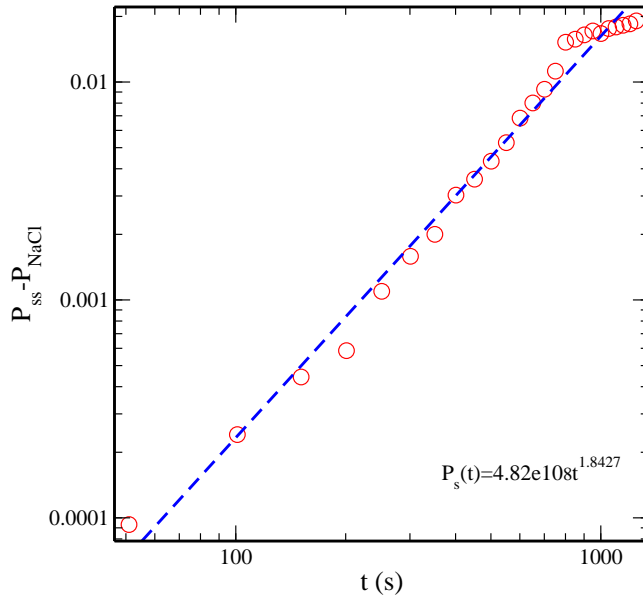


Figure 3.24: The difference of partial pressures for supersaturated vapor on the BF and in the perimenter of the salty drop.

must remember, the condition to produce condensation is due to the difference of temperatures which induces to a difference of pressures. On the surroundings of a recently BF pattern formed (second stage), the pressure has a close value of 1.3 kPa which corresponds to the vapor pressure at the temperature of the substrate. As we said before, this set a upper condition for the pressure gradient on the depletion zone. Now, we are going to present some measurements and calculations of the mean radius at different distances from the depletion zone. To observe exactly how the profile of the pressures in the BF side is, we use the fact that the concentration is proportional to the pressure, and that the concentration is

$$\Delta c \sim t^{-1}. \quad (3.20)$$

The values of concentration will be extracted from the region where the power law $t^{1/3}$ is valid. Such that the Equation 3.20 can be handled as $(A/\langle r \rangle)^3 = t^{-1}$ where A is a constant and the cubic inverse of the average radius is the volume of water droplets at certain time t . This representation is very convenient to find the amount of mass transferred from the vapor system and to the drop's carpet. For the concentration values, it is expected to observe (as the ratio ζ/δ increases) an exponential profile. For the rest of the spatial domain, the pressure gradient could fit on the assumption discussed on Section 3.3.

We do an inspection of the histograms of the droplets size for each ring defined. The Figure 3.25 shows the histograms for different ratios of ζ/δ (Equation 3.1). We expected such dispersion on the data because the number of droplets per ring is not very large (the small width of the ring acts like a size filter). There is a decay on the exponent at the coalescence stage which is in agreement with [11]. The two stages of BF evolution are presented in Figures 3.27. The spatial domain of computation of $\langle r \rangle$ is determined for the position of the rings (as is shown in Figure 3.7) and the duration expected depends on whose value of δ .

The droplets placed at the end of the depletion zone have certain concentration values and their corresponding WV pressure value. We may think that the connection with the pressure gradient on the BF and in the depletion zone should be a continuous function. Now, we are going to develop the analysis in the sense of connecting values of concentration with their corresponding pressure values. But first, we will obtain a complete sketch of gradient of pressures dealing with the pattern at different stages. As we will see, from the calculation of the mean radius in specific places, the gradient of concentration can be obtained directly also, the pressure gradient. The mean radius of our interest is one defined on the second stage because the density of droplets is proportional to t^{-1} , or $\Delta c \sim \langle r \rangle^3$.

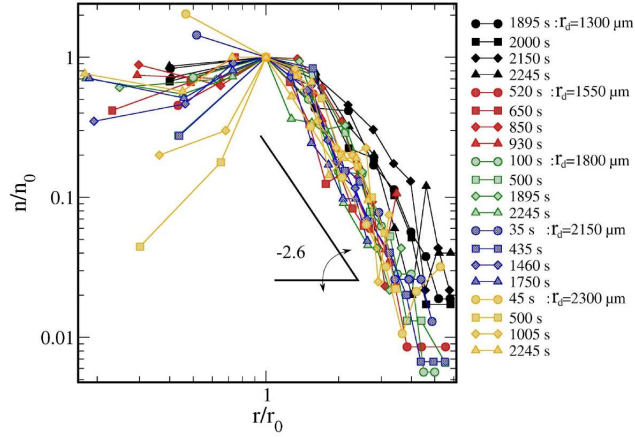


Figure 3.25: The algorithm (described in subsection 3.2.2) helps to calculate the histograms of the size of droplets and their population.

3.5. The Profile of the Pressure Gradient

From the Figures 3.28 and 3.29 the values of $\langle r_o \rangle$ are substituted on the expression for t^{-1} or $(\langle r_o \rangle/A)^{1/3}$. It is necessary to set the minimum value as the pressure of WV at the temperature of the substrate. The spatial region is set like $r_d/(\delta + R)$, where r_d is an independent value of the position between the perimeter of the salty droplet and the very end of the depletion zone (measured from the center of the salty drop). pattern and the depletion zone, even the pressure values of the salty drop can be matched in one plot (Figure 3.30).

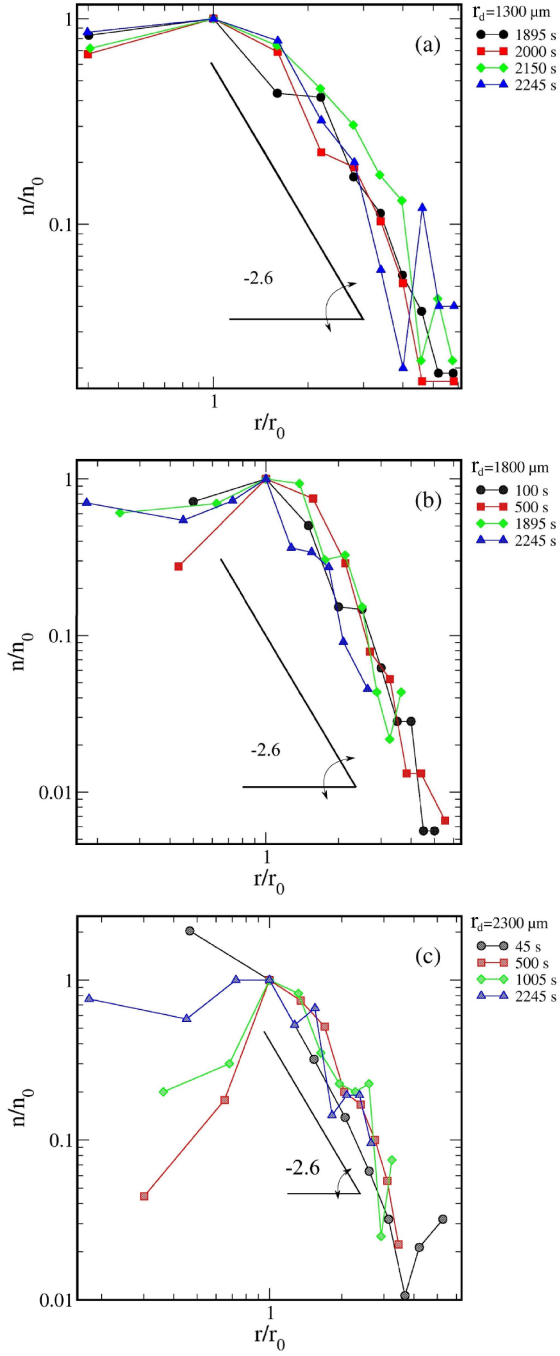


Figure 3.26: The plots correspond to histograms for different rings at different distances. According to the introductory chapter, the decay on the number of droplets corresponds to the increment of their size of t on the coalescence stage. The dispersion observed in the statistic calculation is due to the number of droplets counted are so few and because we sought the average radius of the droplets in the stage $t^{1/3}$ the corresponding size were favored on the rings size selection.

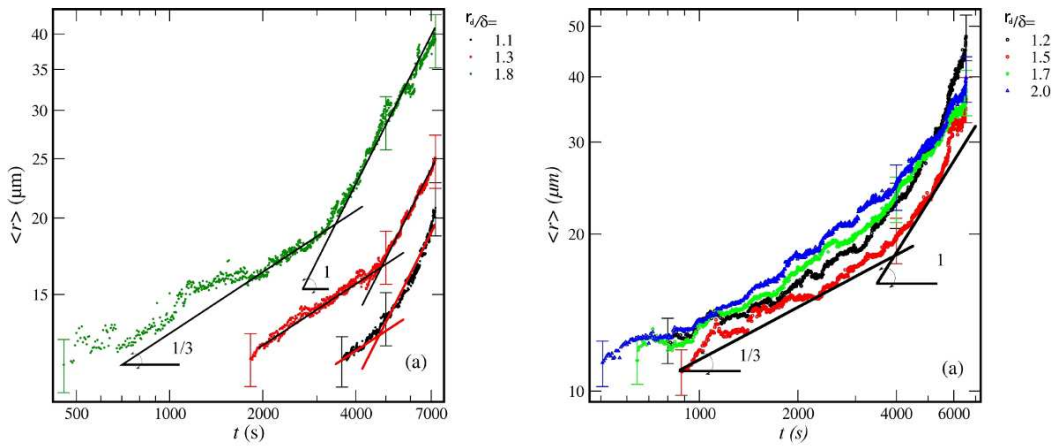


Figure 3.27: The mean radius $\langle r \rangle$ for two different experiments are shown.

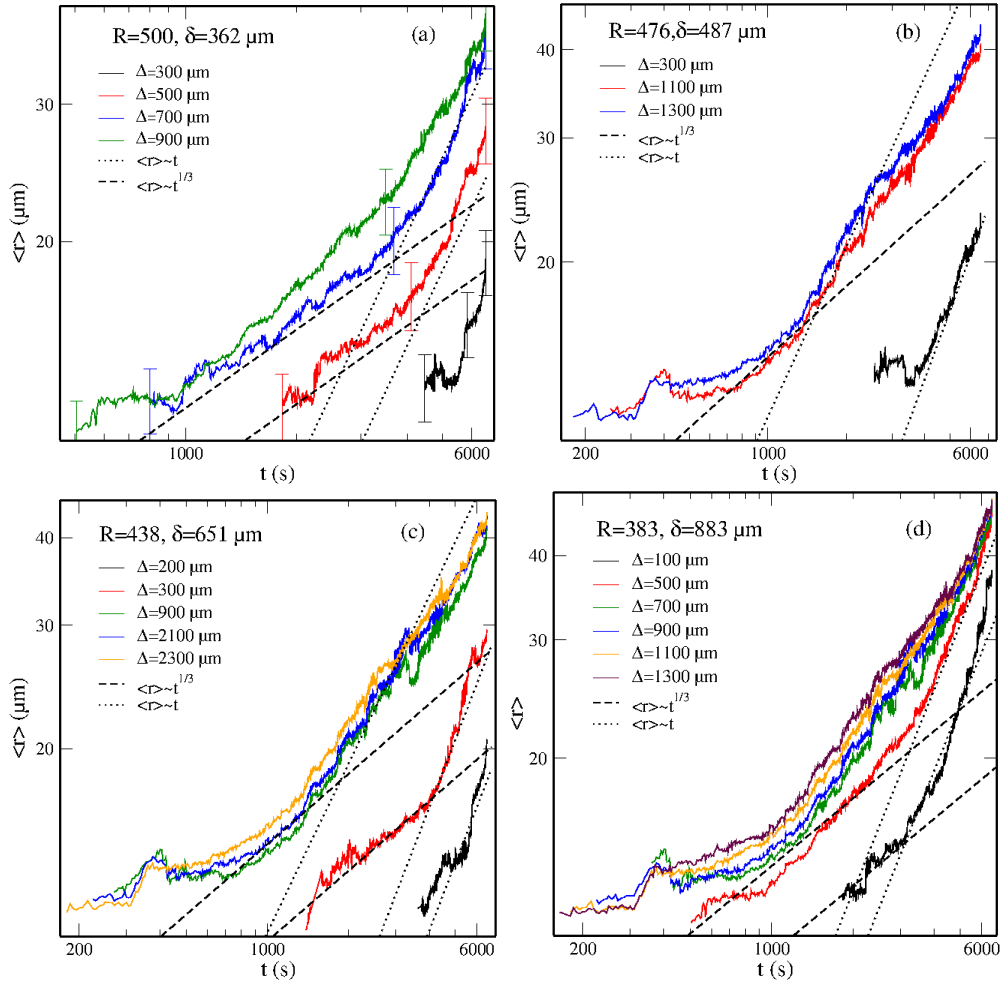


Figure 3.28: Mean radius for different widths of the ring.

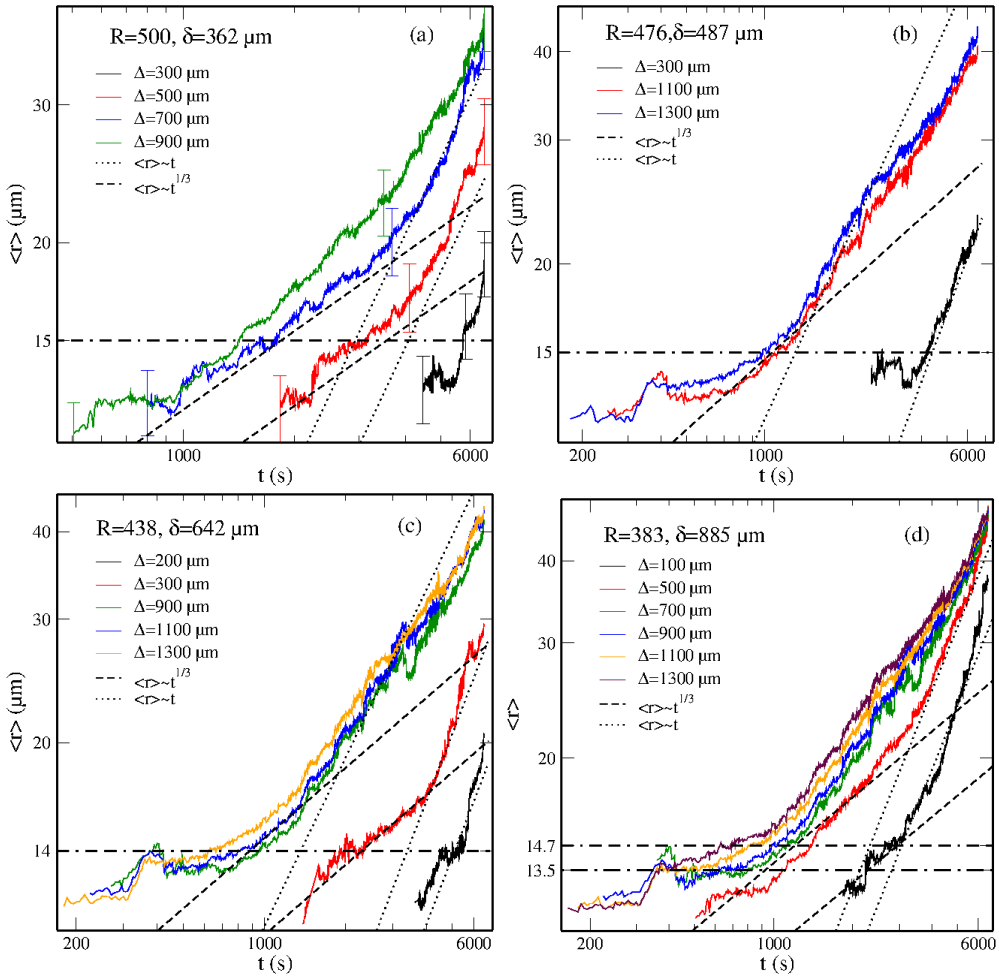


Figure 3.29: The calculation of Δc is obtained from a shared value of $\langle r_0 \rangle$.

3.6. Concluding Remarks

1. The reason because there are not drops in the depletion zone is because the vapor is not supersaturated and it cannot condense.
2. A mathematical formulation for δ and R profile was obtained. This formulation is settled on the assumption that the depletion zone around the humidity sink is due to that the water molecules are not only near the substrate, but also they are surrounding the humidity sink.
3. From the solution of the diffusive equation we found a tendency between the incoming flow of water vapor to the condensation chamber and the cutting times where the depletion zone. As the flow of water vapor increases, the cutting time values decrease.
4. This model let us to compute the profile of the pressure inside the depletion zone.
5. The values of the pressure from the measurements of the t^{-1} at the second stage were matched successfully with the depletion zone's pressure profile.

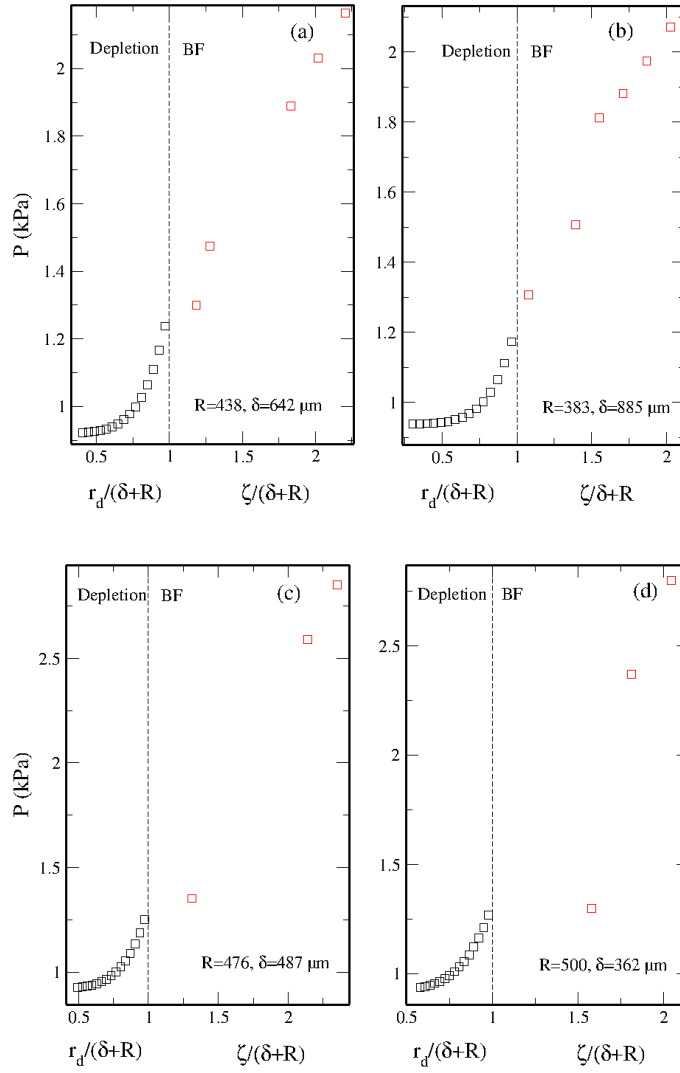


Figure 3.30: The profile of the pressure as a function of ζ , R and δ define a spatial domain. The reason because there are not drops in the depletion zone is because the vapor is not saturated there and it cannot condense.

Chapter 4

Breath Figure under Solidification Temperature of Water

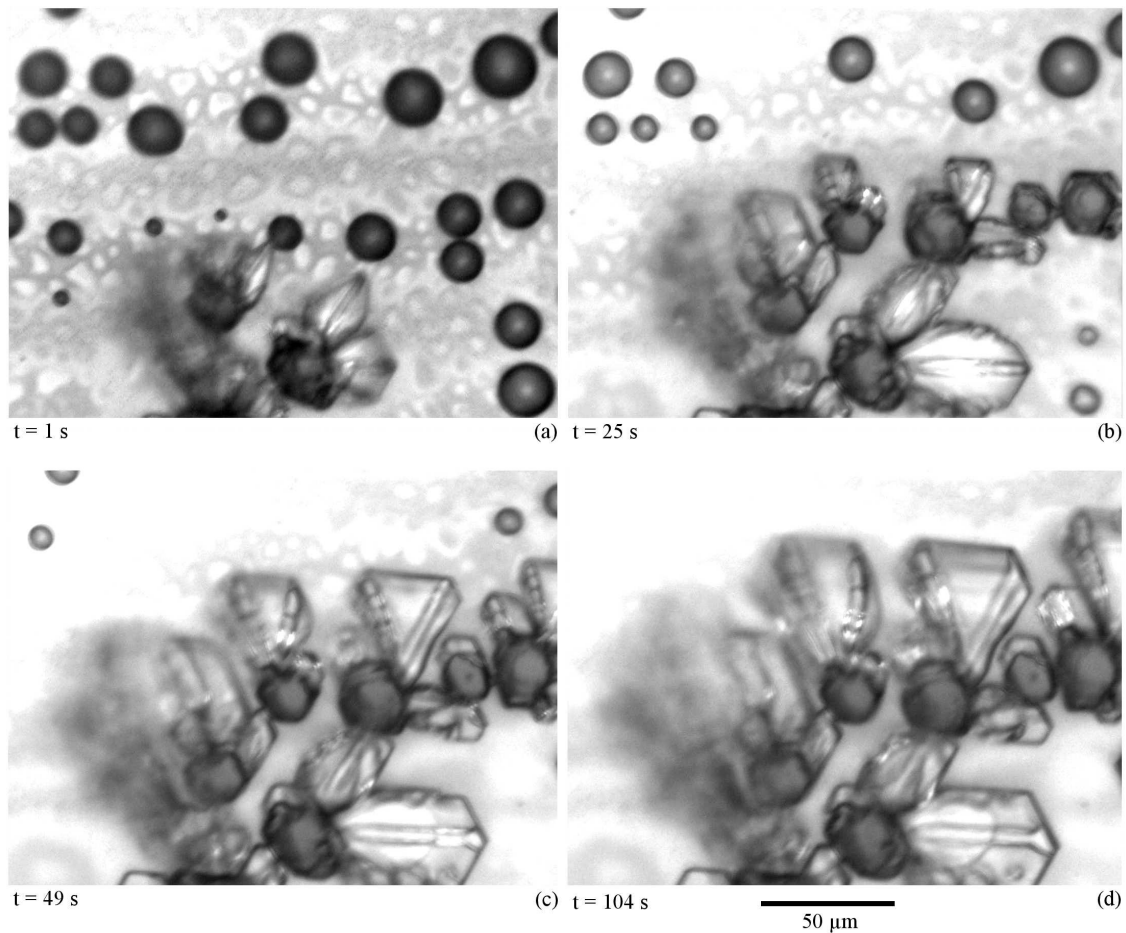


Figure 4.1: Hexagonal ice dendrite at $-10\text{ }^{\circ}\text{C}$. The ice grows at expenses of the water droplets.

4.1. Introduction

From ESPCI-Paristech Paris, France Dr. Prof. Daniel Beysens conceived the project. He, Anne Mongruel and W. Gonzaéz Viñas designed the experiment. The design of the experiment was basically created to investigate the intervention of the Breath Figure phenomenon and the formation of frost. Water will always be a complex subject of study. It is well known that water presents a maximum of density when its temperature is near 4.2 °C. Of course, when the temperature decreases until 0 °C and it transits to solid phase its density decreases too. Inspired on this physical characteristic, and wondering how the molecules of water behave to produce this change on the values of density, some works have been done since 1980. They have attempted to reach lower temperatures under -5, -30, -45 °C in order to study the physical and thermal properties of density and heat capacity¹ before the solidification [46]. Nowadays, the temperature has been decreased in a wide range of 0 to -120 °C. "Under -120 °C is a land of no men." [47]; I extracted from this last citation the next paragraph because I found it really enlightening: "The ability to supercool water well below the T_h ² by confining it in nanoscopic pores can therefore provide a useful loophole. Chung-Yuan Mou of the National Taiwan University in Taipei has refined the fabrication of silica nanotube assemblies, similar to those used as catalysts for cracking hydrocarbons, to reduce their diameters to 1.5 nm. Using these nanotubes as sample containers that suppress the freezing of water, Mou, Sow- Hsin Chen of the Massachusetts Institute of Technology and co-workers have been able to explore several properties of deeply supercooled water. Building on this work, Mou, Chen." As it can be noticed on last paragraph citation, the methodology to study supercooled water can involve a simple experimental device or very costly facilities unaffordable for many research groups. Other research is focused into thermal properties like heat transfer [48]. The heat conduction property of supercooled water is interesting to substitute environment harsh substances used on heat exchangers [49]. More in the scope [50], that content is about to the theoretical and experimental research on frost production and the interaction with surfaces. B. Na and Ralph L. Webb quantifies the supersaturation of humidity on air and the supersaturation degree as a function of the surface energy. Because the frost formation is very nice to observe, but it is not for some instruments on exteriors, there exists an industry dedicated to avoid the frost formation, and to the development of ice phobic surfaces. In that orientation, experimental research like [21, 51] are specialized to find out the process of nucleation of ice in at very small length scales. The interest arises on the formation of clouds and the further nucleation process. Moreover, the interaction with different phases when they coexist are basic on the comprehension of climate [52]. Concerning the nucleation and frost formation, there are many interesting researches attempting to understand what perturbations drive the supercooled water to solid phase, and what kind of macroscopic parameters are responsible of the phase transition [15]. In this sense, the Wegner-Bergeron-Findeisen (WBF) process is used to understand the nucleation and growth of ice in clouds, where the vapor, solid, and liquid coexist. This process explains and describes the ice growth at expenses of evaporating liquid droplets [19].

At the beginning, we expected to observe something related to the snow falling, or the spontaneous and instantaneous freezing of the water vapor. Also we expected the formation of some crystals like dendrites, or formation of hexagonal flakes. That observations had not happened in

¹Only ultra pure water can hold this characteristics because it does not have nucleation sites.

²Homogeneous nucleation temperature defined in a range of -12 to -40 °C.

that way! Then, we started to look for something wrong. The first change on the experiment was to dry the condensation chamber. We flowed air that has been circulated first by silica-gel then, we decrease slowly the temperature until $-13\text{ }^{\circ}\text{C}$. This attempt was not enough to remove the observation of a BF pattern. Then, we decided to reduce the temperature of the water vapor putting the flask container of ultra-pure water in the same temperature bath used to dissipate the heat from the Peltier element. We could get a temperature of water vapor of $13\text{ }^{\circ}\text{C}$, but this attempt was unsuccessfully too in the sense of obtaining snow or instantaneous solidification of water vapor. Then, we decided to keep going with the observations, trying to figure out what it was wrong on the configurations. At a very weak flow, we observed a very stable and long second stage of a BF pattern and suddenly, a transition to liquid-solid phase in the down left corner of the microscope that propagates for all the pattern. Then, we were very enthusiastic with the beautiful ice crystals. Scanning around on the sample we watched dendrites flakes and droplets of liquid water (Figure 4.1). This experience was very promising and we wanted to reproduced again, and again to follow the propagation and, to observe the formation of the big crystals. Many questions have arisen at that time, for example, why does the phenomenon trigger the freezing process always near the corners? Why do the droplets remain liquid? We tried to reproduce several times, variating the temperature of the substrates to find a limit on the temperature condition. The condensation is a heating process, and perhaps the latent heat of liquid drops was enough to endure the change of state to solid phase. Yet, some liquid droplets were still observed in liquid phase for long times. They were spread on the surface without becoming ice. When we had become skilled reproducing the experiments, we tried to observe the contagious of one solidified droplet to another, and we observed two possibilities: if the droplet is close enough to the recently solidified drop, then occurs the ice contagious. The other possibility is that the drop evaporates. We can observe when water is supercooled (under $0\text{ }^{\circ}\text{C}$ at open atmosphere) on the coexistence of solid and vapor phases outside of thermodynamic equilibrium. So, we have found a new proceeding of propagation of water in 2-D surfaces by a percolation process.

4.2. Experimental Set Up and Procedures

The experimental set up are quietly similar of the one discussed on Chapter 2 (Figure 4.2). The modifications are the position of the inlets that they are at level of the copper plate and the material of construction is different but it does not matter for our purposes. First, the flask with ultra-pure water gets into a heat bath until its temperature reaches $13\text{ }^{\circ}\text{C}$. At the same time, the work area of the condensation chamber is set to cool to $-13\text{ }^{\circ}\text{C}$. The $4\text{ }^{\circ}\text{C}$ is the difference of temperatures found between the substrate sample and the work area of the copper plate. So, the substrate achieves $-9\text{ }^{\circ}\text{C}$. Once all these conditions have been reached, the water vapor is flowed to begin the observations (Figure 4.3 (1)).

4.3. Observations

The experiments were performed using different samples, with micro etching like stripes 4.4 and squares patterns, over parafilm, silane coated glasses, and 3M EGC-1700 coated glasses too. Figure 4.5 shows the stages observed during condensation of WV over a cover slip glass coated

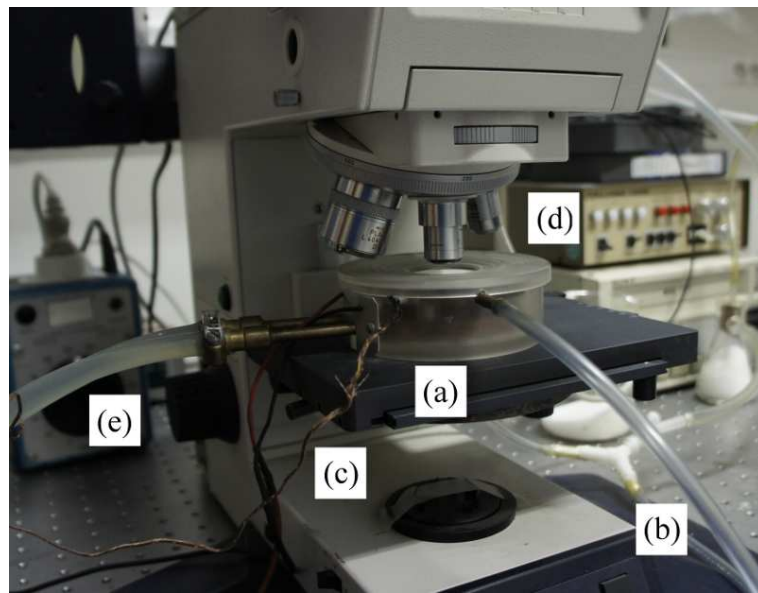


Figure 4.2: (a) Condensation chamber. (b) Tubes to flow cooled water vapor. (c) Four thermo-couples to acquire the temperature of the copper plate, the sample, in one of the inlets of vapor, the temperature outside the system. (d) Microscope. (e) Tubes to recirculate cooled water.

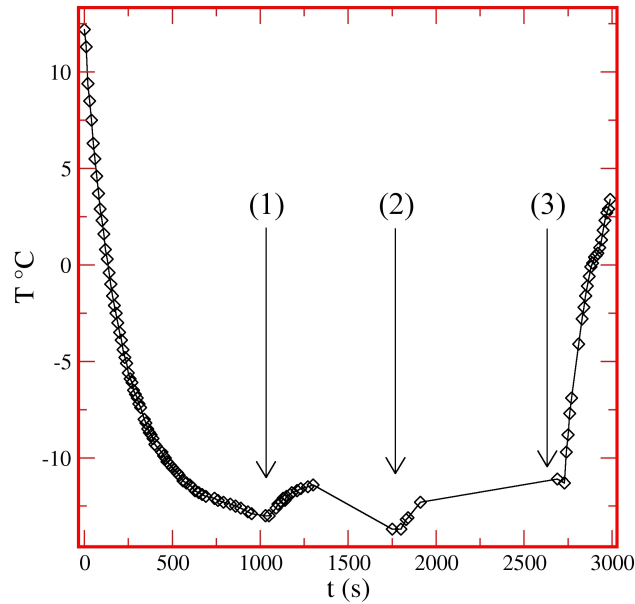


Figure 4.3: The variation of the operation temperature measured on the copper plate of the condensation chamber. (1) The copper plate reached the minimum temperature, and the experiment can be performed. (2) The flux is stopped to do inspections. (3) The system is reheated.

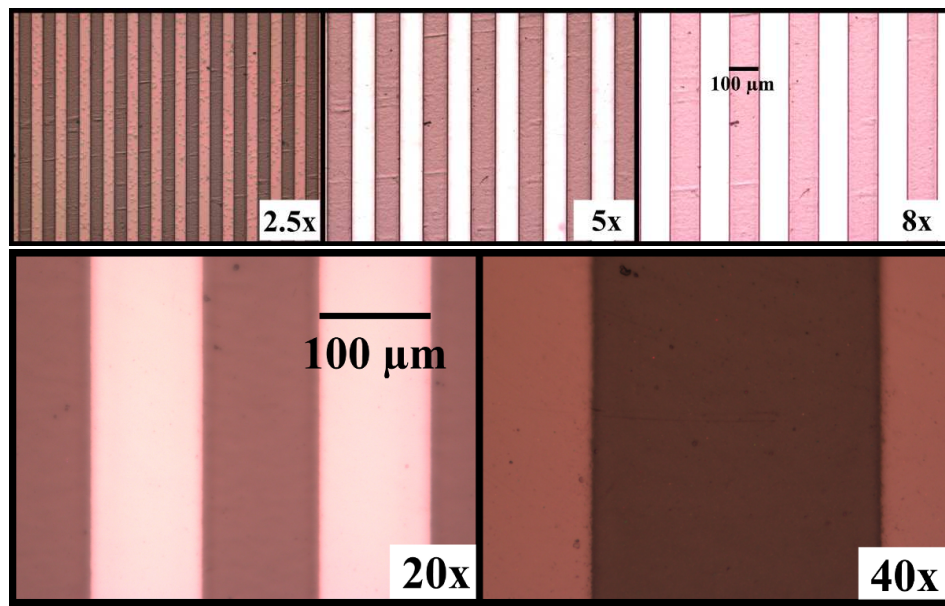


Figure 4.4: Stripes width of $100 \mu\text{m}$ and depth $45 \mu\text{m}$ observed at different magnifications.

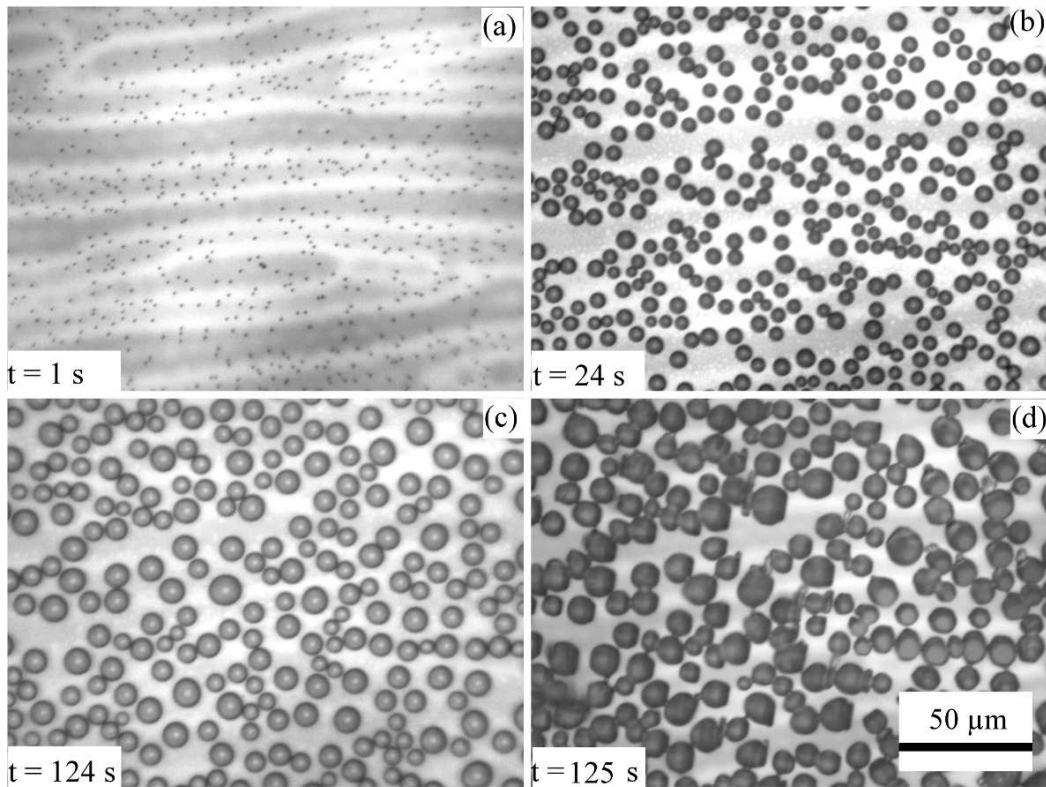


Figure 4.5: Freezing formation: observation of the previous stages of BF. (a) The BF starts under conditions of -9°C . (b) Droplets grow as $\langle r \rangle \sim t^{1/3}$ (Figure 4.7a). (c) The $\langle r \rangle \approx 9 \mu\text{m}$ without appreciable coalescence events. (d) In the lower-left corner is appreciable how some drops start to freeze.

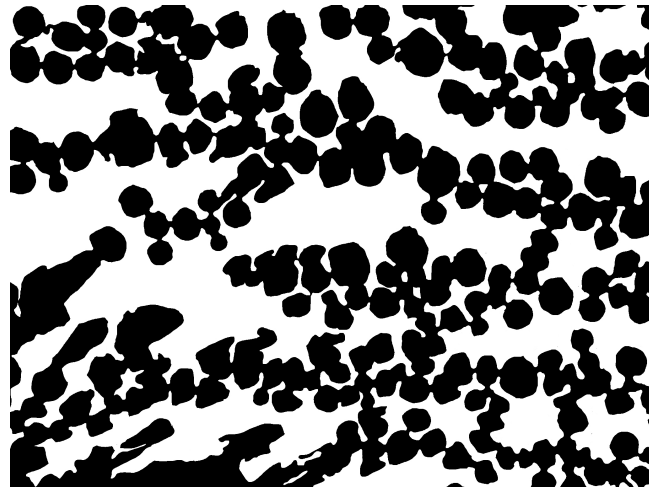


Figure 4.6: The final stage of propagation of ice is thresholded in order to compute the fractal dimension which has a value of $f_D = 2.48$ (Figure 4.5d).

silane with contact angle of $\theta \approx 90^\circ$. Even though, the glass cover slip coated with 3M EGC 1700 presents stripes and the BF appeared not to notice them³.

We observed the next (Figure 4.5): (a) At the beginning very small droplets appear spread over the substrate. (b) The droplets grow in the second regime of BF. During the growth, the temperature is $T \approx -10^\circ\text{C}$. (c) The drops still are liquid. They grow to a size of $\langle r \rangle \approx 9 \mu\text{m}$ and the bare spaces are significantly reduced, and very few coalescence is observed. (d) Suddenly, the system transits from supercooled to solid phase. It occurs when one iced drop (or a group of drops, we do not know) touches another drop. The transmission of the solid phase through the pattern happens because the ice is hygroscopic and grows by the adsorption of vapor from the liquid drops. Also, the solidification occurs at the same time in other places of the substrate. We noticed this when we moved the microscope to observe other areas of the sample. We found very large dendrite crystals nearby the inlets of vapor.

In the same experiment we observed too, not only propagation of ice. We could observe parts of the substrate where evaporation and ice growing were in progress. There were too, parts of the substrate with large dendrites and ice crystals, as well, parts where several drops remained liquid. To distinguish whether a droplets remains or not liquid, first we observe their shape. Then, we change the lens focus distance to illuminate a single drop. If the drop reflects the light as in cases mentioned on Chapters 2 and 3, we say it is still liquid.

To begin with a characterization of the system, we calculated the fractal dimension of the system at $t = 125$ s (Figure 4.5d) which corresponds $f_d = 2.48$ (Figure 4.6).

Other interesting observation is the BF evolution which is driven as the theory predicts. The influence of the supercooled metaphase seems being ignored by the process. Since the initial time until the frost formation, a power law of $t^{1/3}$ describes well the increment of mean radius (Figure 4.7).

When all the droplets (on the observable area) have been converted into ice, it is time to

³Those stripes are the result of coating, they seem to be related to the repellent property of this coating. The stripes are not so regular or periodic

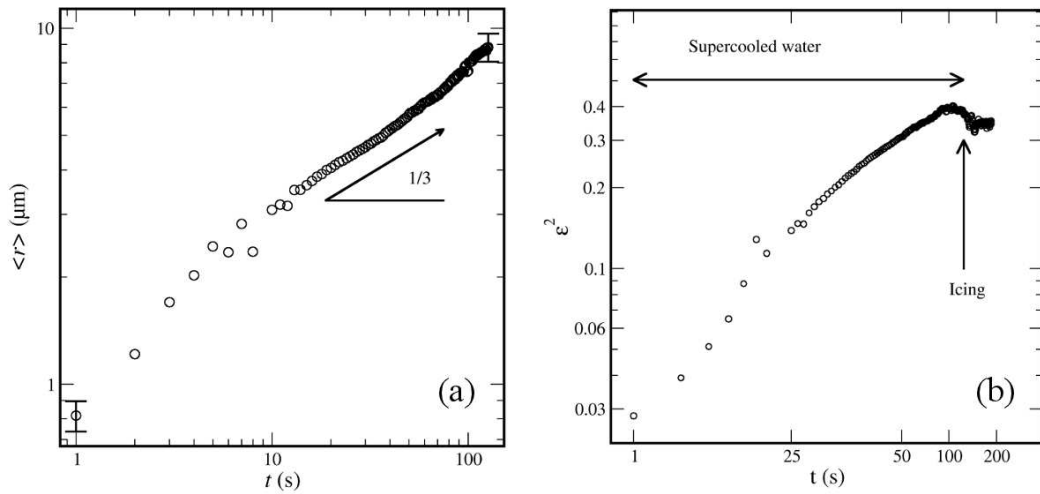


Figure 4.7: (a) The mean radius for second stage of BF is well described by the power law of $t^{1/3}$. After this, the ice propagates by touching the drops. (b) The occupation before the ice propagation on the surface is $\epsilon \approx 0.4$.

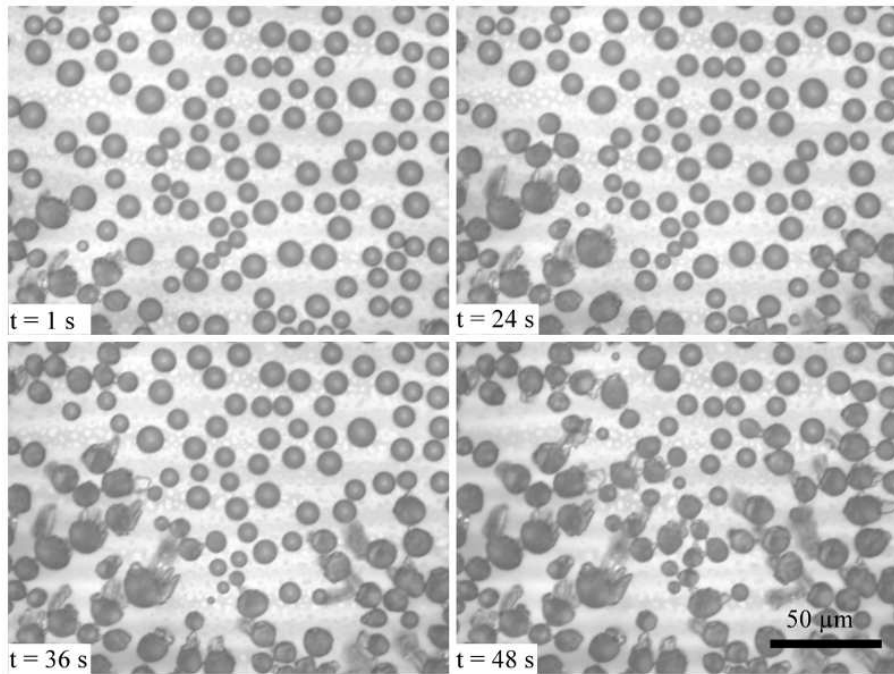


Figure 4.8: In the same observation of Figure 4.5 but, shifting the time to 1 s in order to follow the ice propagation in this specific area. It can be appreciated contagion of ice in the drops which produces dendritic shapes.

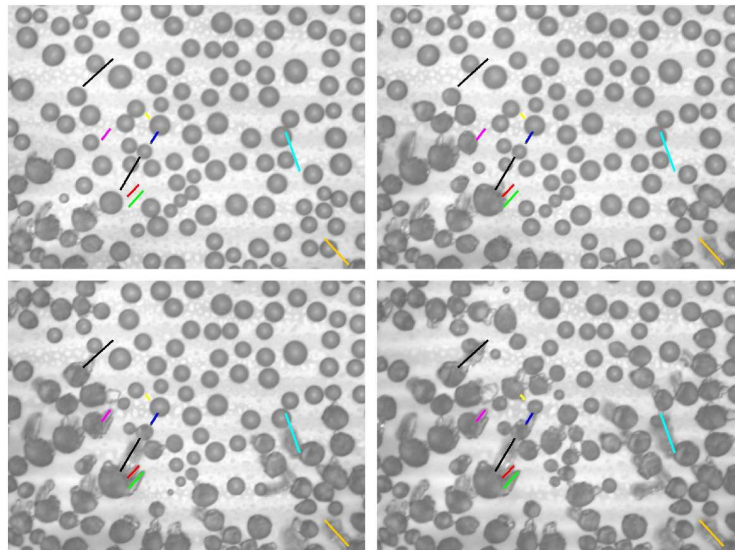


Figure 4.9: This set of images corresponds to Figure 4.8. The paths of the growing orientation are drawn signalizing the dendrites' growth orientation.

browse with the microscope to other area to look for of another front propagation. Figure 4.8 shows where the dendrite formation is developing at expenses of the liquid droplets. In this case, we could observe the evaporation of few droplets since the time $t = 1$ s. Some dendrites grow from the upper left part of the observable area. Time after, it exists a clear tendency of the advancing ice. The drops on the upper part of the observation area are source of water. Then, the dendrite ice is naturally oriented towards that direction. In Figure 4.9 we draw the paths of the growing dendrites in order to know the rate of growth and propagation. To understand better the situation, we followed a case where there are two droplets in front of a iced one: one drop is closer to the iced one and it is large enough to do not totally evaporate during the deposition process. The other droplet is small and it is far from the iced one. We observe how the first droplet evaporates but a dendrite from the iced drop can contagious the liquid droplet. Simultaneously, branch of ice grows from the iced droplet but it could not reach the droplet before it evaporates completely (Figure 4.10). The plots where the evaporation and growing of droplets suggest that the velocity of propagation is constant. The evaporation process leads us to think on the difference of pressures on the surroundings between the ice and the liquid droplet. The corresponding partial pressures (at the vicinity) are: for an evaporative droplet P_d and for the ice P_i . And the relation between these two partial pressures is $P_d > P_i$. This inequality is maintained always and it is the core of the phenomenon of ice propagation. In Chapter 3, we suggested how could it be the pressure gradient on the inter space between two objects which maintain different pressures. In fact, the among of pressure, should depend on the size of the objects. This assumption is in agree with the two examples of above. The low partial pressure produced by the ice is due to its hygroscopic property. On physiochemical the salty drop and the ice share similar characteristics but, the geometry achieved for one humidity sink and the other are completely different. The salty drop maintains a radial geometry while the ice changes its shape from the radial one to faceted.

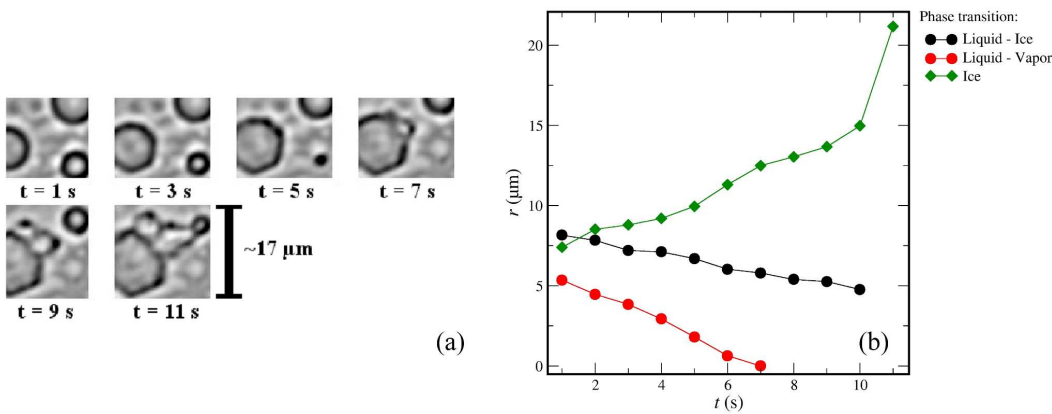


Figure 4.10: (a) The two cases of transmission phenomenon: in one case the droplets is enough large and enough closer to the one solidified and a dendrite can grow towards this droplet. In the other case, the drop is small and is enough far such is evaporated. (b) The rates of evaporation and the advancing ice.

The values of the velocity of propagation have been computed for Figure 4.9. It reveals that the transmission from drop to drop increases on time (Figure 4.11). The range of values of the velocity reported is $V \approx 0.5$ to $1.6 \pm 0.2 \mu\text{m}\cdot\text{s}^{-1}$. In other places of the substrate it was found a situation where a front of droplets are facing a large ice crystal. The crystal grows at expenses of water source (Figure 4.12). The evaporation profile is depicted as almost near to a quadratic function (Figure 4.13). Also, we have observed different crystal formations that are typical from the range of the operation temperatures (Figure 4.14).

In other experiments, we used patterned surfaces but, without obtaining the same family of crystals and the explicit stages of the process of freezing. Anyway, I present too those observations as a collection of the experiments (Figure 4.15).

4.4. A Salty Drop under Solidification Temperature of Water: Anisotropy on the Pressure Gradient.

Because is interesting and because is affordable to do the comparison of the boundary conditions for pressure at the perimeter of the salty drop and at the beginning of the BF can give us a clue about the process of water vapor adsorption. We can extract information of the supersaturation pressure at the exactly time when all the BF pattern become ice due to the same ideas exposed on Chapter 3. The experiment procedure is similar to the other exposed, without differences so, we can avoid an explanatory section. At the beginning a small NaCl crystal is set over a silane coated glass. The system temperature is decreased until $\approx -9^\circ\text{C}$. The contact angle detected for the salty drop is $\sim 92^\circ$. The evolution of the salty drop radius and the depletion zone is depicted in Figure 4.16. In this case, due to the anisotropy produced by the growth of the ice around the salty drop, the dynamic of the radius of the salty drop R and the width of the depletion zone δ are affected. Due to the low temperature among the salt crystal, it is not completely dissolve during the fast production of drop-wise condensation. The explanation of

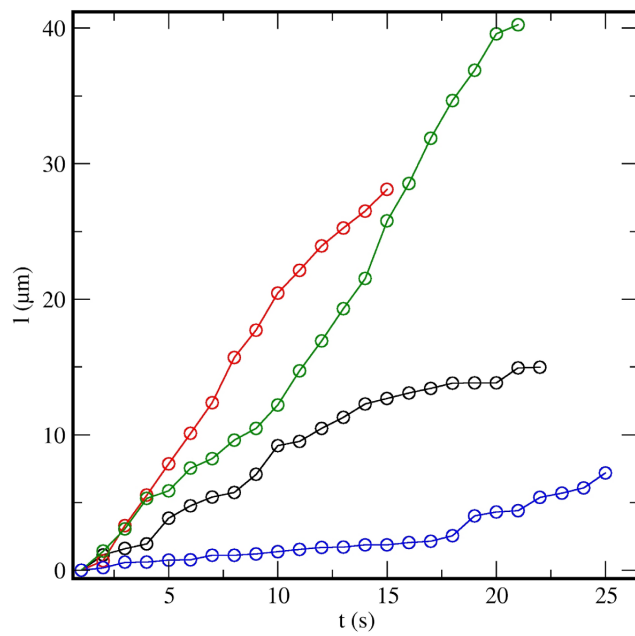


Figure 4.11: Velocity of propagation of ice measured from already iced droplets to liquid ones. The measurements were taken from Figure 4.9. The range of values of the velocity reported is $V \approx 0.5$ to $1.6 \pm 0.2 \mu\text{m}\cdot\text{s}^{-1}$.

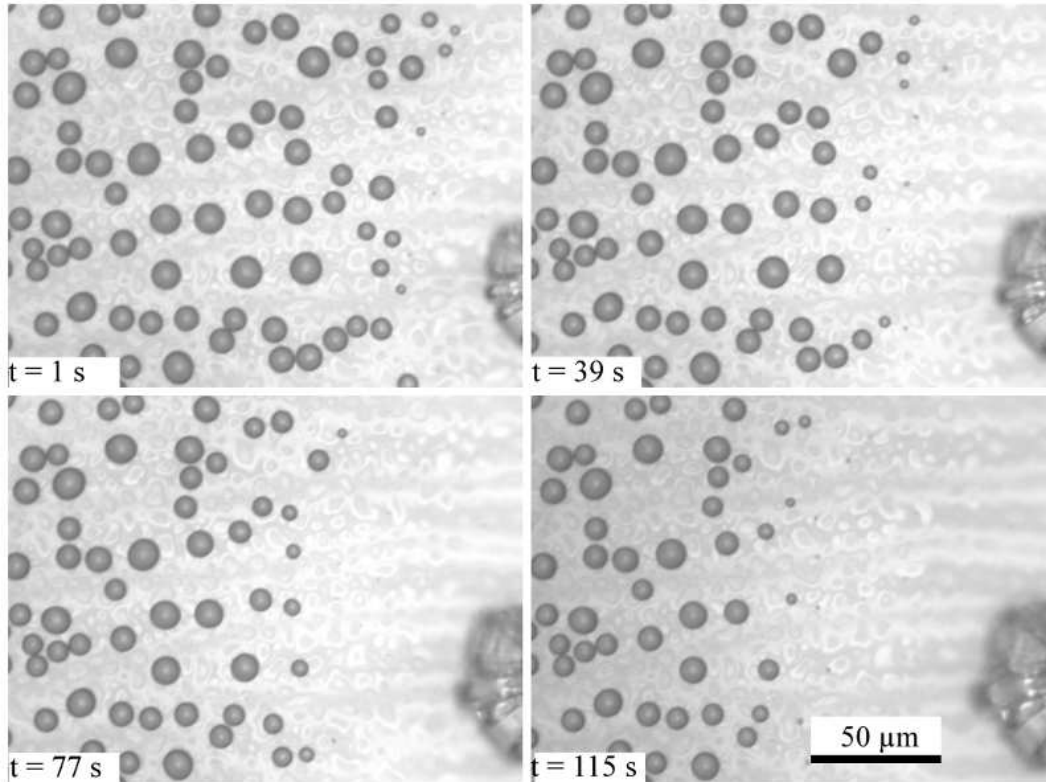


Figure 4.12: Evaporation of the facing droplets due to the dendrite.

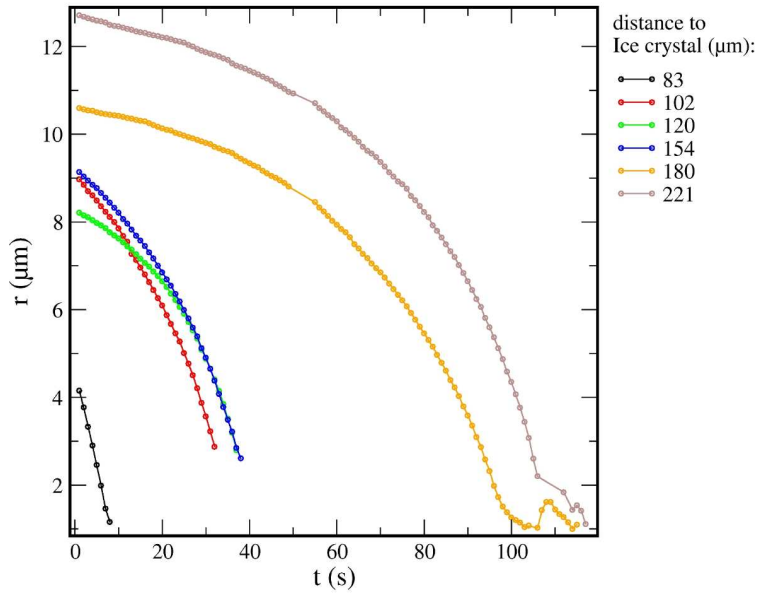


Figure 4.13: Evaporation of the droplets at different distances from the ice crystal (Figure 4.12).

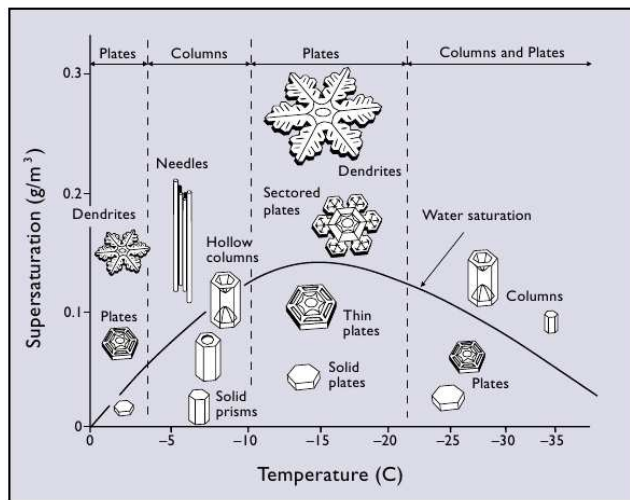


Figure 4.14: The Morphogenesis on Ice of Kenneth G. Libbrecht [53]. The experiment temperature is -12 to -6 $^{\circ}\text{C}$. We could observe some of those crystals represented on the sketch, even flakes, needles and dendrites (to see more crystals, Figure 4.26 at the end of the chapter).

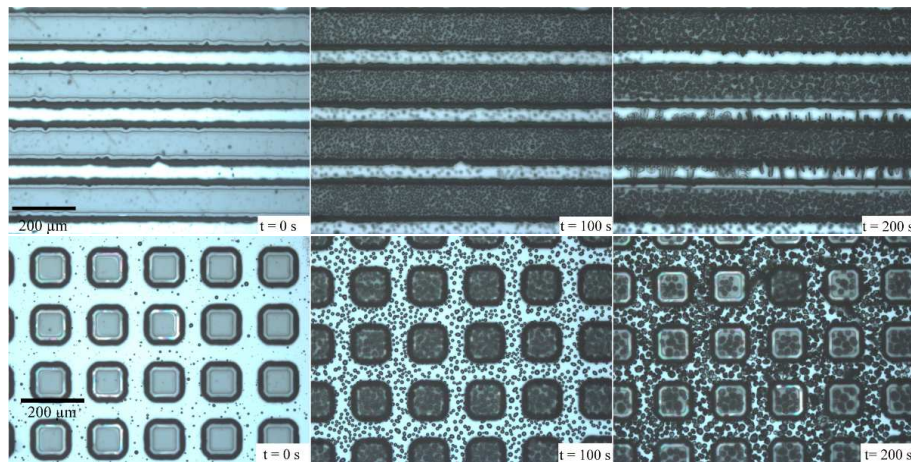


Figure 4.15: The icing experiment is reproduced on patterned surfaces. The interest as an application technique can increase if the pattern instead to be a micro structured is an nano structured surface. The depth of patterns is 45 μm . In the pictures it is not appreciable some significant change on the process of propagation. The only detail different from the flat substrates is that it is possible to observe 3D crystals.

these results is a very heavy duty task to solve. It should be necessary to discuss the relations of the Chapter 3 taking into account the complexity of the flux produces by anisotropy of the BF pattern and its phase transitions.

The salty drop grows fast, because the humidity is partially collected by the crystal. Once the chamber is full of vapor, the BF appears leaving a small gap between its two boundaries. For short times, this gap appears to be constant and the only length which is changing is the radius of the salty drop. When the BF freezes, the depletion zone shrinks because the ice is attracted to the humidity source: the salty drop. When the salty drop is touched by some crystal, it does not get freeze like the case of the ultra pure water. Instead, the solution spreads on the ice melting it. In Figure 4.21 it is appreciable the concentric relation between the salty drop and its depleted zone is missing. This anisotropy can be understand in terms of the size of the crystals on the limit of the depletion zone. If the dendrites in some specific place are bigger than in other places, the system will break the circular geometry in such point. The Figure 4.20a shows two values of δ and R almost symmetric one respect to the other. Perhaps, because the asymmetries between the depletion zone and the quasi-spherical shape of the salty drop are not quite different. The fit proposed in Chapter 3 (Equation 3.7) as it is noticeable on Figure 4.20b, it cannot be applied. We can say the pressure of supersaturated vapor on the frontier it is not so high in comparison with the partial pressure on the salty drop. This can explain the small rate of growth of the salty drop. If we look on the BF pattern, before the ice formation, the growth of law $t^{1/3}$ fits well with the mean radius (Figure 4.22). The concentration of the salt solution is affected by the temperature. The crystal salt does not dilute totally inside the salty drop and this could be a strong reason to observe anisotropy, which impedes a uniform growth of the salty drop. Something unexpected was to see how the salty drop continues growing even when the frost pattern was already formed all around. In fact, should be necessary to reconsider the mechanism of adsorption. The main

hypothesis is that the molecules of water enter only by the contact line, but what is going on if this mechanism was only a part, and the molecules increase the size of the droplet entering by its surface, too?, perhaps the answer is in the experiment where ice and liquid droplets are surrounding the sink (Figure 4.18).

4.5. A Model of Ice Propagation

As I mentioned at the introduction, the propagation of ice due to a percolation mechanism was not observed before this work. In this section I am going to use a part of the theory of the article "Percolation-induced frost formation" by J. Guadarrama-Cetina, A. Mongruel, W. González-Viñas and D. Beysens [2].

Before the freeze propagation starts, the occupation maximum reached by the pattern is $\epsilon^2 \approx 0.4$; that means the contact angle is $\theta \approx 200(1 - \epsilon^2)$, hence $\theta \approx 120^\circ$ and the mean distance is $0.8\langle r \rangle$. The freezing only happens on during the second stage and the possible explanation can be related with the mean size of droplets and because the phase of supercooled liquid needs very small perturbations to transit from liquid to solid. Commonly, it is observed that the process begins at some arbitrary place near to the edges of the sample. When some droplet has been touched by the ice, the contagious is instantaneous. Two sequences of the ice transmission are shown in Figures 4.23 to 4.25 (also in Figure 4.10 to 4.9). A dendrite grows towards the next drop, but if the drop is small and it is placed far, then that drop will evaporate. Otherwise, if the drop is large and it is placed not so far, the ice will transmit by this liquid drop to continue growing. The ice growth proceeds by vapor deposition and the liquid drops feed the ice crystals (Figure 4.12). The process of deposition is driven by the difference of vapor saturated pressure, of course this pressure on solid is very low rather than liquids, and the maximum difference of pressure is observed at -12°C at atmospheric pressure (approx. 10%).

4.5.1. Percolation

The velocities of transmission (Figure 4.11) are linked with rates of evaporation (Figure 4.12). In this [2], the diffusion flux diverges at the contact line, so the evaporation rate is proportional to the perimeter of droplet,

$$\frac{dm}{dt} \approx R, \quad (4.1)$$

or

$$\frac{dR^3}{dt} \approx R. \quad (4.2)$$

m and R are the mass and the radius of the drop. The rate of evaporation can be observed as the rate of change of the surface area of the drop,

$$R^2(t) = R_0^2 - \alpha t \quad (4.3)$$

where $\alpha \approx 1.8 - 6.25 \mu\text{m}^2\cdot\text{s}^{-1}$. If two identical droplets of radius R_0 separated by a distance d_0 between their interfaces are considered, and $t = 0$ is the time when the drop freezes and emits a dendrite. The time t_D is defined when a drop is totally evaporated which corresponds to,

$$t_D = R_0^2/\alpha \quad (4.4)$$

The dendrite makes contact with the center of the evaporating drop at,

$$t_l = (d_0 + R_0)/V \quad (4.5)$$

and the condition to have a contact is $t_l < t_D$. The possible minimum radius for drops to have transmission of ice can be obtained from the inequality,

$$R_0 > \left(\frac{d_0 + R_0}{R_0} \right) \frac{\alpha}{V} \quad (4.6)$$

4.6. Summary and Concluding Remarks

Experimentally, it was possible to observe a new phenomenon of ice propagation in 2-D. In order to understand and to classify the physical variables of the propagation of ice induced by BF, measurements of fractal dimension of the iced pattern were done, also the dynamical measurements of the mean radius of supercooled water droplets and their occupation factor was useful to determine a model of propagation and the description of the minimum necessary condition to transmit ice for one frozen drop to a nearby liquid drop. Also, we studied the evaporation of water drops when they are facing ice crystals and we measured the rate of evaporation. As a contribution of the model of propagation, the velocities and the direction of the dendrite's growth were measured satisfactory. In other experiments developed in the same conditions, we studied also the anisotropy of water vapor condensation and the adsorption by a humidity sink. We also found the impact on the adsorption process when the BF pattern is homogeneous or not.

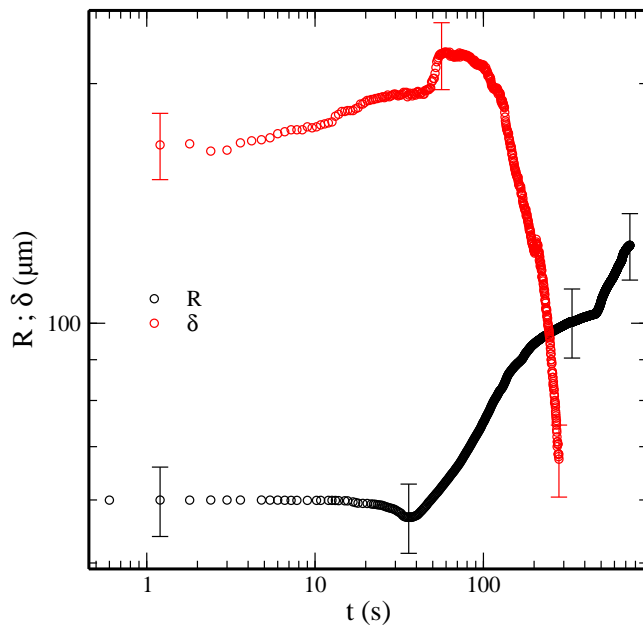


Figure 4.16: Depletion zone δ and radius of salty drop R at $T = -9^\circ\text{C}$. At the beginning the small crystal captures all the water vapor on its surroundings getting wet and dissolving. After some time, a small air bubble is suspended inside the salty drop. The time when the salty drop reaches the stage of saturated solution is not very clear, but it seems exists at least three stages of growth. Once the ice pattern has appeared, the droplet is still growing, even with the competency of ice. The increase is small because the ice is also hygroscopic. In this case, due to the anisotropy on the water vapor distribution a reference of salt saturated solution at certain temperature stood undefined. The fit (Equation 3.7) cannot be applied to describe the evolution. Other interesting observation is the crossing of δ and R .

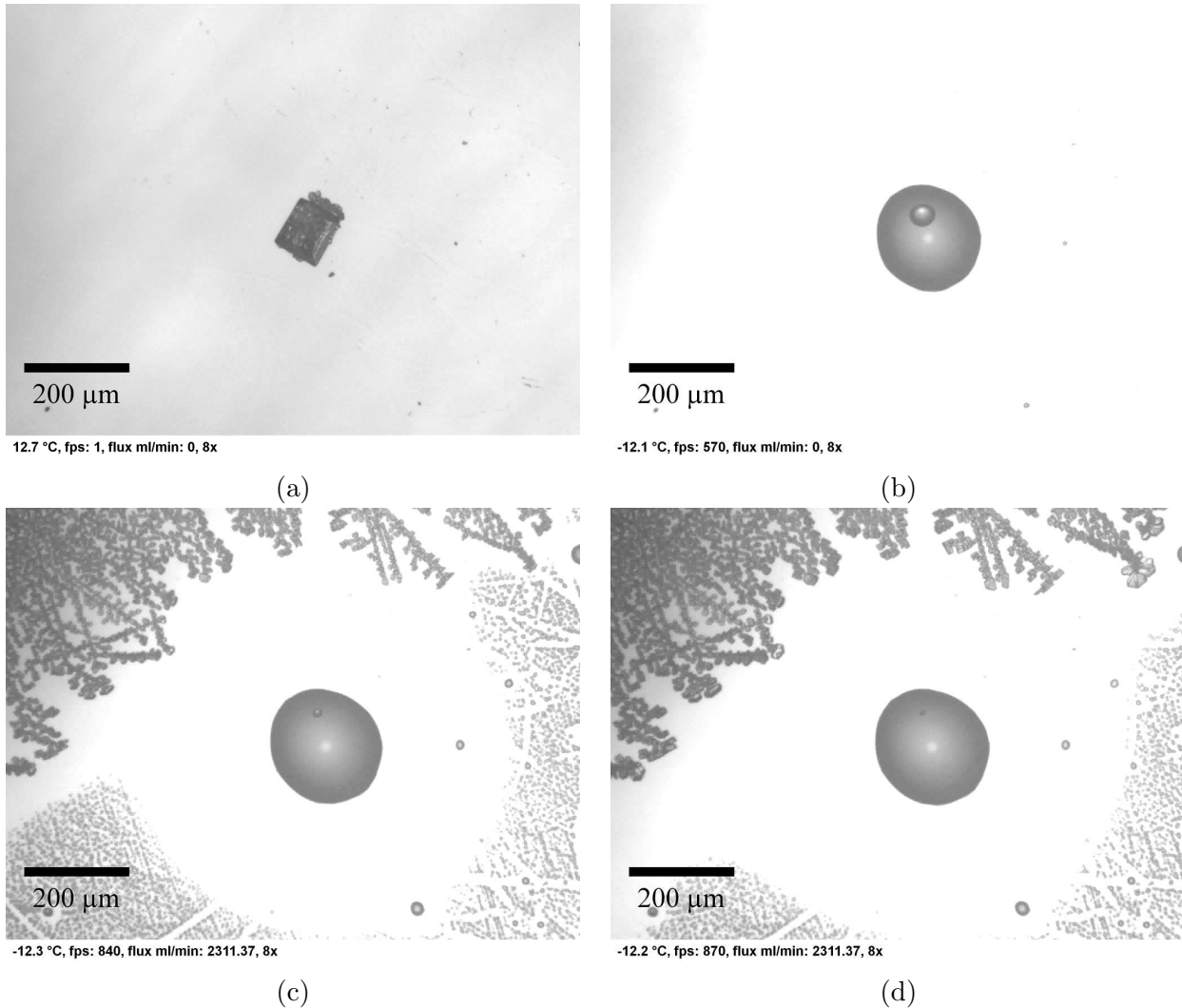


Figure 4.17: (a) A NaCl crystal is set over a cool silane coated glass. (b) When the temperature is approximately -4°C the rest of humidity inside the chamber condenses on the crystal. (c) Once the temperature is -12°C , the water vapor flux produces condensation all around. Very fast the propagation of ice occupies a big place and starts to compete for water vapor. (d) At this time, the salt has not diluted yet, but the growth of the salty drop has not stopped, even the ice is in competition for the humidity.

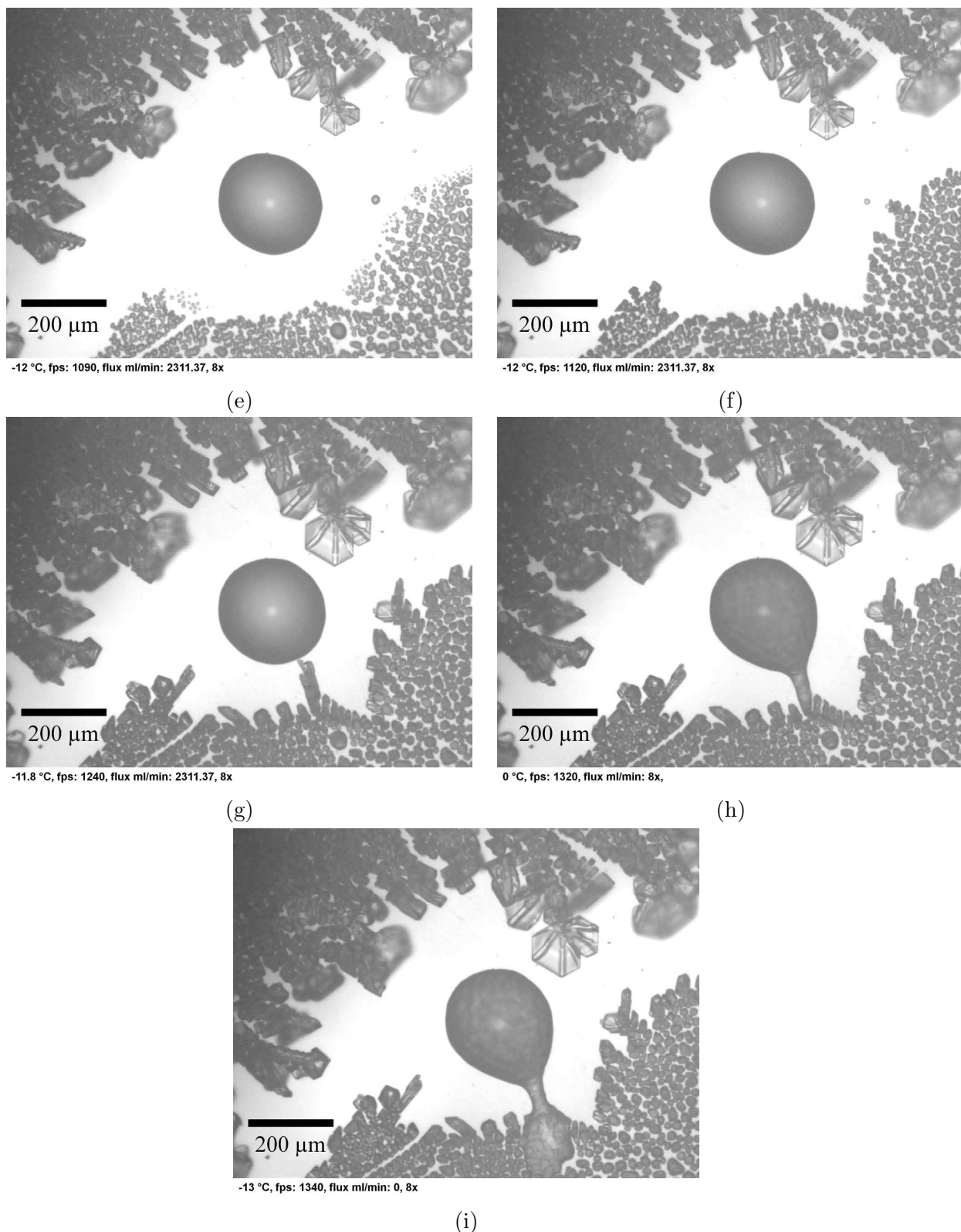


Figure 4.18: From Figure 4.17. (e) The NaCl crystal has diluted completely. (f) For the ice it seems that the most affordable humidity source is the salty drop. (g) The small crystals use as humidity source the salty drop. (i) When finally a crystal has touched the salty drop, this did not dilute, but spreaded and melted the ice.

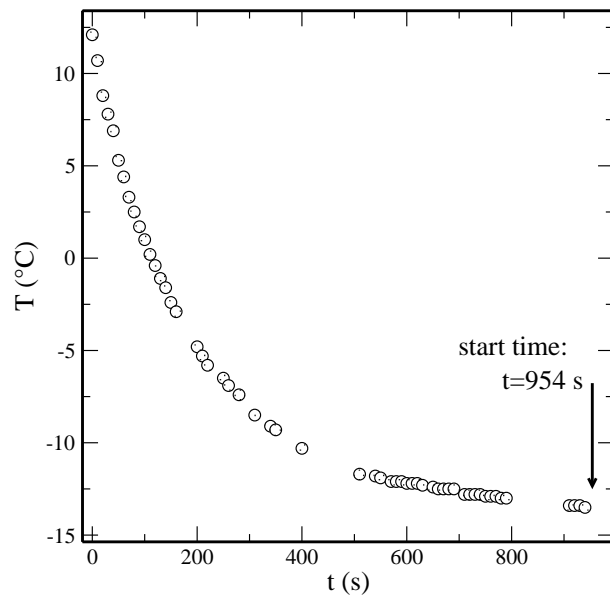


Figure 4.19: The arrow marks the starting temperature of the flux input. At this time, the reference time t^* is defined as 0. The temperature was monitoring from the copper plate, but it corresponds for 4 °C of difference.

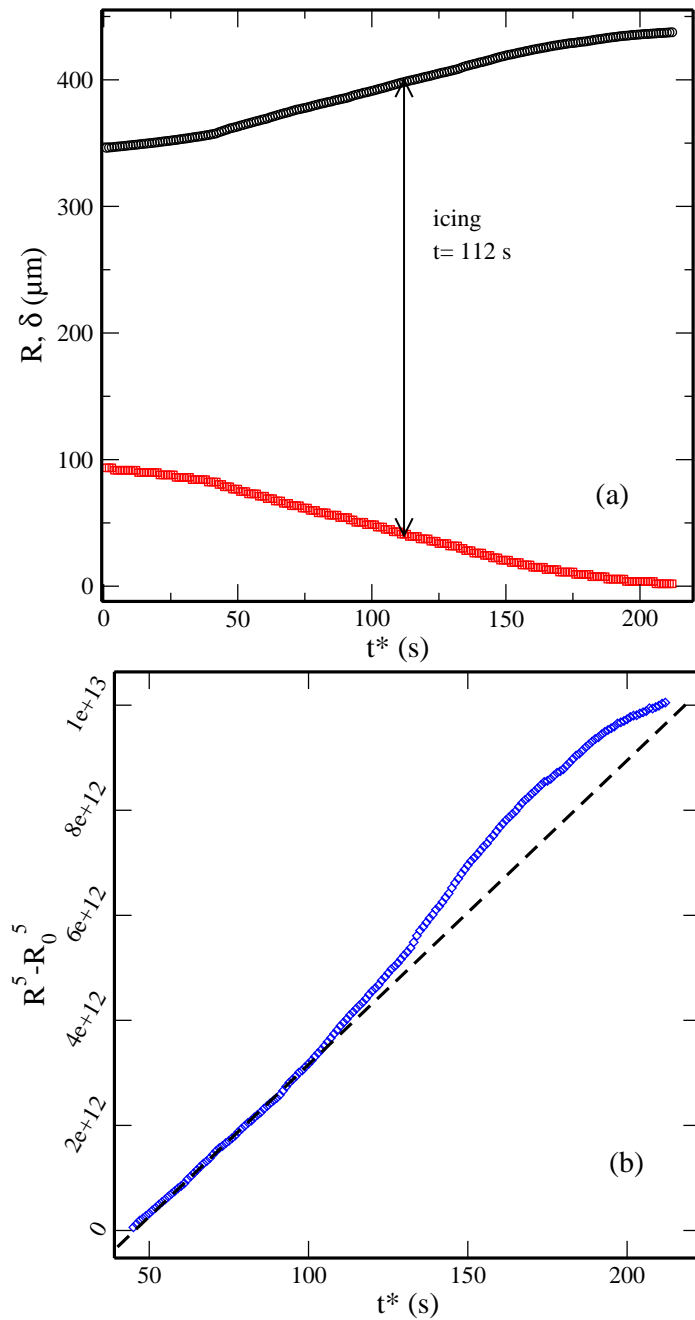


Figure 4.20: (a) The mirror effect of the value of δ (depletion zone width in red squares) and R (radius of salty drop in black circles) is due to the depletion zone which stays defined in the same perimeter, while the salty drop grows until the BF freezes. (b) The value for the concentration on Raoult's Laws (Equation 3.2) is $B = 2.53 \cdot 10^9 \pm 0.18 \cdot 10^9$ ($\text{m}\mu^5 \cdot \text{s}^{-1}$).

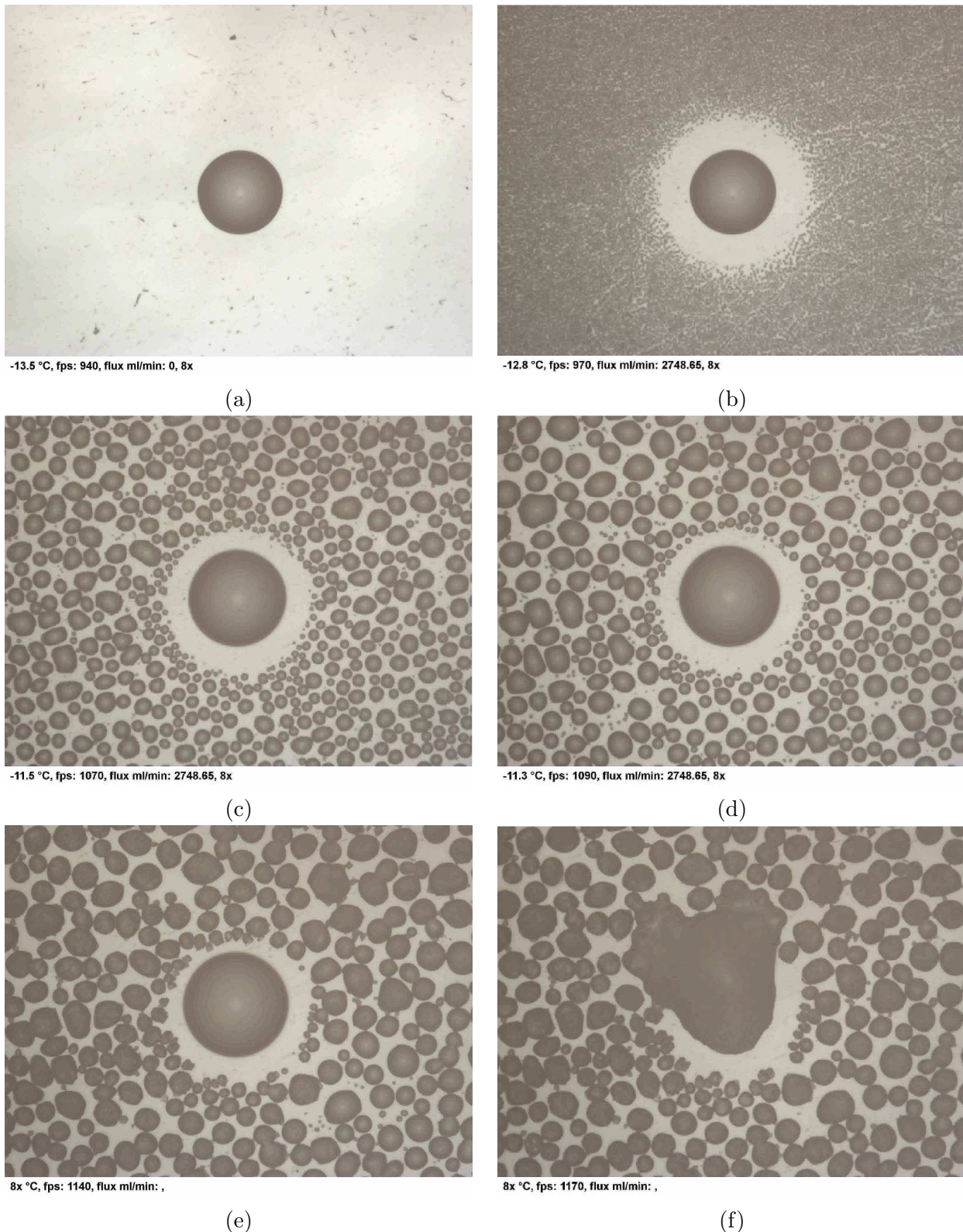


Figure 4.21: The temperature on the substrate is around $-8.5\text{ }^{\circ}\text{C}$. (a)-(b) In a short time the salty drop is surrounded by the BF leaving a short gap of depleted zone. (c)-(d) Apparently the depletion zone does not shrink too much in comparison with the salty drop producing an anisotropy. (e)-(f) The salty drop's center is shifted from its original position and finally the ice makes contact with the salt solution.

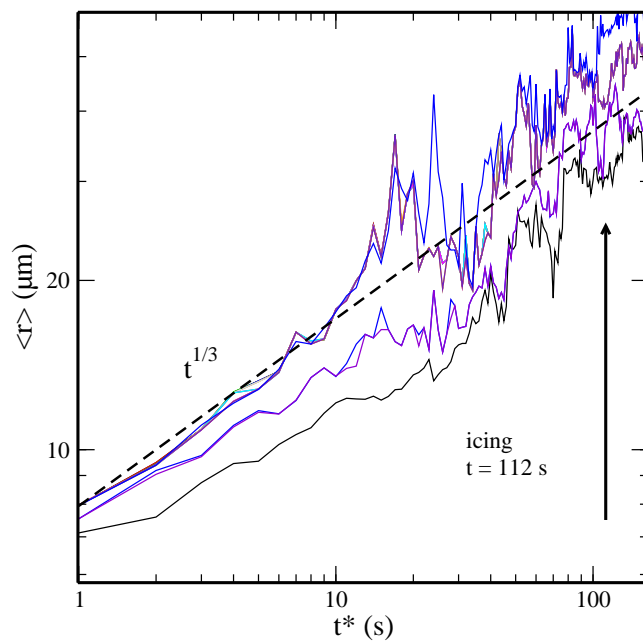


Figure 4.22: The BF around the depletion zone cannot achieve the stage of coalescence (that means $\langle r \rangle \sim t$ is not represented on the graph) few time before, the ice is spread all around. As in the Chapter 3 and [1], the different continuous lines are the values of mean radius far from the salty drop.

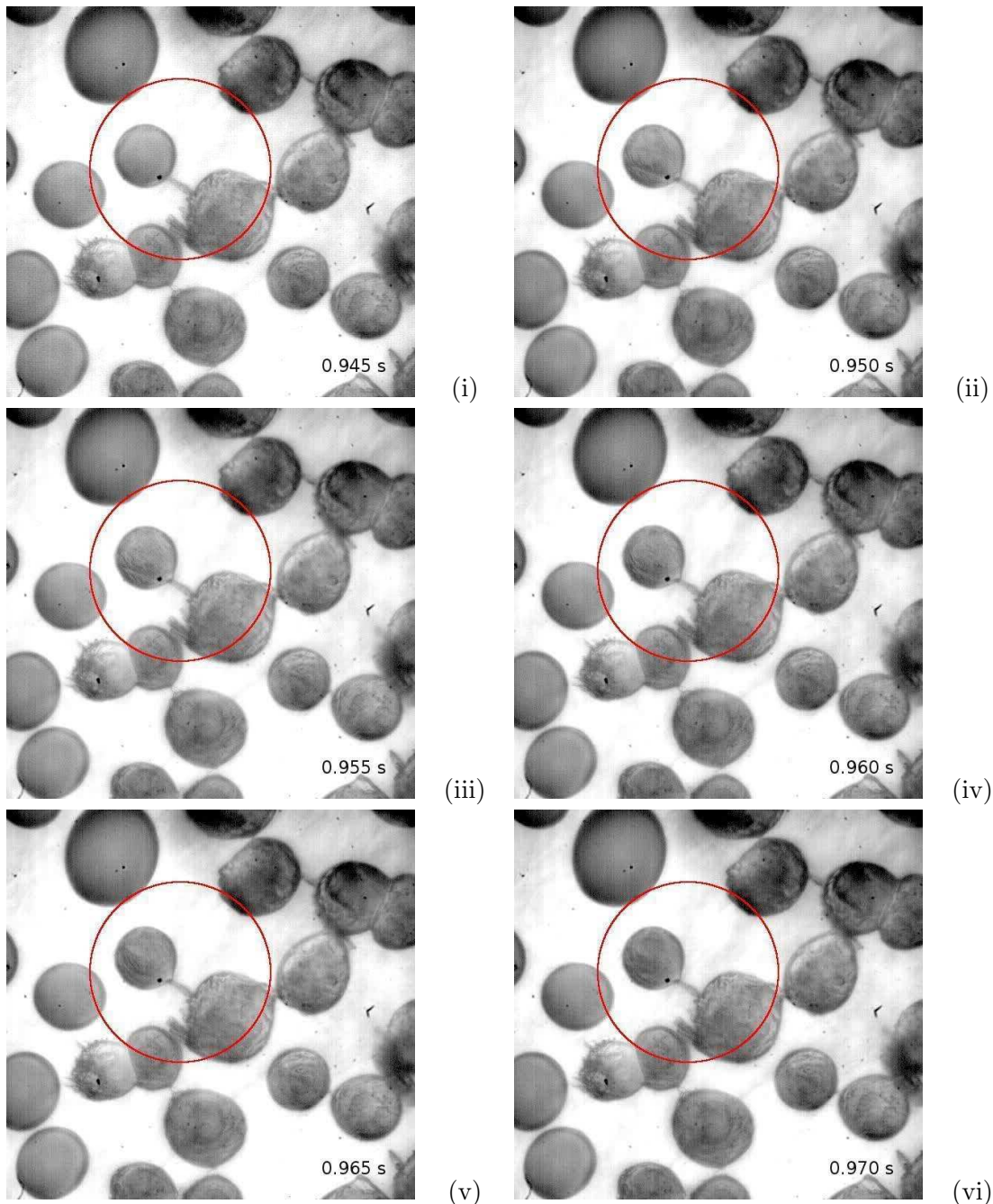


Figure 4.23: The transmission of ice is recorded with a fast speed camera (1000 fps) with an objective of 10X. (i) shows a very thin dendrite growing towards a non-iced droplet. When the dendrite touches the drop, the icing process begins from the dendrite's tip to a small area on the droplet's surface. The ice spreads inside the droplet.

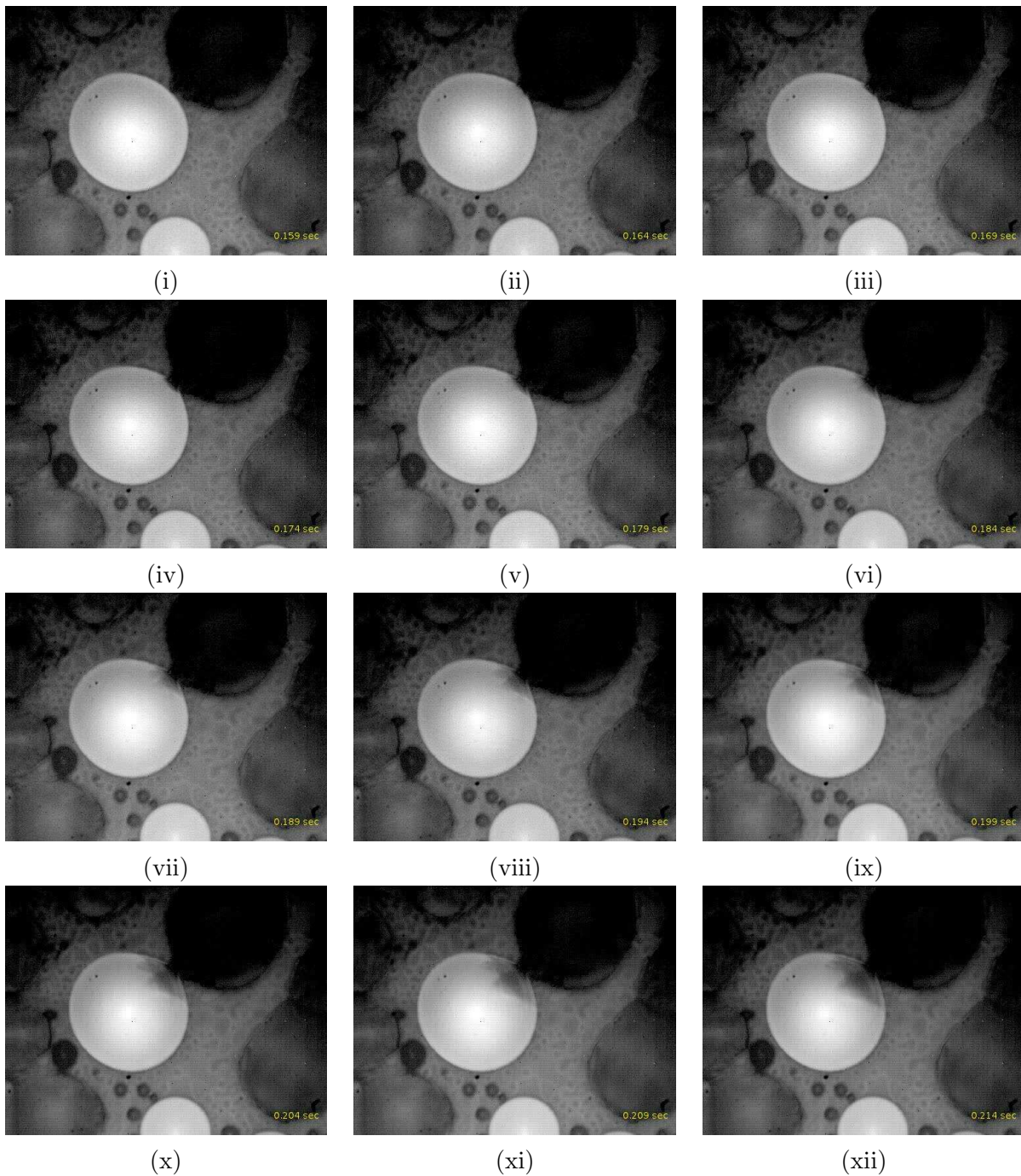


Figure 4.24: Another observation series shows in detail the transmission of ice. At the beginning a dendrite's tip touches the surface of a droplet. The ice is spread for all the inside volume. With help of a fast speed camera (1000 fps) with an objective of 20X it is possible to follow the propagation of ice.

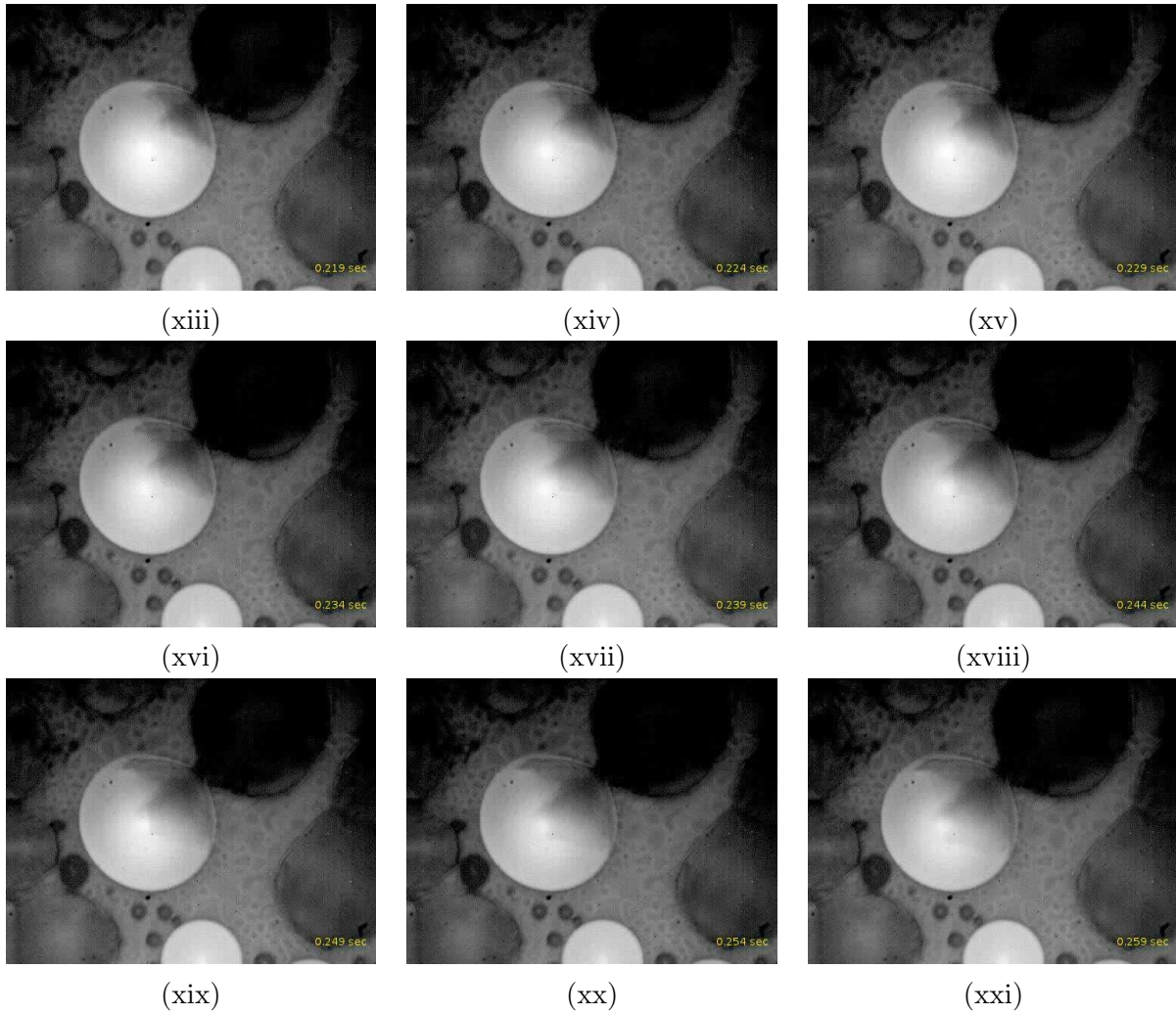


Figure 4.25: From Figure 4.24 In appearance the ice inside the droplet changes the shape of the geometrical boundaries of the droplet during the phase transition.

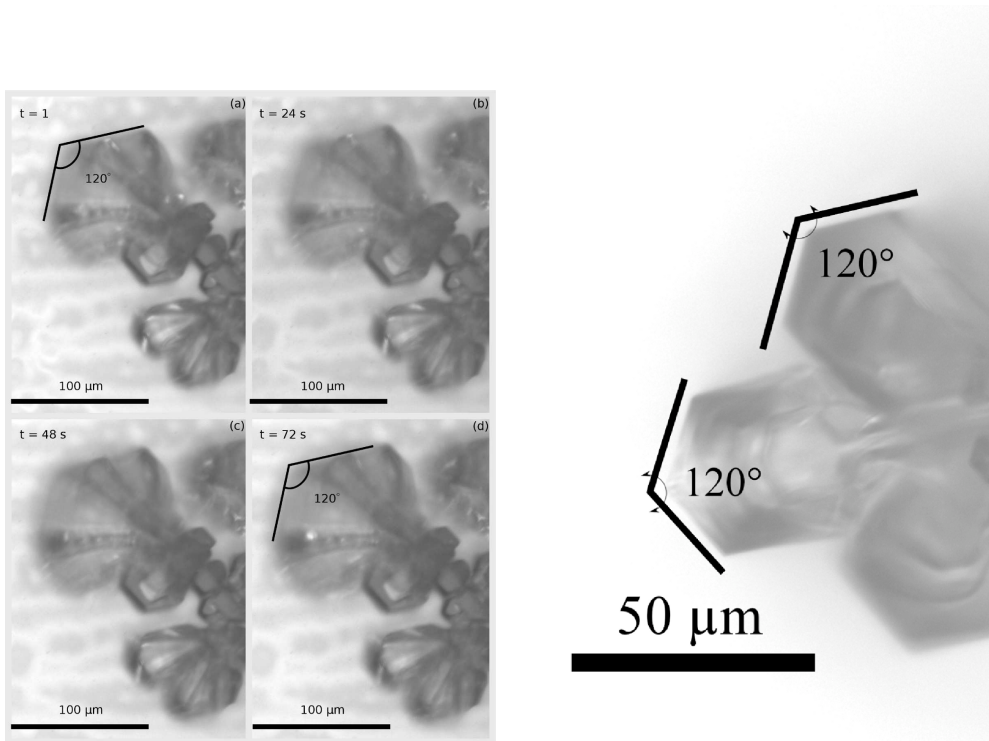


Figure 4.26: According to the operation temperatures, flakes and hexagon shaped crystal were observed during the experiments.

Chapter 5

Two Immiscible Substances Condensing on a Cold Surface

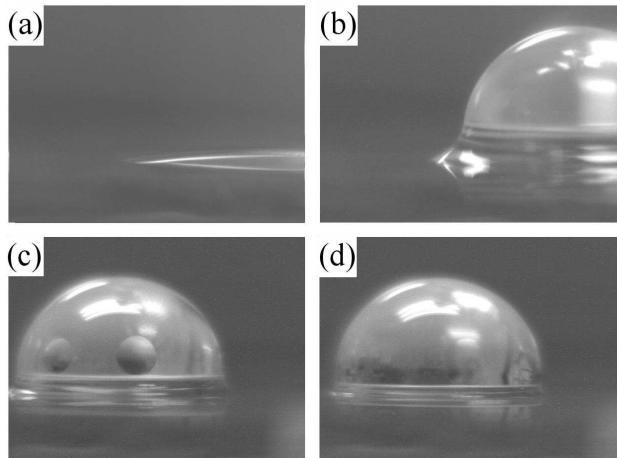


Figure 5.1: (a) The contact angle of a HMDSO droplet over common glass is very low. (b) A water drop is set over, then the contact for both substances increases. (c) Due to the surface energy difference between the two substances, the HMDSO enters to the water drop. (d) The HMDSO out of the contact line of water evaporates and the rest enters to the water drop and the contact angle of water of both substances increases.

5.1. Introduction

We found very interesting the interaction two immiscible substances condensing in the same surface simultaneously. According to the physical properties of each substance, one may think, ultra pure water can condense first and occupy more coverage area. The hexamethyldisiloxane ($C_6H_{18}OSi_2$ or HMDSO) condenses after water, its dynamic of pattern condensation is different at time it interacts ultra pure water. When we observe the experiments, the competition is clear defined. Water always condenses first. HMDSO takes some time to do it, and when it finally

does, it reaches the coalescence stage in a short time and it forms clusters with ultra pure water droplets or **H-W**. We are interested on those clusters and how the dynamics of BF is affected for the interaction of HMDSO. Also, we are going to focus on the necessary conditions to obtain those clusters. The properties of both substances can be consulted on Chapter 2. We decided to use those substances because the ultra pure water is the most used substance in laboratories, and in the case of HMDSO it is immiscible and highly volatile, and it does not make chemical reaction with water. Other interesting applications of both substances can be found in J. Guadarrama and W. González-Viñas [3, 54–60]. Concerning the theory to study the observations we are going to base on [4, 11, 30, 61–65], where very useful universal laws can be found. Also at the Introductory Chapter the theory used here can be consulted. To understand the dynamics, we show observations of three kind of experiments. In the first experiment, we condense the pure substances on different repellent substrates to study their dynamics. In the second experiment, we first condense water vapor until to obtain certain mean radius of droplets and then, we condense HMDSO vapor. Then, we repeat the experience condensing first HMDSO vapor and then, water vapor. In the third experiment, we simultaneously condense both substances at different variations of flow's values.

5.2. Experimental Procedure and General Observations

The surface used to perform the experiments is a common cover slip glass coated with 3M ECG-1700® (hereafter called 3M). Before performing any experiment, the condensation chamber is coated with 3M to avoid premature condensation of vapors. The hexamethyldisiloxane ($C_6H_{18}OSi_2$ or HMDSO) and ultra pure water have been chosen to condense because they are immiscibles and they do not chemically react. The HMDSO evaporates easily and its dew point temperature is approximately 10 °C under the 24 °C. Its contact angle achieved on common surfaces is small, no more than 7°. On the substrate coated with 3M the contact angle achieved is 65° (see Chapter 2). Water dew point temperature is just 1.5 °C under the 24 °C and its contact angle on our 3M-coated substrate is 92°. In the case of interface water-HMDSO, the developed constant angle changes as the concentration of HMDSO substance changes (Figure 5.1). We are not going to pay to much attention to this complex part of the experiment during the data analysis. For all observations, we kept the substrate at 5 °C and the vapors were produced by bubbling air inside the flasks where the substances were stored. The procedures performed for each type of experiment were:

1. First experiment consists in to condense pure substances on the repellent surface (Figure 5.2 columns (a) and (b)). The procedure is the standard of BF.
2. Second experiment consists on condensing first one of the two pure substances and once the droplets of the pattern were formed and reached a given size $\langle r \rangle$, we stopped the vapor flow and then we flow the vapor of the other substance (Figure 5.4). We tested with water vapor to obtain several different values of $\langle r \rangle$ which are control parameters and they become the initial conditions for cluster formation. We have observed, when we first condensed HMDSO instead of water, we obtain ponds of HMDSO with some water droplets embedded.
3. Third experiment consists on condensing simultaneously both substances and to change the

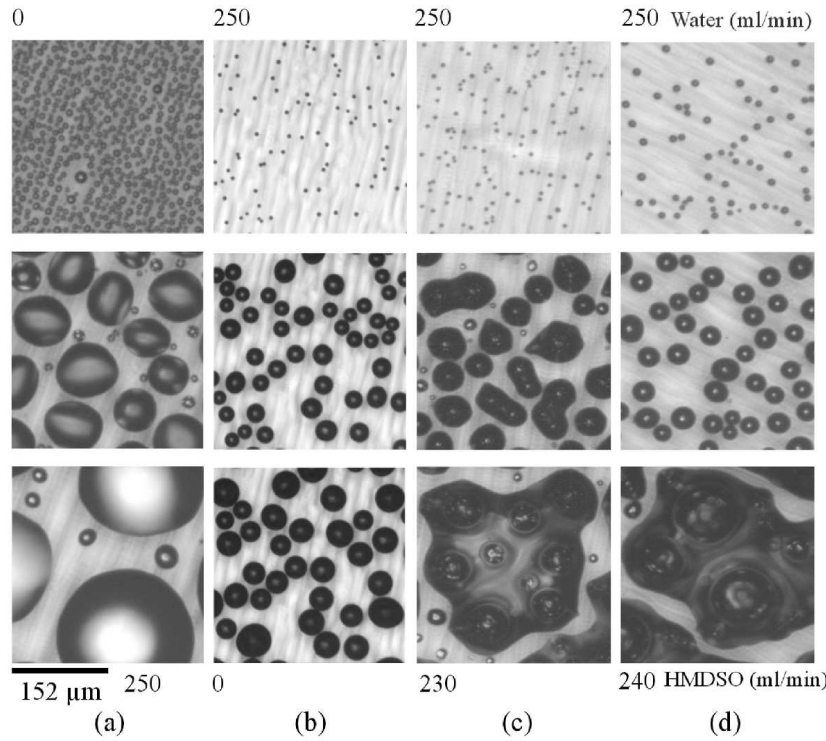


Figure 5.2: The BF evolution for HMDSO and water. The snapshots up the initial stage is represented, then the intermediate stage is in the middle and the final stage of the pattern is down. In (a) the HMDSO and (b) the ultra pure water had pumped with a flow of 250 ml/min. The water vapor flow is kept at 250 ml/min while, (c) the HMDSO is pumped with a constant flow of 230 ml/min. At the beginning, the water condenses first, then the HMDSO condenses and aggregates to the water droplets form H-W individuals. The amount of HMDSO increases to form cluster of some H-W individuals. (d) Similar to evolution than (c), now the HMDSO vapor flow is 240 ml/min.

values of the flows to observe whether we obtain cluster or ponds of HMDSO. The dynamics observed was very rich, but very complex (Figures 5.2 and 5.3).

5.2.1. First Experiment: Single Vapor Condensation

We first analyze the case where each substance condenses without interacting (Figure 5.2 columns (a) and (b)). The Figure 5.5 shows the droplet production and the average radius for each substance. The first reading of this observation is that the mean radius for HMDSO is not the expected one. It presents different droplets production and power laws of $\langle r \rangle \sim t^{1.5}$ and $\langle r \rangle \sim t^2$. The disparate behavior in comparison with water mean radius is the HMDSO condenses on preferential sites of the substrate. The 3M coating produces some grooves and it is assumable that this substance prefers some sites. This fact leads us to analyze this pattern condensation with other tools. The scaling theory whose interpretation of conservation laws for mass transfer can describe more general observations. With the BF morphology we obtain the expected growth laws that had been discussed on Chapter 1. For the case when the water and HMDSO condense

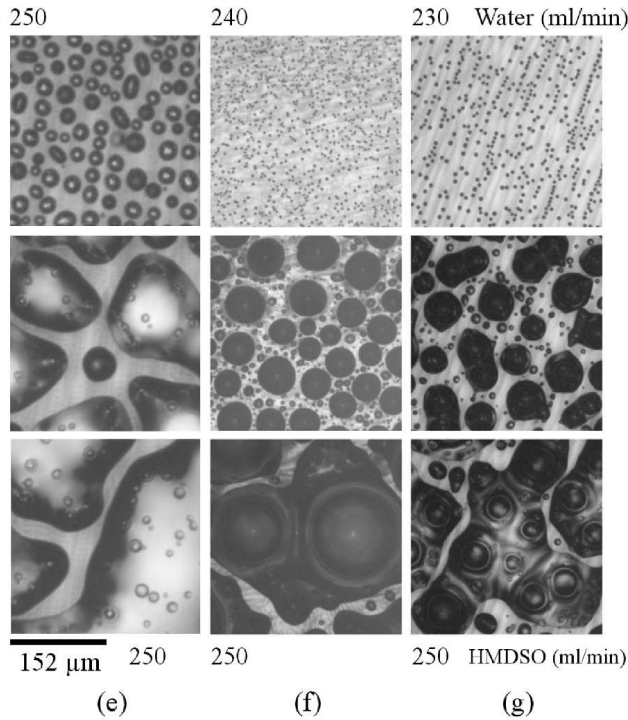


Figure 5.3: The BF of HMDSO and water. The image series up the initial stage is represented, then the intermediate stage is in the middle and the final stage of the pattern is down. The HMDSO vapor flow is kept at 250 ml/min. (e) The water vapor flow is 250/min, after the water condensation, the HMDSO condenses into a puddle around the water droplets. The HMDSO ponds grow and the water droplets are embedded. (f) the water vapor flow is 240 ml/min. At the beginning, the water condenses first, then the HMDSO condenses and aggregates to the water droplets to form H-W individuals. The amount of HMDSO increases forming cluster of some H-W individuals. (g) the flow of WV is 230 ml/min, H-W interaction is similar than the case of (f).

by separate, the maximum value of occupation factor for water is ≈ 0.63 and for HMDSO ϵ^2 is ≈ 0.8 (Figures 5.6a and 5.6b).

5.2.2. Second Experiment: Condensing one Vapor at once

The observation of the second experiment reveals that the HMDSO does not condense anywhere exactly: it first does in areas where the population of water droplets is low and when it condenses, at the beginning the HMDSO leaves a bare space as is shown (Figure 5.4). This depletion zone is concentric to the water droplets. As the time is increasing, this area disappears completely and the HMDSO still condenses anywhere. The droplets interaction appears at the beginning. From the measurements of the droplets areas, we have calculated the occupation factor ϵ^2 , (Figure 5.6) and the evolution of the mean radius $\langle r \rangle$. A representation more quantitative of the diagram Figure 5.7 is shown in Figure 5.8. In this case, the comparison between the initial conditions and the final stage exhibits two domains where the lack of structures is due to the low value of the occupation factor of water, and when there are clusters, their size depends on

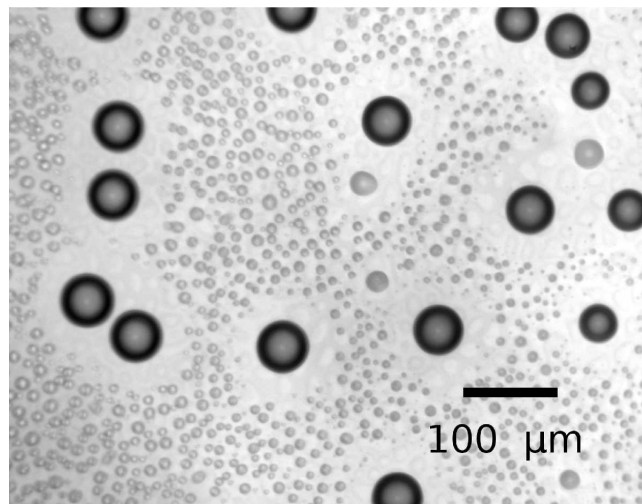


Figure 5.4: HMDSO condensing on a water *Breath Figure*. There is a bare zone between the water droplets and the just condensed HMDSO due to the water vapor at surface level and because the water is "HMDSO-scopic"

how large is the water occupation factor is. In addition, when we tried to repeat the experiment condensing first HMDSO, stop to pump and then just flow water vapor, we could not observe other result than the production of large HMDSO ponds with water droplets embedded.

5.2.3. Third Experiment: Condensing Two Vapors Simultaneously

What we observe in all the experiments of mixed vapors condensation can be summarized (see Figures 5.2 and 5.3) as following: (1) water condenses first. (2) Soon after the HMDSO does. (3) During the HMDSO condensation, the coalescence stage is achieved very fast and the intermediate stage no longer rules the drop-wise mechanism. On the empty spaces, new generations of the same substance form. As a consequence of this activity, the empty spaces among the water droplets are filled rapidly. This drives the pattern to produce H-W aggregation. Also we have observed that not all concentrations of vapors achieve H-W aggregations. Another possibility is to observe ponds of HMDSO and some droplets embedded in those ponds. We do not focus on this situation. We want to find the conditions to observe H-W individuals. By the experimental observation we have obtained that the aggregation depends on the occupation of water droplets. This means that the amount of condensed water determines the final stage of the evolution of the pattern.

5.3. Results

To describe the process of cluster H-W formation we put the results of the three experiments together. For that reason, in the following we will show results and later we are going to compare those results.

For the **first experiment**¹, the dynamics of HMDSO pattern condensation can be studied applying the theory of coalescence. We use the number of droplets of HMDSO production and

¹We base the discussion of the observations and the results on the introductory Chapter 1.

its corresponding $\langle r \rangle$ (Figure 5.5a,b) on the following analysis. We have found the process of condensation does not have a homogeneous spatial distribution. The HMDSO prefers to condense on certain sites on the grooves of the coating. Also, the birth of new droplets produces almost always in the same sites. In case of water, the drops appear more likely to a homogeneous distribution rather heterogeneous. The analysis [11] suggests that if the drops have a dimension $D = 3$ whereas the surface dimension $d = 2$, and the volume of the droplets S , or average radius r , mass conservation ρ , and number production N can be consider as a function of time which obey the scaling law:

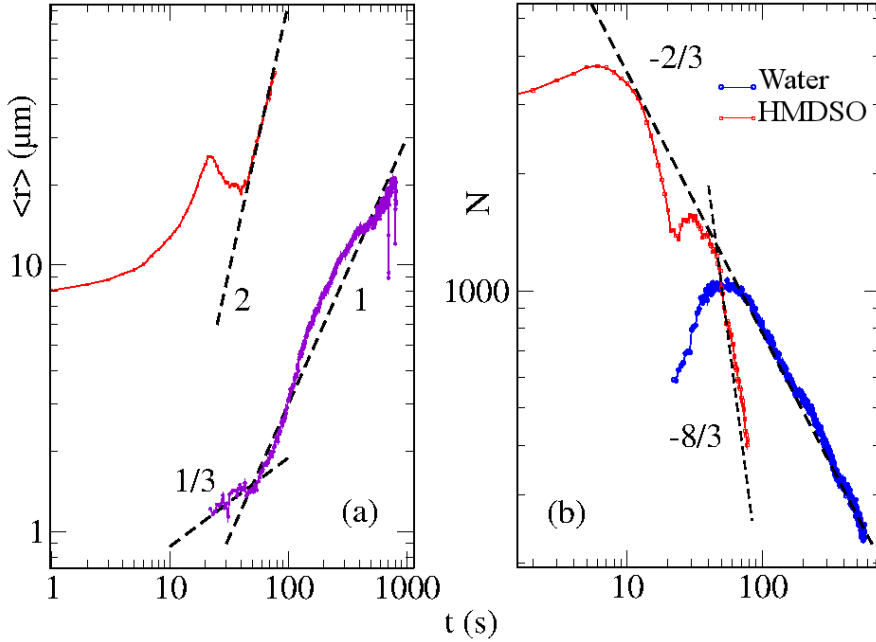


Figure 5.5: (a) The number production of droplets during the process of condensation. (b) The mean radius had obtained for BF of water and HMDSO non mixed. Those measurements are related with the Figures 5.2a and 5.2b.

$$S(t) \sim t^z, r(r) \sim t^{z/D}. \quad (5.1)$$

In the case of a homogeneous distribution

$$\rho \sim S^{2-\xi} \int x^{1-\xi} f(x) dx \sim t^{2-\xi} \quad (5.2)$$

where $\xi = 1 + d/D$, and $z = D/(D-d)$. The scaling law to describe the production of droplets is

$$N(t) \sim t^{z'} \quad (5.3)$$

where $z' = z(\xi - \tau)$. For experimental conditions, $\tau = 11$ which corresponds to value found for the production of water droplets. In case of heterogeneous distribution, the scaling law is similar to the Equation 5.2.

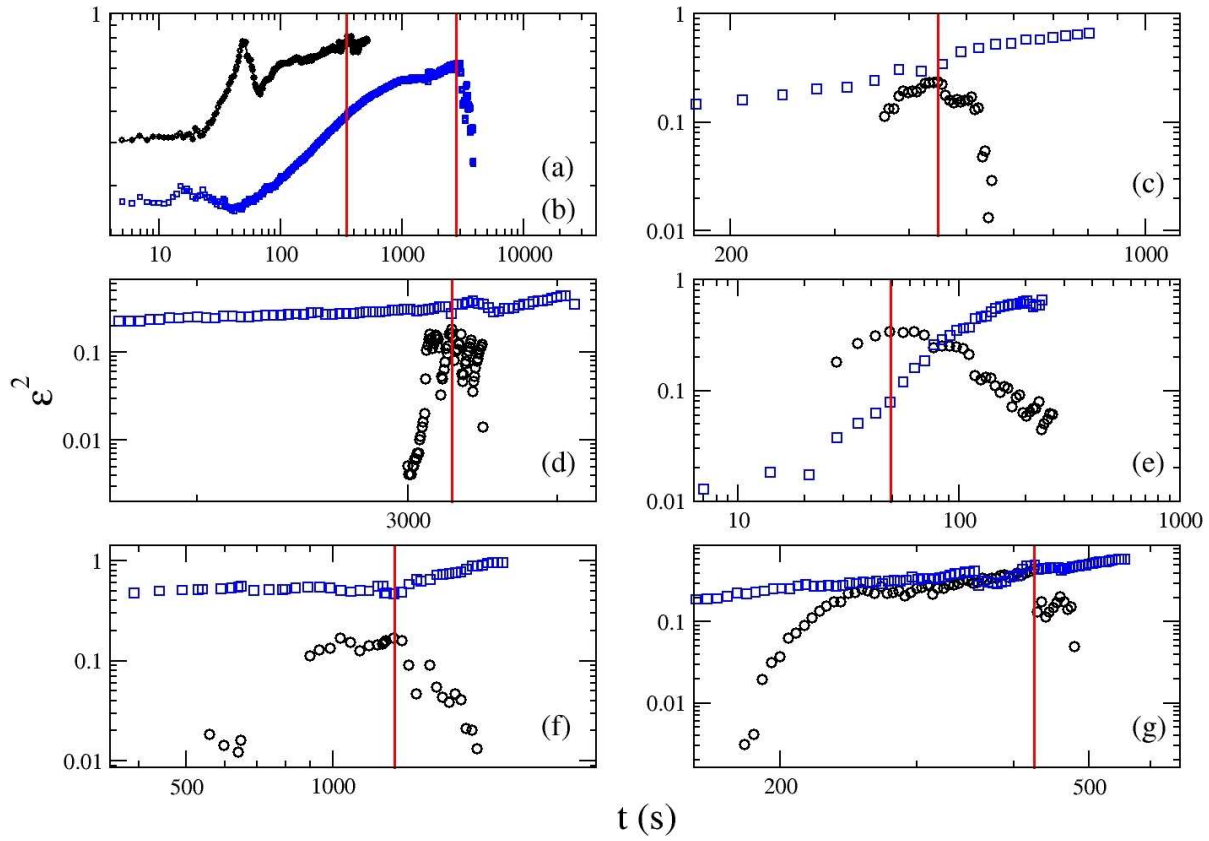


Figure 5.6: The occupation factor ϵ^2 for each value of flux of water and HMDSO vapors. Once the maximum of occupation has been reached for the HMDSO (circles), the formation of H-W begins (squares) and it increases rapidly. The order of the graph is according the flux rates presented in (Figures 5.2 and 5.3). The vertical line means signalizes when the ϵ^2 of HMDSO reaches the maximum.

$$\frac{dr}{dt} \sim r^\omega. \quad (5.4)$$

We found $\omega = 1/3$ and $\omega = 1/2$ to describe the two power laws of growth obtained during the process. The exponent ξ is always related to the dimension of the droplets and the surface, so we kept it equal to $5/3$. Comparing the exponents found for N with the equation,

$$N(t) = S^{1-\xi} \int x^{-\xi} f(x) dx \sim t^{z'(1-\xi)} \quad (5.5)$$

the exponent $z' = d/(1 - \omega)$ has two values. $z' = 2$ and $z' = 4$ which correspond to the power laws 1.5 and 2 respectively. We can understand why the exponents of the power laws for the water droplets and cluster growth are so different: when we mix two vapors we affect the way one compound can find a site. The compound presents a heterogeneous distribution and, depending on the concentration, it will force the other component to present a heterogeneous distribution, too. We observe this in the shape of power laws presented for the intermediate

stages (Figure 5.20) where the growth law $\langle r \rangle \sim t^{1/3}$ is comparable to the values found. In the case of HMDSO (Figure 5.21) the heterogeneous condition in the growth laws is evident.

In the **second experiment**, we have developed the following observation: first we had pumped water vapor to the chamber observing the droplets to not grow enough to coalesce. Then, we have stopped the flux of water vapor and we wait until the growth activity on the surface diminish. Then, we have streamed HMDSO vapor. The condensation of HMDSO has not taken too long. In some cases, if the system has droplets too big, we will observe few events of coalescence previous to the HMDSO condensation. After that, we have computed the occupation factor and the average radius to find an initial condition or parameter to let us predict what kind of pattern we shall obtain. In (Figure 5.7), we show the values of average radius and occupation necessities to produce one pattern or other. In Table 5.1 are shown the results of the observations and their respective references to Figures of this experiment.

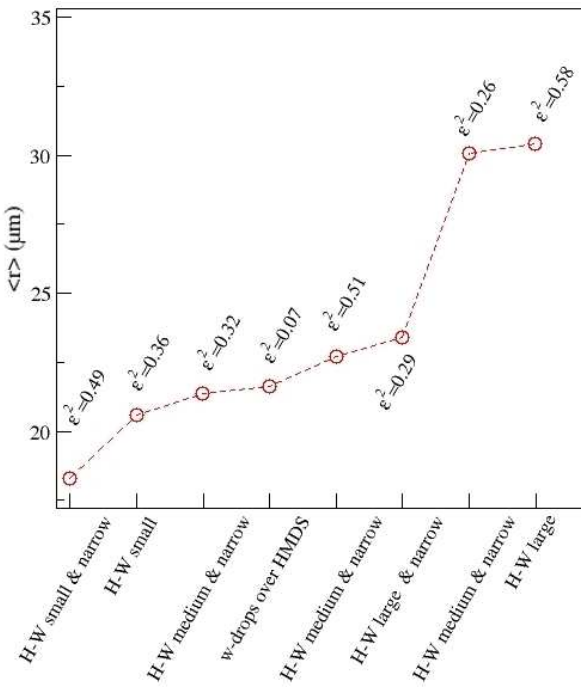


Figure 5.7: Conditions of average radius and occupation factor to determine the cluster formation. When we mention small, medium or large, we refer to the size of the water droplet embedded in HMDSO ($H-W$). And when we mention narrow, we refer to the mean distance between two $H-W$.

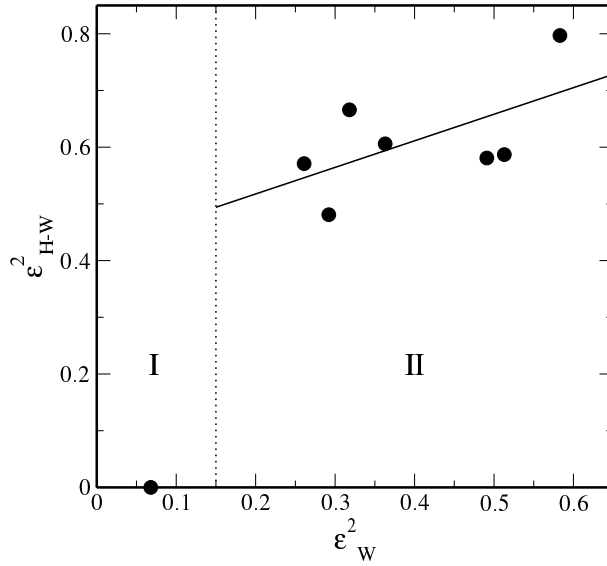


Figure 5.8: The final occupation (ϵ^2_{H-W}) is compared with the size occupation of water ϵ^2 before. It is possible appreciate the existence of a minimum condition to observe H-Ws. All indicates that the water drops have a very important role in the structure formation.

First substance to condense	ϵ^2	cluster	Figure
Ultra-pure water	≈ 0.07	no	5.9
Ultra-pure water	0.26	yes	5.10
Ultra-pure water	0.29	yes	5.11
Ultra-pure water	0.32	yes	5.12
Ultra-pure water	0.36	yes	5.13
Ultra-pure water	0.49	yes	5.14
Ultra-pure water	0.51	yes	5.15
Ultra-pure water	0.58	yes	5.16
HMDSO	0.61	no	5.17
HMDSO	0.65	no	5.18
HMDSO	0.73	no	5.19

Table 5.1: On this table we summarized the information of occupation reached for droplets of ultra pure water and HMDSO and if the clusters were observed at the time of making flow a second vapor.

In case of the **third experiment**, we have observed that after getting ϵ^2 's values (Figure 5.6), we may ask why does the HMDSO takes too long to start the condensation? One possible reason could be that the water droplets on the intermediate stage grow by the absorption of the molecules which are nearby the contact line [9]. Once the water droplets have reached enough size (and the concentration of molecules is near to zero) the partial pressure on the surroundings have decreased. In consequence the HMDSO dimers finally find empty sites to condense on the surface. We have observed through the ϵ^2 for water, when the condensation activity reaches a certain value of occupation larger than ≈ 0.2 , the BF of HMDSO appears on the surface (Figure 5.6). The HMDSO does rapidly and once have self reached the maximum of occupation, immediately

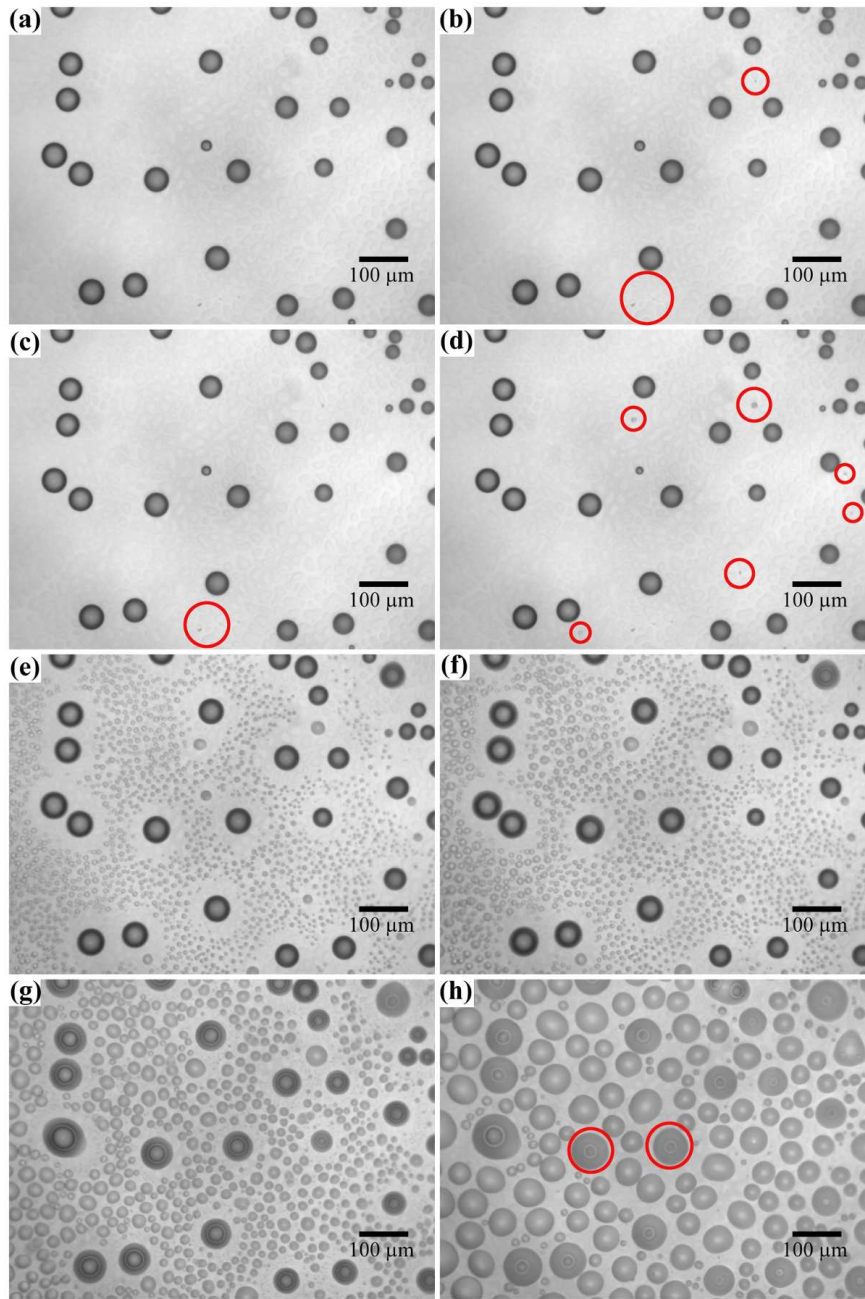


Figure 5.9: (a) The occupation factor is $\epsilon^2 \approx 0.07$. After the flow of water vapor is stopped, and some time was waiting without flowing any vapor, we flowed HMDSO vapor. (b) Some HMDSO droplets appear and some of them are marked with a red circle. (c)-(g) We observe the evolution of pattern condensation of HMDSO interacting with the water droplets. (h) No clusters were observed. A possible cause could be there were not large enough water droplets. Some water droplets are embedded on the HMDSO ponds and are marked with a red circle.

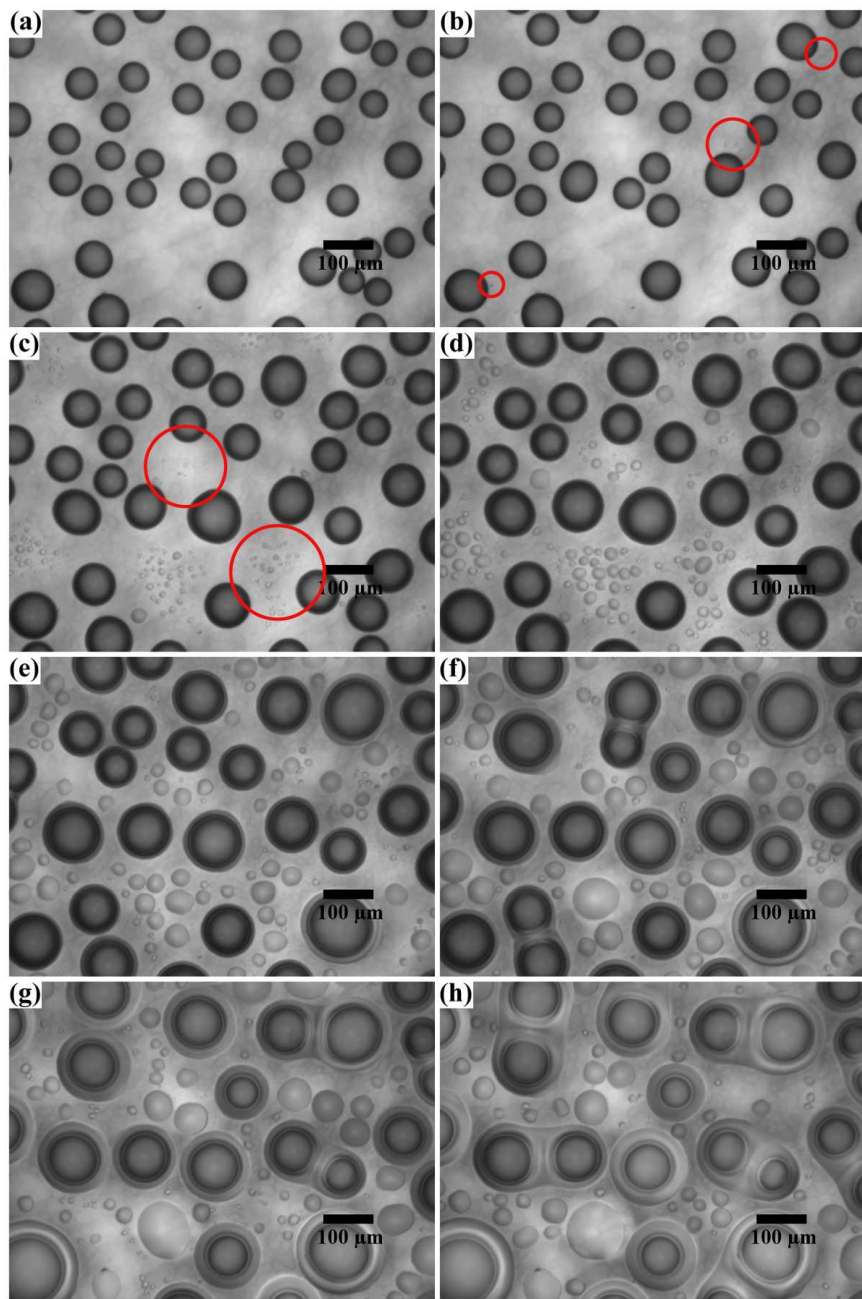


Figure 5.10: (a) The occupation is $\epsilon^2 = 0.26$ and the HMDSO was flowed. (b)-(c) Some droplets of HMDSO are marked with a red circle. (d) The HMDSO does not touch the water droplets, even some depletion zone around the water droplets is observed. (e)-(g) Suddenly, the HMDSO breaks this depletion zone and aggregates near the contact line of the water droplets. We can say that the cluster formation has started. (h) At the final stage, some clusters are visible.

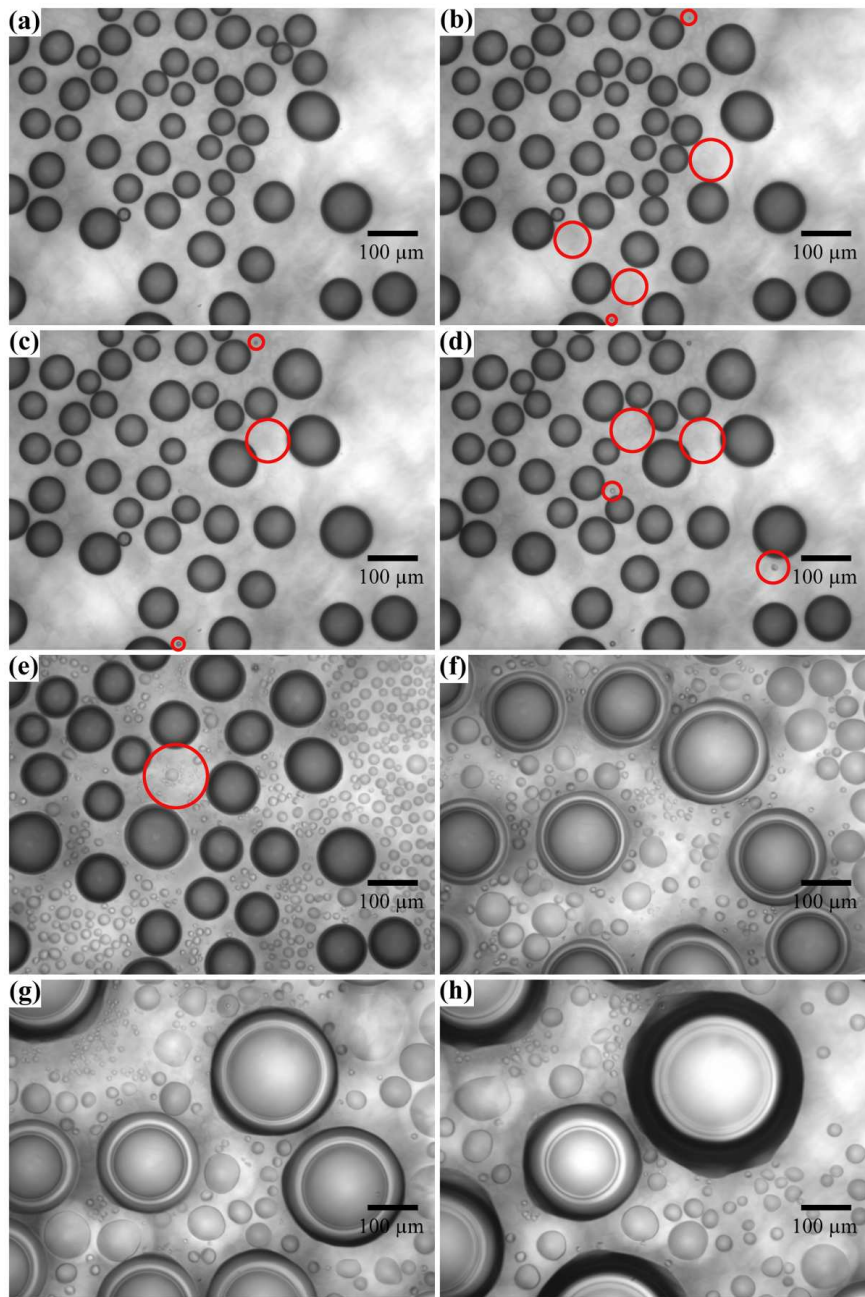


Figure 5.11: (a) The occupation factor is $\epsilon^2 = 0.29$. (b)-(d) Some HMDSO droplets appear, those are marked with a red circle. (e)-(g) The number of water droplets has diminished but, their size has increased. (h) Some H-W can be observed.

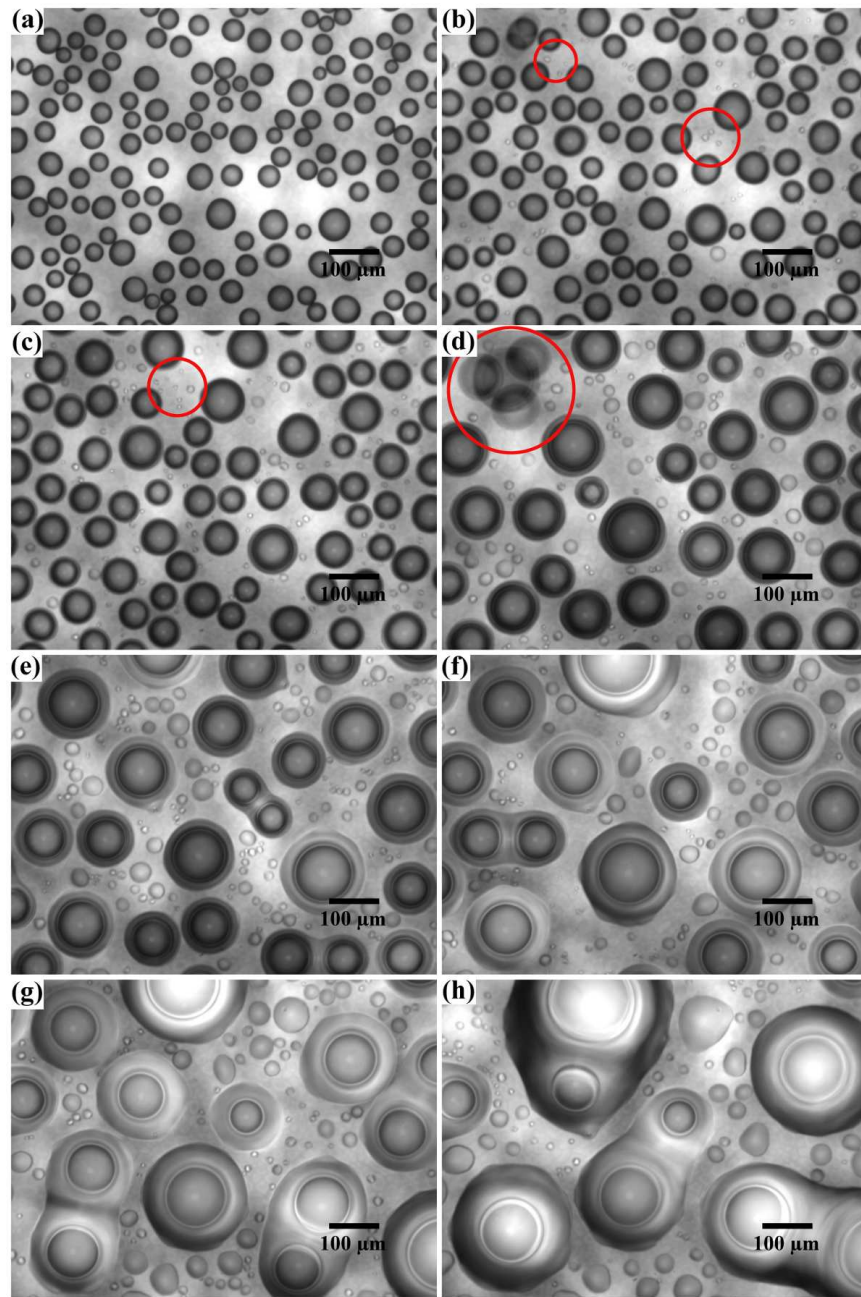


Figure 5.12: (a) The occupation factor is $\epsilon^2 = 0.32$. (b)-(c) Some HMDSO droplets appear. (d) In a red circle is marked the coalescence of three water droplets surrounded by HMDSO. (e)-(h) Early we can observe the formation of H-Ws.

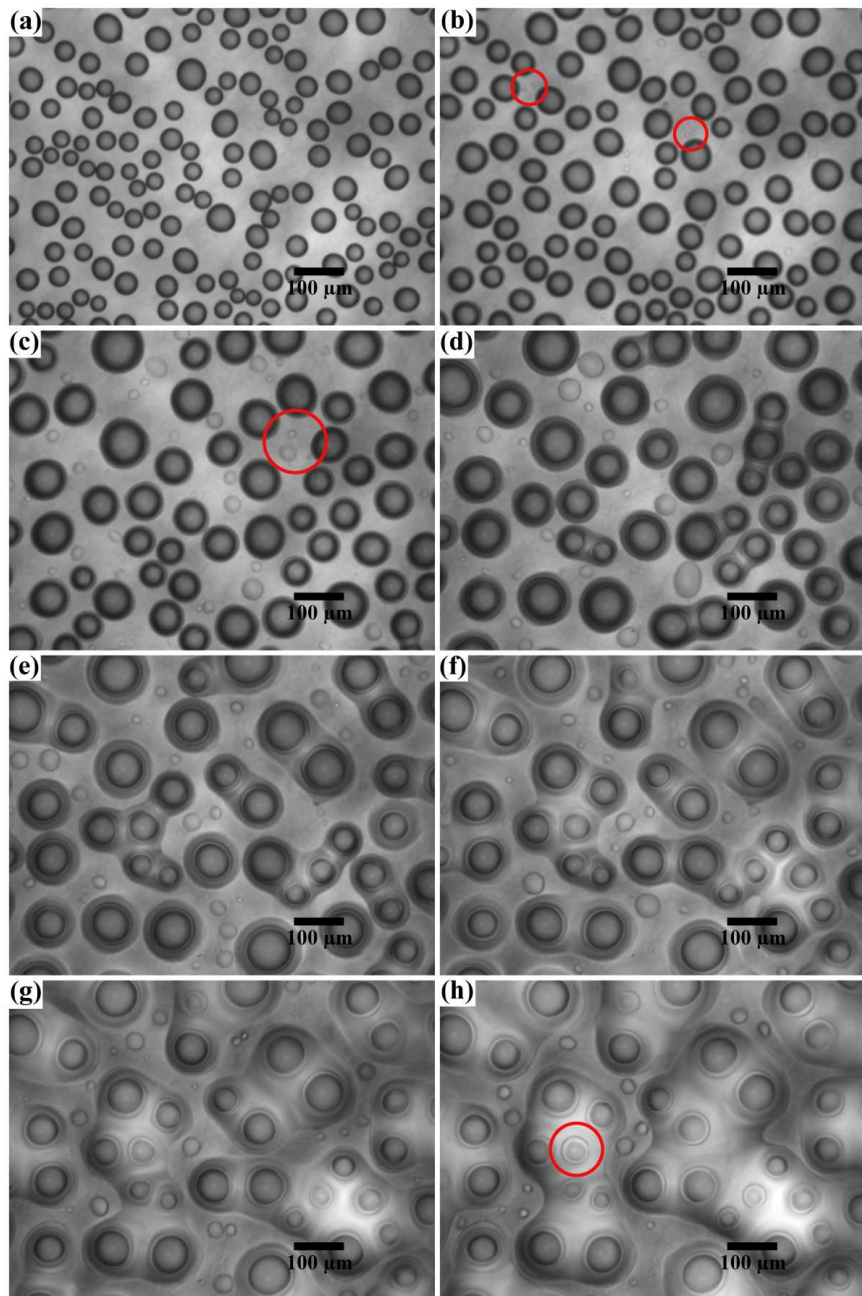


Figure 5.13: (a) The occupation factor is $\epsilon^2 = 0.36$. (b)-(c) The HMDSO condenses and a large size droplets appear on the substrate. Those droplets surround the water droplets. With red circles we mark the places where HMDSO has been observed. (d)-(f) The cluster have appeared on the substrate and those grow and aggregate to other clusters. The coalescence of water droplets is also observed, even without any flow of water vapor. (g)-(h) As we flow HMDSO vapor, we observe clusters, but the water droplets are embedding on the ponds of HMDSO. With red circles we mark the place of the embedded water droplets.

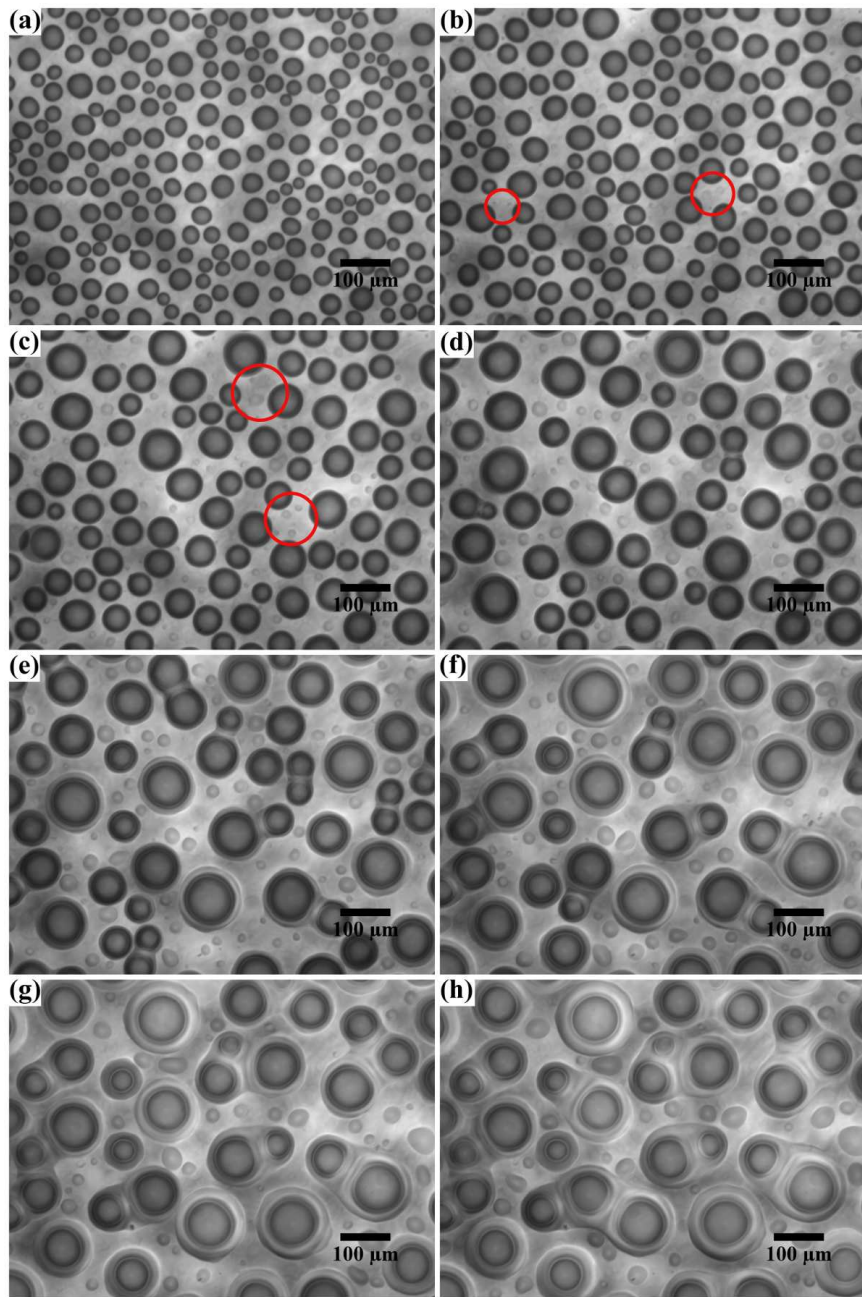


Figure 5.14: (a) The occupation factor is $\epsilon^2 = 0.49$. (b)-(c) Some HMDSO droplets appear near to the water droplets (red circles). (d)-(e) The aggregation of H-W clusters is visible. (g)-(h) The final stage of cluster formation.

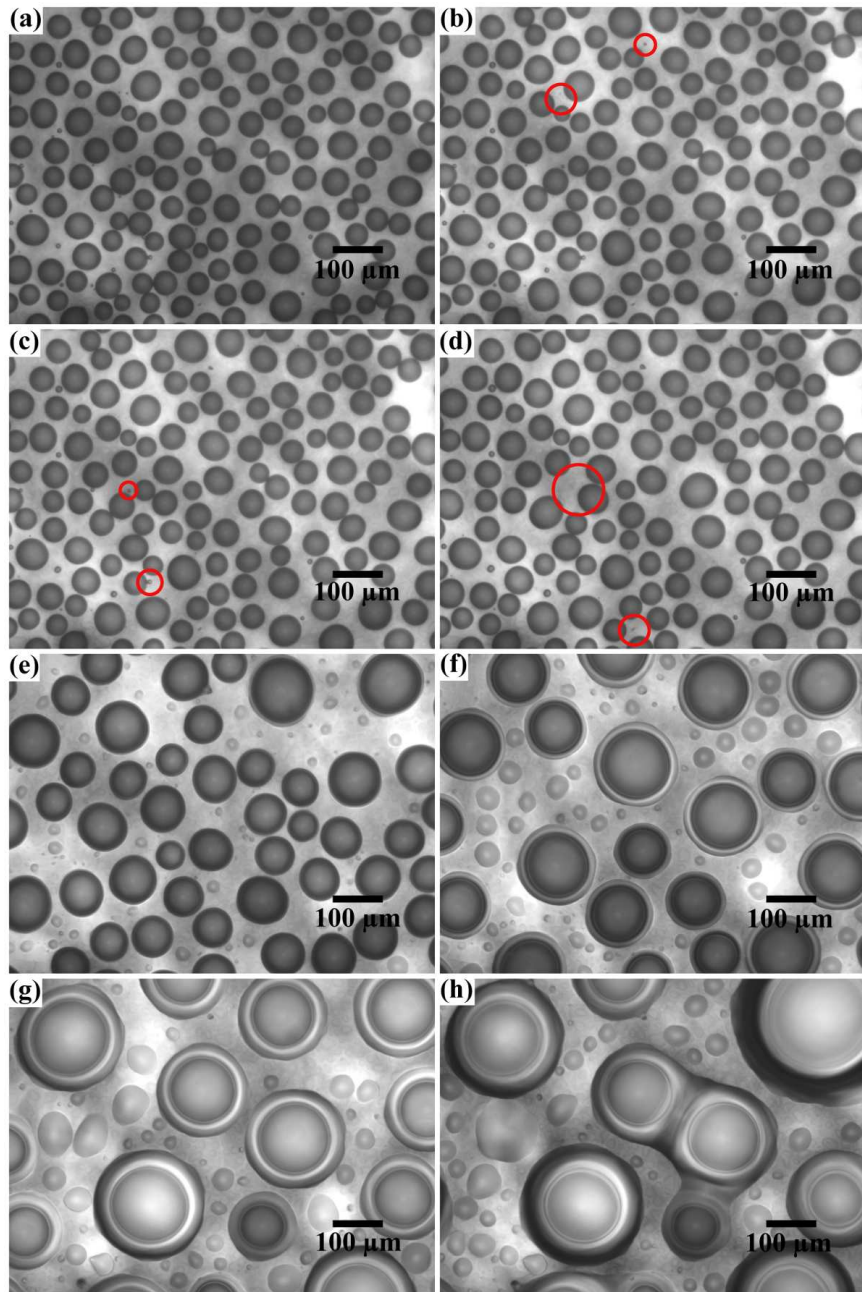


Figure 5.15: (a) The occupation factor is $\epsilon^2 = 0.51$. (b)-(e) Some HMDSO droplets appear on the empty spaces of the substrate (the red circles show where are some HMDSO droplets). (f) The HMDSO droplets surround the water droplets and the aggregation process boosts the coalescence of water droplets. (g)-(h) The large H-Ws continue aggregate until the cluster formation.

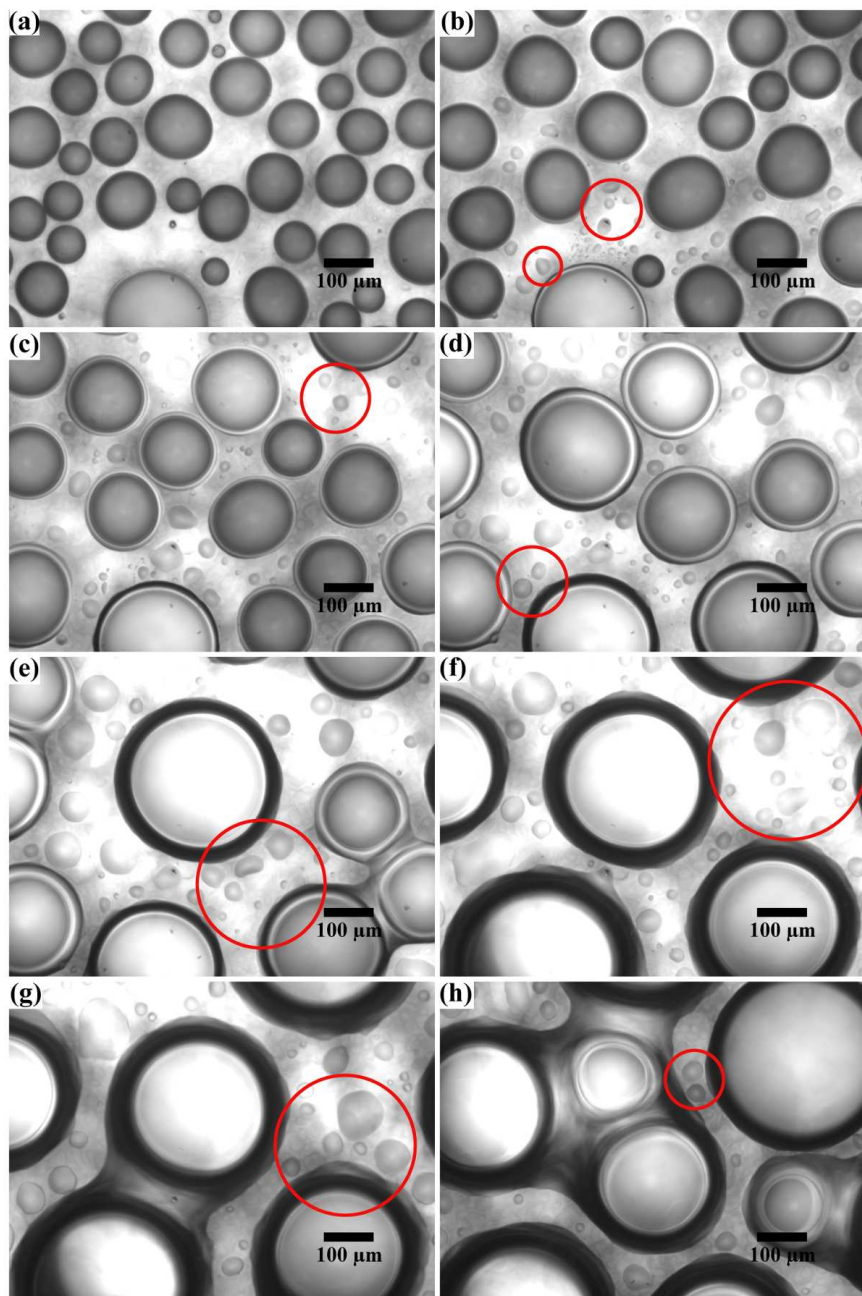


Figure 5.16: (a) This is the largest occupation factor observed on this experiment, $\epsilon^2 = 0.58$. (b)-(d) In red circles some HMDSO droplets. (e)-(f) The large size of water droplets is reached by coalescence. This part of the process draws attention because those large water droplets let free empty space to condense more HMDSO. (g)-(h) The H-Ws aggregate each other to form clusters.

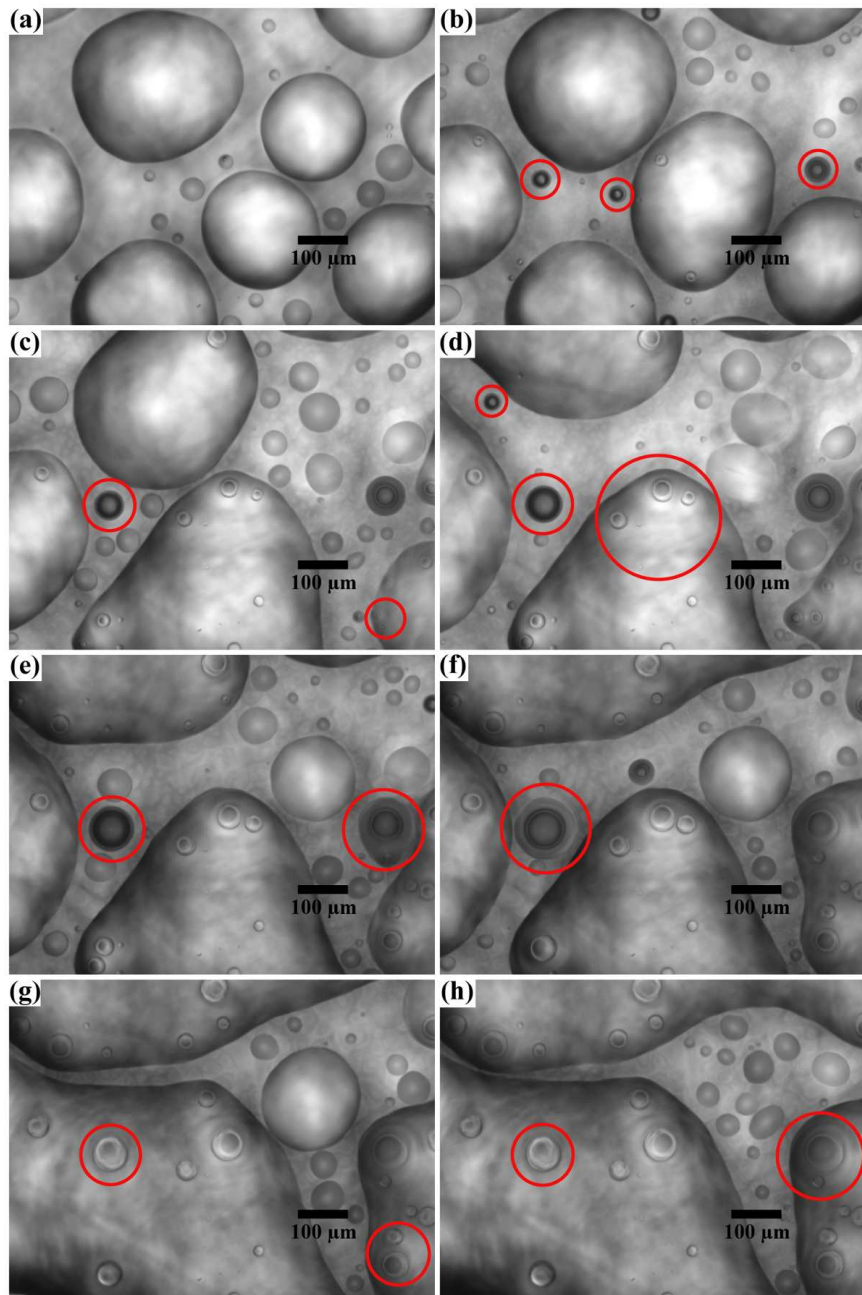


Figure 5.17: (a) The HMDSO occupation factor is $\epsilon^2 = 0.61$. (b)-(e) The water vapor condenses anywhere, even over the HMDSO ponds. (f)-(h) The HMDSO ponds spread and expand while the water vapor is still condensing (water droplets in red circles).

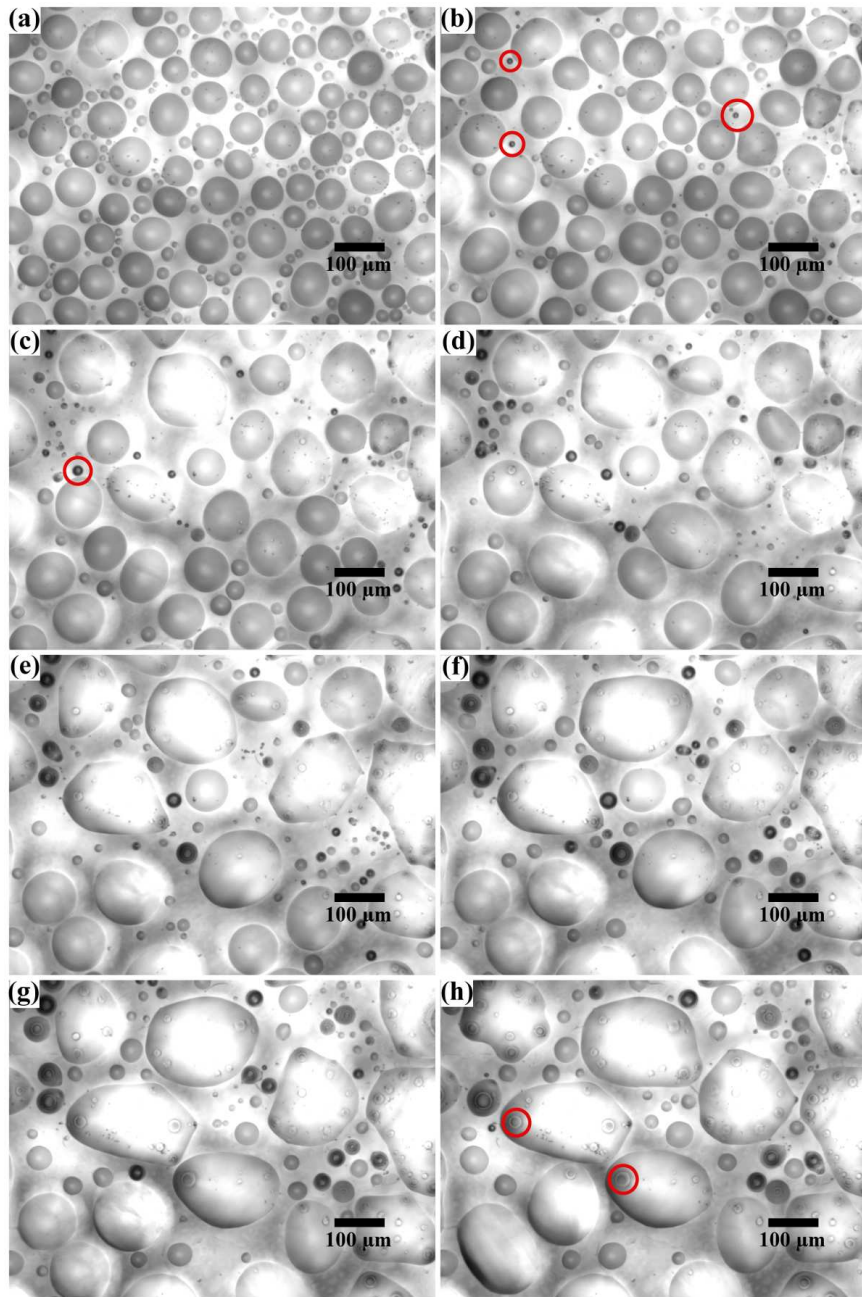


Figure 5.18: (a) The HMDSO occupation factor is $\epsilon^2 = 0.65$. (b)-(e) The water vapor condenses anywhere. In red circles the water droplets can be found. (f)-(h) The HMDSO droplets do not form ponds and the water droplets appear embedded (see the red circles).

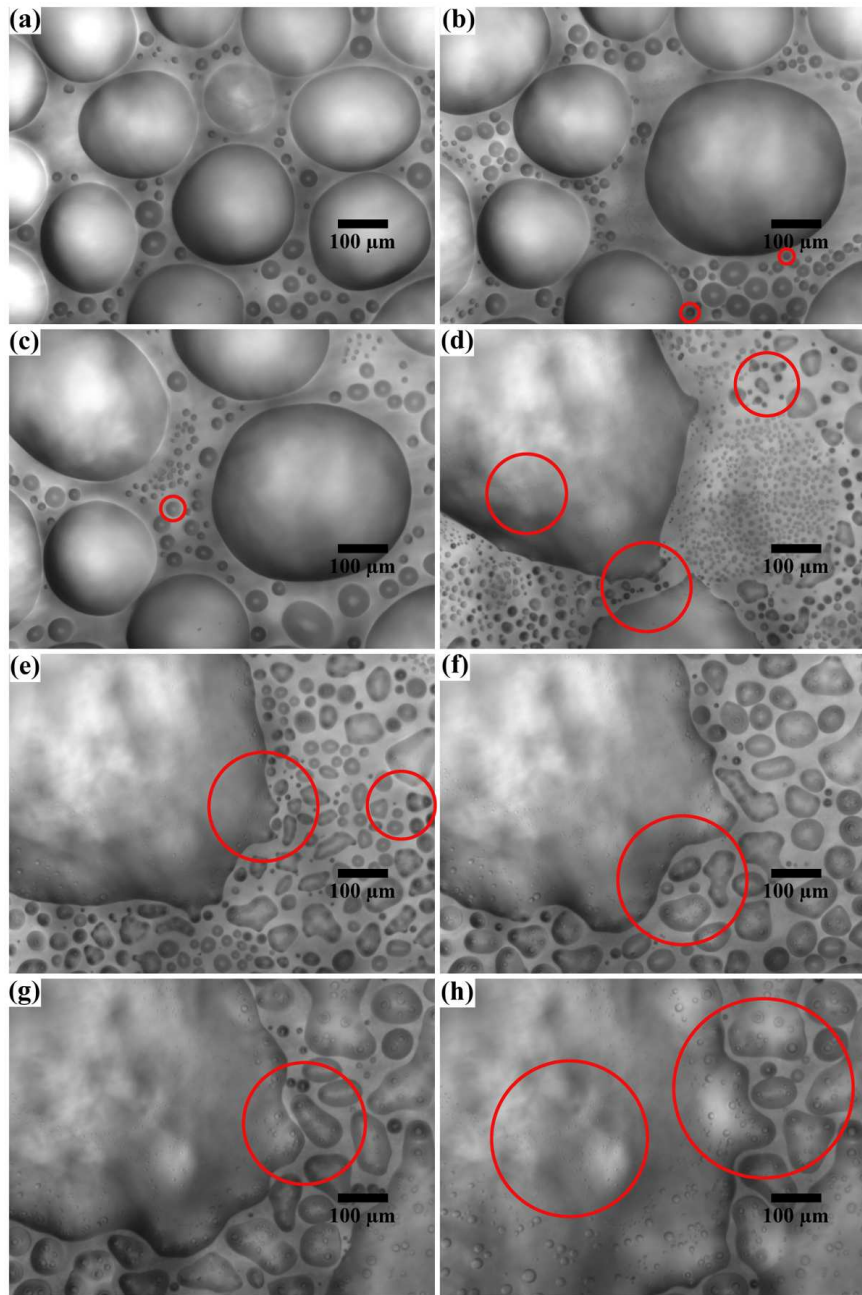


Figure 5.19: (a) $\epsilon^2 = 0.74$ is the largest value of occupation factor for this experiment. Due to the large amount of HMDSO on the substrate, when the water vapor condenses (red circles), HMDSO ponds spread all around but part of this material form again small droplets (c)-(f). (g)-(h) it is possible to observe some H-Ws structures on the red circles.

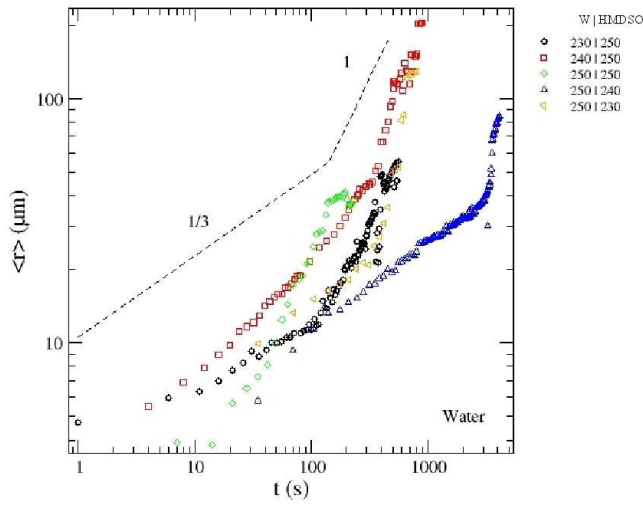


Figure 5.20: The radius average for the water droplets of BF presents two stages: the small values of $\langle r \rangle$ represent the intermediate stage almost represented for the law $1/3$. The rest of the values represent the mean size of the H-W.

the HMDSO starts the interaction with water droplets. Other result was that the condition of the cluster formation of H-W individuals depends on the mean radius of the water droplets. If the droplets are not large enough, HMDSO will form ponds. Otherwise, if the mean radius of the droplets is enough large, the HMDSO rapidly participates on the water coalescence, i. e., the cluster formation. The mean radius of the droplets for both substances have been analyzed too. We have found the mean radius $\langle r \rangle$ for water droplets has changed. The intermediate stage and the coalescence still exist but they do not have the classical result $\langle r \rangle \sim t^{1/3}$ and $\langle r \rangle \sim t^1$. We found that the exponents do not change systematically as the values of the flux (concentrations) do it. According to Figures 5.2 and 5.3, the corresponding average radius are in Figures 5.20 and 5.21.

Ref. WV / HMDSO (ml/min)/ stage	const.	α
230/250/2nd	3.40 ± 0.04	0.30 ± 0.01
230/250/3rd	0.1 ± 0.1	1.00 ± 0.02
240/250/2nd	2.10 ± 0.05	0.50 ± 0.01
240/250/3rd	0.0 ± 0.5	1.30 ± 0.08
250/250/2nd	1.4 ± 0.3	0.4 ± 0.1
250/250/3rd	0.4 ± 0.3	1.0 ± 0.1
250/240/2nd	2.00 ± 0.03	0.400 ± 0.004
250/240/3rd	0.0 ± 1.5	3.0 ± 0.2
250/230/2nd	3.1 ± 0.1	0.34 ± 0.01
250/230/3rd	0.0 ± 0.8	2.3 ± 0.1

Table 5.2: The relation $\langle r \rangle \sim t^\alpha$ fitted values from experimental results (Figure 5.20). The correlation values are in the interval of 0.99 - 0.94.

The HMDSO vapor on the surroundings affects the rate of growing of the water droplets. In

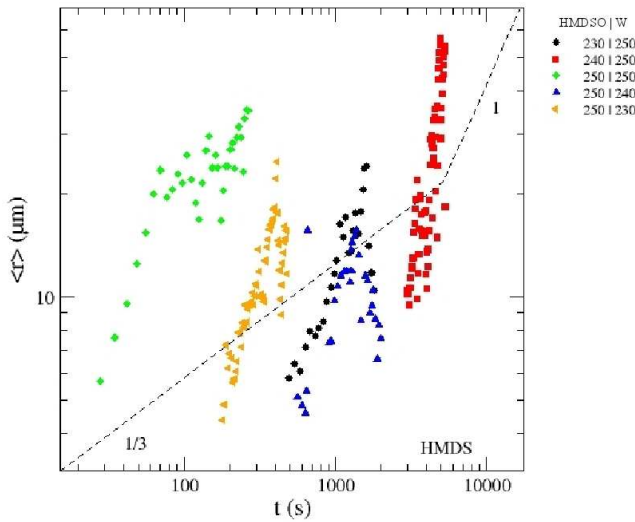


Figure 5.21: The radius average for the HMDSO droplets of BF.

Ref. WV / HMDSO (ml/min)/ stage	const.	α
230/ 250	0.0 ± 0.4	1.2 ± 0.1
240/ 250	0 ± 1	2.6 ± 0.2
250/ 250	0.03 ± 0.23	1.6 ± 0.1
250/ 240	0.0 ± 0.6	1.4 ± 0.1
250/ 230	0.0 ± 0.4	1.6 ± 0.1

Table 5.3: The relation $\langle r \rangle \sim t^\alpha$ takes the fitted values from experimental results (Figure 5.21). The correlation values are in the interval of 0.99 - 0.93. The fluctuations given the high activity of the BF formation do not let to have a smooth and large region of values to determine $\langle r \rangle$. Instead of this, it is preferable to remove the steps in order to have a continue curve at least with the same tendency.

the case of the values for water droplets, we have computed the $\langle r \rangle$ in two parts: for the mean radius of droplet in the intermediate stage and the mean size of H-W. The end of the intermediate stage is when the HMDSO begins to aggregate. We report $\langle r \rangle$ for the HMDSO only for droplets which are in the empty spaces. In Figures 5.20 and 5.21 the values of $\langle r \rangle$ are compared with the laws of $1/3$ and 1 . For different fluxes some other power laws have been computed. From Tables 5.2 and 5.3, we are going to take the corresponding exponents of the coalescence stage to study the polydispersity with the analysis proposed to study the first experiment. Solving the Equation 5.4, we obtain that the ω is

$$\omega = \frac{\alpha - 1}{\alpha} \quad (5.6)$$

Once the values of ω have been obtained. Now, we want to know how the number of droplets decays. According to Equation 5.5 in a first approximation $N(t) \sim t^{\zeta'(1-\xi)}$, we can assume the results of Figure 5.22 and 5.23 where we can predict the dynamics of aggregation.

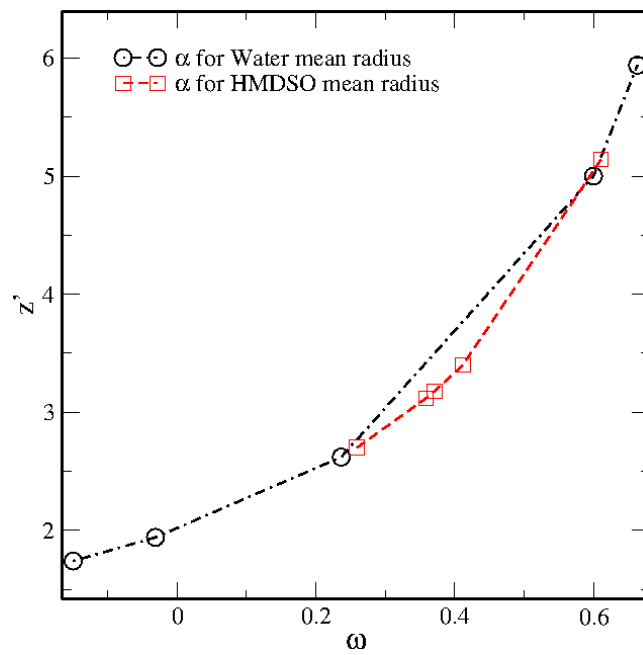


Figure 5.22: From the values of α for the third stage (Tables 5.2 and 5.3) we obtain the values of ω and z' .

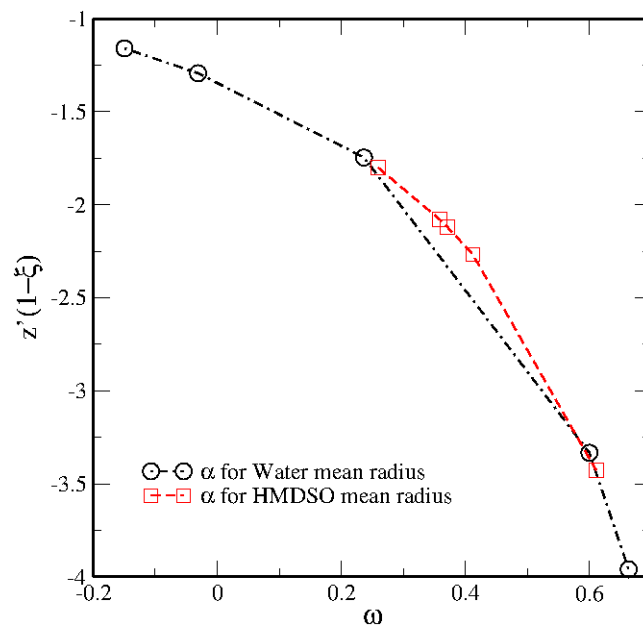


Figure 5.23: How the number droplets decays $N(t)$ is predicted as a function of concentration and the size of clusters.

5.4. Summary and Concluding Remarks

We described the condensation of two immiscible vapors when one component condenses with spatial homogeneous distribution and the other has heterogeneous distribution. The distinction was done by applying scaling laws and observing the average radius evolution for the mixing in different concentration of vapors. We can conclude that the cluster production depends totally on two factors: the mean radius and the occupation ϵ^2 to obtain different configurations and clusters of different sizes. Meanwhile, we also observed that the action of remaining not condensed vapor in the surrounding of water droplets affects the condensation of the HMDSO. The possible explanation that we can do is: when that water vapor reduces its pressure because it was absorbed by the water droplets or because the second vapor increases its pressure to break the barrier necessary to reach the condensing pressure. We should mention, other experiments must be developed with different immiscible substances in order to observe the mechanism of more periodic patterns.

Conclusions and Outlook

Conclusions

BF phenomena are ruled by several parameters. The most important variables are the temperature, pressure, surface tension, vapor saturation and hydrodynamic flows. At microscopic level, the interaction of molecules of vapor with defects on the surface also affects the contact angle of droplets. However, other parameters related with chemical potentials and bounds can be involved on the dynamics, like in the case of ice propagation. At the laboratory, we controlled the temperature, the flow of vapors, and the liquid-solid contact angle. We could measure the radii of drops. We characterized the dynamics when the BF is in a presence of a humidity sink (Chapter 2). Because the humidity sink has a radial geometry, we suggest the Fick's law $J = -D\nabla n$ in radial coordinates is the solution for the molecules' flux. Through the mathematical solution, we studied the relation between the water vapor flowed to the chamber and the time crossing of the depletion zone and the radius of the salty drop. This attempt helps us to depict the pressure gradient within the depletion zone and the singularities produced by the BF pattern and the salty drop's perimeter. This latter result is a clue to know the saturation pressure of vapor in the surroundings of BF. In brief, the conclusions can be summarized as:

1. The depletion zone exists because there the vapor is not supersaturated and it cannot condense.
2. The width of the depletion zone δ could be described as a solution of Bessel's polynomials and exponential function using the value of the radius of a sink R . This result lead us to set a model of condensation to understand the depletion zone around the salty drop. This model allows to compute the profile of the pressure in the depletion zone.

The relevance of the BF (with ultra-pure water) on frost formation and propagation of ice was discovered during experiments (Chapter 4). The classical description of $\langle r \rangle \sim t^{1/3}$ is also valid and applicable for the intermediate stage of supercooled water droplets. The recognition of the phase transition from liquid into solid is done through ϵ^2 . The phenomenology is very rich in physical processes like the coexistence and interaction between solid, gas and liquid phases of water. Those interactions can be classified into percolation and deposition. The process of evaporation through $dm/dt \sim dR^3/dt$ obeys the law $R(t)^2 = R_0^2 - t\alpha$ where R_0 is the initial radius of two droplets separated by a distance d_0 . Those results were corroborated with the experimental measurements. The velocity of propagation is measured as the dendrites growth at expense of water droplets. From those measurements it is possible to describe the conditions of minimum droplet's radius and critical time for the percolation process to exist. In other experiments performed at the same

conditions, we studied also the anisotropy of water vapor condensation and the adsorption by a humidity sink. We found how is the impact on the adsorption process when the BF pattern is homogeneous or not. In this way, it is left to work on the theoretical explanations and more controlled experiments.

We described the condensation of two immiscible vapors when one component condenses with spatial homogeneous distribution and the other has heterogeneous distribution. The distinction was done applying scaling laws and observing the average radius evolution for the mixing in different concentration of vapors. We can conclude that the cluster production depends totally on two factors: the mean radius and the occupation ϵ^2 to obtain different configurations and clusters of different sizes. Meanwhile, we also observed that the action of remaining vapor in the surrounding of water droplets affects the condensation of the HMDSO. We can explain that the water vapor reduces its pressure because it is adsorbed by the water droplets (the second vapor increases its pressure to break the barrier necessary to reach the supersaturation pressure).

Outlook

Two branches of research can grow from this thesis work. The first one, is the field of the hydrodynamics and microfluidics to study complex flux inside the condensation chamber with walls at different temperatures in order to have forced convection, other work can be the study of the vapor flow just in the interface liquid gas of the drops. With this study, we could prove the assumption that all the vapor feeds the growing drops by the contact line. This work will be performed in collaboration with School of Science (UNAM) in México and School of Science (University of Navarra). Another research of our interest is to understand the solution of BF when are facing anisotropies in water vapor resources. The idea is to study easy cases by simulations and supporting with experimental work, and also to test the models with real patterns. This work will be developed between three the School of Science (UNAM), School of Science (University of Navarra), and the University of Tarapacá in Chile. However in experimental research there are a lot of things left to do. Concerning the salty drop and the Breath Figure, it is left to investigate how is the behavior of other BF in presence of sinks made of others compounds. To study the arrangement of sinks and the adsorption of humidity at the contact line. Concerning the frost formation, to study the diffusion of salt on a frost pattern. For mixed vapors, to study some other substances not only immiscible but, miscible too. Like the process of washing chlorophyll from green leafs at different concentrations of water/ethanol. Also, the study of BF over beetle tenebrionid stenocara's elytra with ESPCI-Paristech in Paris, France and the distribution of temperature over the elytra's surface to induce water vapor condensation.

Appendix A

Appendix 1: Program Routines

A.1. Pre-analysis routines: Conversion PPM - JPEG

The follow routines have written to do a treatment of attributes of the image stacks. Those are displayed here in logic execution order.

Bash Script for Linux to 'cut' the area where the salty drop is placed. The size has chosen according to its maximum growth.

```
"recorte.sh"

#!/bin/bash
echo "numero de experimento"
read nnn
nom=ito$nnn
directorio=peque$nnn
mkdir $directorio
for i in $( cat $nom-originales.txt | awk '{ print $1 }' )
do
convert -quality 100 -crop 543x522+792+519 $i $directorio/$i
done
```

This Matlab routine uses a threshold matrix to analyze a stack of images. Similar as the one used on the radius of the central drop calculation, and according to the values of time and cell position, a recommended value of the threshold will be applied. Once all the image has been binarized, the routine finds the droplets geometric properties and the average radius, the occupation factor, and other values can be computed. To run this routine it is necessary to have all the exits of all previous. Another important calculation what this routine does, is the calculation of the mentioned parameters are setting as a function of the central drop radius, the depletion zone and the size of interval in turns another small interval d which depends on the minimum and maximum radius of the droplet size per interval. The next table is an example of threshold values applied to binaryze the image stack. In this case an image of 2048×1536 pixels is divided into 6×8 cells, if we count in the matrix 48 cells starting from the first column left and from the first row.

starting value								
137	132	118	111	105	99	96	89	84
149	136	129	120	108	108	97	89	89
156	145	135	132	121	115	98	95	87
156	148	138	129	121	110	97	96	89
161	148	135	123	107	105	94	100	88
154	147	133	124	116	107	95	88	85
150	143	132	127	116	116	103	95	101
152	150	137	129	118	113	98	98	106
166	158	146	132	121	121	107	103	108
174	170	158	135	121	128	110	113	105
175	164	146	129	122	124	108	102	88
172	155	141	127	111	113	102	98	100
160	147	136	128	119	124	115	106	104
172	160	154	133	122	130	129	116	114
183	182	156	166	132	159	150	129	123
188	189	166	164	138	161	149	132	123
184	188	175	130	137	149	141	114	119
184	171	153	132	125	124	111	101	100
166	161	148	133	124	124	119	108	115
151	182	160	130	112	105	137	126	131
116	111	107	110	112	105	103	101	113
116	111	107	110	112	105	103	101	113
177	188	143	171	142	152	153	148	145
191	182	166	137	128	130	119	119	108
179	167	153	140	142	132	132	127	121
183	176	169	110	107	111	104	103	153
115	114	108	110	107	111	104	103	113
115	114	108	110	107	111	104	103	113
182	201	179	110	107	176	159	103	132
200	186	183	154	146	143	139	135	131
181	176	160	147	137	130	132	121	107
175	177	172	176	155	146	148	148	139
121	113	111	111	108	110	103	103	110
113	113	108	111	108	110	103	103	110
194	192	187	193	188	135	139	145	140
204	196	175	172	154	150	134	126	113
167	168	157	142	130	127	122	113	104
191	184	167	156	150	146	146	130	116
194	184	186	164	137	149	132	129	145
196	207	209	181	161	153	153	137	145
197	201	175	158	148	145	139	122	140
201	191	159	154	155	132	135	116	124
178	169	159	141	128	129	119	109	105
182	167	156	144	136	130	126	114	104
202	174	169	151	151	135	142	132	120
201	187	171	157	149	147	135	121	113
204	182	165	148	140	140	124	115	128
204	180	159	148	143	137	117	108	104

```

clear all;
%
salidaf='gotas';
salidaf2='dist-';
muestra='ito0-';

```

```
formato='jpg';
tipf='dat';
nombre2=strcat(salidaf,tipf);
uuu=fopen(nombre2,'w+');
%
% Datos iniciales de centros X y Y.
%
format long e
frecuencia=5;
deltas=load('ito-delta.dat');
CentrosX=load('ito-centrosx.dat');
CentrosY=load('ito-centrosy.dat');
Radios=load('ito-RADIO.dat');
recortes=load('recortes'); % revisar fecha de experimento
umbral=load('thresholds'); %archivo con los valores de bin, tiempo y threshold.
[au bu]=size(umbral);
%l=0;
%for i=0:15:105
%l=l+1;
%if(i == 0)
%i=12;
%end
%tiempos(l)=i;
%end
tiempos=[4 10 30 60 120 150 240 330 450]';
l=0;
for i=0:250:2000
l=l+1;
if(i==0)
i=1;
end
if(i==2000)
i=2048;
end
h(l)=i;
end
l=0;
for i=0:250:1500
l=l+1;
if(i==0)
i=1;
end
if(i==1500)
i=1536;
end
v(l)=i;
end
recx=recortes(1,4);
recy=recortes(1,5);
factor=1.390625*500/322.58;
nft=1;
inicio=4;
%numfoto=max(size(Radios));
numfoto=450;
%
% Inicia ciclo.
%
l=1;
for nft=inicio:numfoto
nfoto=num2str(nft);
nombre=strcat(muestra,nfoto,formato);
I=imread(nombre);
```

```

cx=round(CentrosX(nft)+recx);
cy=round(CentrosY(nft)+recy);
%
% CALCULO.
% ConversiÃsn de rx.
%
dtamR=2*round(sqrt(cx^2+cy^2));
tamR=round(sqrt(cx^2+cy^2));
[tamax tamax]=size(I);
%
% CALCULO.
% ConversiÃsn de rx.
if(nft >= tiempos(1,1))
l=1+1;
end
lb1=0;
for i=1:8
for j=1:6
lb1=lb1+1;
fototest0(v(j):v(j+1),h(i):h(i+1))=I(v(j):v(j+1),h(i):h(i+1))<umbral(lb1,1);
end
end
%
% ObtenciÃsn de los radios.
[ry1 rx1]=size(fototest0);
[ito n]=bwlabel(fototest0);
ito0=regionprops(ito,'filledarea');
ito1=regionprops(ito,'centroid');
areas=cat(1,ito0.FilledArea);
centros=cat(1,ito1.Centroid);
clear ito;
clear ito0;
clear ito1;
%
% radio estimado
radioss=factor*sqrt(areas/pi);
%
% Distancia al centro de la gota.
dgotasx=factor*centros(:,1)-factor*cx;
dgotasy=factor*centros(:,2)-factor*cy;
dgotas=sqrt(dgotasx.^2+dgotasy.^2);
rdgotas=dgotas(find(dgotas>delta(nft,2)+delta(nft,3)));
%
% Salidas
[sdgotas lii]=sort(rdgotas);
sradios=radioss(lii);
discriminador=mean(sradios)/2.0;
indrad=find(sradios<factor*100.0);
srad=sradios(indrad);
sdgot=sdgotas(indrad);
parametros=[sdgot,srad];
nombre4=strcat(salidaf2,nfoto,tipf);
fprintf(uuu,'%1.f %1.f %s\n',nft*5,n,nombre4);
tamagno=size(sdgotas);
save(nombre4,'parametros','-ascii');
%clear parametros;
nft
n
end
fclose(uuu);

```

A.2. Salty-drop Analysis

- (1) To transform stacks of color images in "ppm" format to "jpg" grayscale images. This routine corresponds to **Bash** scripts programming for Linux. The entrance information is the suffix name of the file, for example, in "ito0-20101027-081103-447.ppm", the entrance name is "0". The exit name is "ito0-i.jpg" $i = 0, \dots, n$. This program produces a second exit file

”ito0-00000i.jpg” to feature a movie of the experiment, and a third file to storage the original names.

```
"tratamiento.sh"

#!/bin/bash
echo "numero de experimento"
read nnn
num=$nnn
nom=ito$num
directorio=jpgs$num
directorio1=jpgsvideo$num
let l=0
mkdir $directorio
mkdir $directorio1
for i in $( ls -A $nom-* .ppm )
do
basearxiv='basename $i ".ppm" | cut -d'-' -f1'
datearxiv='basename $i ".ppm" | cut -d'-' -f2'
arxiv2=$basearxiv"-`printf %010d $l`".jpg"
arxiv3=$nom"-`$l`.jpg"
echo $arxiv3"      "$arxiv2"      "$i >> $nom"-originales.txt
postext=473
texto='5,'${postext}', ``basename $i ".ppm"``',
tamanyoa=614
tamanyobmod=476
convert -quality 100 -colorspace gray $i $directorio/$arxiv3
convert -quality 100 -resize 30% -extent ${tamanyoa}x${tamanyobmod}
-draw "text `echo $texto`" $i $directorio1/$arxiv2
let l=$l+1
done
cd $directorio1
ffmpeg -i $nom-%010d.jpg -sameq -an -r pal -f "mpeg1video"
$nom"-video".m1v
```

- (2) Matlab routine to extract the profile of the central droplet. This routine runs with all the ”jpg” files of the stack. The exit is ”ito0-x-i.dat” and ”ito0-y-i.dat”.

```
"radiocalculador.m"

muestra='ito0-';
formato='.jpg';
nft=1;
inicio=1;
numfoto=1309;
% Para archivos de salida de datos.
% datos iniciales.
umbral2=118;
umbral1=123;
tipf=' .dat';
for nft=inicio:numfoto
nfoto=num2str(nft);
nombre=strcat(muestra,nfoto,formato);
% tratamiento.
imagen=imread(nombre);
% ajuste.
imagenrx=imresize(imagen,[1 10].*size(imagen));
imagenry=imresize(imagen,[10 1].*size(imagen));
imagen=0;
```

```
% binarizacion y borde.
bwImagenrx=((imagenrx >= umbral2)-(imagenrx >= umbral1));
bwImagenry=((imagenry >= umbral2)-(imagenry >= umbral1));
bx=max(size(bwImagenrx));
ay=max(size(bwImagenry));
imagenrx=0;
imagenry=0;
% calculos.
nombre2=strcat(muestra,'x-',nfoto,tipf);
nombre3=strcat(muestra,'y-',nfoto,tipf);
vvv=fopen(nombre2,'w+');
uuu=fopen(nombre3,'w+');
for ii=1:bx
fprintf(vvv,'%1.1d %1.6f\n',ii,sum(bwImagenrx(:,ii))');
end
for ii=1:ay
fprintf(uuu,'%1.1d %1.6f\n',ii,sum(bwImagenry(ii,:))');
end
%tiempo=(nft-1)*10;
bwImagenrx=0;
bwImagenry=0;
fclose(uuu);
fclose(vvv);
nft
end
```

- (3) Fortran routines to extract the limits of the profile of the droplet obtained for the routine above. It is necessary to create a database by hand with the necessary limits. The heads t_{in} , t_{fi} mean the interval (integers) of time where the rest of the limits are valid. x_0 , x_a , x_b , x_c , x_d , x_e mean the interval where the program is going to cut (in pixels). The next table is an example of what the program should read,

t_{in}	t_{fi}	x_0	x_a	x_b	x_c	x_d	x_e
1	10	0	1136	1364	4673	4864	5430
11	40	0	1158	1342	4666	4879	5430
41	90	0	1048	1269	4695	4901	5430
91	150	0	952	1158	4776	4908	5430
151	220	0	872	1070	4754	4967	5430
221	350	0	717	982	4850	5004	5430
351	550	0	563	857	4894	5136	5430
551	700	0	452	666	5004	5173	5430
701	850	0	372	555	5055	5232	5430
851	1000	0	276	452	5055	5276	5430
1001	1200	0	173	394	5166	5320	5430
1201	1300	0	144	298	5173	5357	5430
1301	1309	0	158	283	5202	5372	5430

This matrix is introduced in the following program:

```
"filtro.f"

program filtro
integer, parameter :: tamx0=14000,tam0=10000
integer :: ini,jn,l,cuantas,cuantos
integer :: param,paran,tami,intervalos
integer :: uno(tam0,8)
real*8 :: x(tamx0,2)
character*64 arxiv,ch(tam0),prefijo,arx,filtros
character*64 buen
```

```
print*, 'base de datos de arxivos a filtrar?'
read*,arx
open(56,file=arx,status='unknown')
print*, 'aqui'
cuantas=0
do i=1,tam0
read(56,*,end=57)ch(i)
cuantas=cuantas+1
enddo
57 continue
print*, 'intervalos del filtro?'
read*,filtros
open(89,file=filtros,status='unknown')
print*, 'almacenamiento de nombres buenos?'
read*,buen
open(55,file=buen,status='unknown')
jn=101
jm=301
intervalos=0
do i=1,tam0
read(89,*,end=18)(uno(i,j),j=1,8)
intervalos=intervalos+1
enddo
18 continue
do interv=1,intervalos
print*,interv,'[',uno(interv,1),',',',',uno(interv,2),']'
paran=uno(interv,1)
param=uno(interv,2)
do l=paran,param
jn=jn+1
jm=jm+1
arxiv=ch(l)
open(jn,file=arxiv,status='unknown')
prefijo='bueno-'//ch(l)
open(jm,file=prefijo,status='unknown')
write(55,*)prefijo
c lectura x
cuantos=0
do i=1,20000
read(jn,*,end=15)(x(i,j),j=1,2)
cuantos=cuantos+1
enddo
15 continue
maxo1=0
c borra seccion inicial de la gota.
ini=1
tami=uno(interv,4)
do i=ini,tami
x(i,2)=0
enddo
c borra seccion central de la gota.
ini=uno(interv,5)
tami=uno(interv,6)
do i=ini,tami
x(i,2)=0
enddo
c borra seccion final de la gota.
ini=uno(interv,7)
tami=uno(interv,8)
do i=ini,tami
x(i,2)=0
enddo
```

```
c escribe el vector a analizar.
do i=1,cuantos
write(jm,*)(x(i,j),j=1,2)
enddo
close(jn)
close(jm)
enddo
enddo
close(100)
end
```

- (4) Fortran routine to extract limits of the profile of the central drop in the horizontal orientation. The entrance is a file with the list of files called "ito0-x-i.dat", this file can be obtained by the execution of the Linux command,

```
ls ito0-x-?.dat > namex
```

the exit files will provide information of the radius of the central drop as a function of time, the geometric center, and the extreme coordinates for the horizontal orientation.

```
"radiosx.f"

program radios
integer, parameter :: tamx0=14000
integer :: cent,k
real*8 :: x(tamx0,2),rx(tamx0,2),R(tamx0)
real*8 :: maxo0,maxo1
character*64 ch(tamx0),arxiv,arx

print*, 'base de datos de arxivos a analizar?'
read*,arx
open(50,file=arx,status='unknown')
open(51,file='ito-radiosx.dat',status='unknown')
open(52,file='ito-centrosx.dat',status='unknown')
open(53,file='ito-extremosx.dat',status='unknown')
factor=1.390625*500/(3225.8*2)
k=0
do i=1,tamx0
read(50,*,end=18)ch(i)
k=k+1
enddo
18 continue
print*,k
print*, 'centro probable de la gota (entero>0)?'
read*,cent
jn=101
do l=1,k
arxiv=ch(l)
open(jn,file=arxiv,status='unknown')
kk=0
do i=1,tamx0
read(jn,*,end=19)(x(i,j),j=1,2)
kk=kk+1
enddo
19 continue
c print*,l,kk
maxo0=0
do i=1,cent
maxo0=max(x(i,2),maxo0)
enddo
ll=0
```

```

do i=1,cent
if(x(i,2) .eq. maxo0) goto 20
ll=ll+1
enddo
20 continue
rx(1,1)=ll
maxo1=0
do i=cent,kk
maxo1=max(x(i,2),maxo1)
enddo
ll=cent
do i=cent,kk
if(x(i,2) .eq. maxo1) goto 21
ll=ll+1
enddo
21 continue
rx(1,2)=ll
R(1)=rx(1,2)-rx(1,1)
centrox=rx(1,2)-R(1)/2
write(51,*)l*5,R(1)*factor
write(52,*)centrox/10
write(53,*)rx(1,1)/10,rx(1,2)/10
close(jn)
enddo
close(50)
close(51)
close(52)
close(53)
end

```

- (5) Fortran routine to extract limits of the profile of the central drop in the vertical orientation. Similar than the last program, the entrance would be a matrix, and the exit will provide geometric information of the central drop.

```

"radiosy.f"

program radios
integer, parameter :: tamx0=14000
integer :: cent,k
real*8 :: x(tamx0,2),rx(tamx0,2),R(tamx0)
real*8 :: maxo0,maxo1
character*64 ch(tamx0),arxiv,arx
print*, 'base de datos de arxivos a analizar?'
read*,arx
open(50,file=arx,status='unknown')
open(51,file='ito-radiosy.dat',status='unknown')
open(52,file='ito-centrosy.dat',status='unknown')
open(53,file='ito-extremosy.dat',status='unknown')
factor=1.390625*500/(3225.8*2)
k=0
do i=1,tamx0
read(50,*,end=18)ch(i)
k=k+1
enddo
18 continue
print*,k
print*, 'centro probable de la gota (entero>0)?'
read*,cent
jn=101
do l=1,k
arxiv=ch(l)
open(jn,file=arxiv,status='unknown')

```

```

kk=0
do i=1,tamx0
read(jn,*,end=19)(x(i,j),j=1,2)
kk=kk+1
enddo
19 continue
c print*,l,kk
maxo0=0
do i=1,cent
maxo0=max(x(i,2),maxo0)
enddo
ll=0
do i=1,cent
if(x(i,2) .eq. maxo0) goto 20
ll=ll+1
enddo
20 continue
rx(l,1)=ll
maxo1=0
do i=cent,kk
maxo1=max(x(i,2),maxo1)
enddo
ll=cent
do i=cent,kk
if(x(i,2) .eq. maxo1) goto 21
ll=ll+1
enddo
21 continue
rx(l,2)=ll
R(l)=rx(l,2)-rx(l,1)
centrox=rx(l,2)-R(l)/2
write(51,*)l*5,R(l)*factor
write(52,*)centrox/10
write(53,*)rx(l,1)/10,rx(l,2)/10
close(jn)
enddo
close(50)
close(51)
close(52)
close(53)
end

```

- (6) Fortran routine to obtain the mean radius. This routine needs the entrance of "ito-radiosx.dat", "ito-radiosy.dat" and the possible center for both orientations.

```

"unidor.f"

program unidor
integer,parameter :: n=1000000
integer l
real*8 :: xr1(n,2),z(n),xr2(n,2)
open(100,file='ito-radiosx.dat',status='old')
open(101,file='ito-radiosy.dat',status='old')
open(102,file='ito-RADIO.dat',status='unknown')
open(103,file='ito-RADIO.P.dat',status='unknown')
l=0
do i=1,n
l=l+1
read(100,*,end=18)(xr1(i,j),j=1,2)
read(101,*,end=18)(xr2(i,j),j=1,2)
z(i)=(xr1(i,2)+xr2(i,2))/2.0
enddo

```

```

18 continue
print*,l
do i=1,l
write(102,*)xr1(i,1)/2.0,z(i)
enddo
do i=1,l,30
write(103,*)xr1(i,1)/2.0,z(i)
enddo
close(100)
close(101)
close(102)
close(103)
end

```

- (7) With the information of the center drop radius and its center per each time, this Matlab routine relocate the original image "jpg" into a new image which its center is the geometric center of the central drop. Also, this routine increases the frame of the original picture into a square frame. Once these operation are done, the image is converted into polar coordinates; the central drop becomes a rectangle, the depletion zone and the rest of the pattern too. Now, the distance between the central drop and small droplets can be computed. This program should be copied into the same folder of the image stack in "jpg" format.

```

salidafl='dens-';
tipf='.dat';
salidafl1='R-dens-';
tipf='.dat';
frecuencia=5;
%%% Datos iniciales de centros X y Y.
CentrosX=load('ito-centrosx.dat');
CentrosY=load('ito-centrosy.dat');
umbral=load('umbrales');
recortes=load('recortes'); % revisar fecha de experimento
umbraln=umbral(1,2); % revisar fecha de experimento
recx=recortes(1,4);
recy=recortes(1,5);
factor=1.390625*500/322.58;
muestra='ito0-';
formato='.jpg';
nft=1;
inicio=1;
numfoto=20;
%numfoto=1309;
%numfoto=size(CentrosX);
%numfoto=size(CentrosX)(1); %octave
%intervalo=10
for nft=inicio:numfoto
%for nft=inicio:intervalo:numfoto
nfoto=num2str(nft);
nombre=strcat(muestra,nfoto,formato);
%I=jpgread(nombre);
I=imread(nombre);
cx=round(CentrosX(nft)+recx);
cy=round(CentrosY(nft)+recy);
% CALCULO %%%%%%
% conversiÃ³n de rx.
tiempo=(nft)*10;
dtamR=2*round(sqrt(cx^2+cy^2));
tamR=round(sqrt(cx^2+cy^2));
[tamay tamax]=size(I);
Ax=round(tamR-cx);

```

```

Ay=round(tamR-cy);
II=ones(dtamR,dtamR)*(-1);
II(Ay:tamay+Ay-1,Ax:tamax+Ax-1)=I;
clear I;
[iimax jjmax]=size(II);
xcc=round(iimax/2);
ycc=round(jjmax/2);
ima=2*ceil(iimax/2)-1;
imax=round(ima/sqrt(2));
jma=2*ceil(jjmax/2)-1;
jmax=round(jma/sqrt(2));
xc=(imax+1)/2;
yc=(jmax+1)/2;
xmac=(ima+1)/2;
ymac=(jma+1)/2;
foto1(1:ima,1:jma)=II(xcc-(ima-1)/2:xcc+(ima-1)/2,ycc-(jma-1)/2:ycc+(jma-1)/2);
angulo=2*pi;
rrrmax=0.5-eps;
N=round(rrrmax*max(jma,ima));
M=(round(angulo*rrrmax*max(jma,ima)));
desenrollada=zeros(N,M);
factorM=angulo/(M-1);
factorN=rrrmax/(N-1);
c2=1:M;
c1=1:N;
cc2=(c2-1)*factorM;
ccrad1=factorN*(c1-1);
coorccx=round(ima*ccrad1'*sin(cc2))+xmac;
coorccy=round(jma*ccrad1'*cos(cc2))+ymac;
coorccc=coorccx+ ima*(coorccy-1);
desenrollada=foto1(coorccc);
clear foto1;
[teta rx]=size(desenrollada);
dry=10; %delta en r en pixeles.
% ciclo de obtenciÃ³n de
for j1:teta-dry
foto=desenrollada(j:j+dry,:);
conta(j)=sum(sum(foto > -1));
conta1(j)=sum(sum(foto > -1 & foto < umbraln));
clear foto;
end
aspecto=(conta1./conta)';
nombre3=strcat(salidaf1,nfoto,tipf);
uuu=fopen(nombre3,'w+');
fprintf(uuu,'%1.4f\n',aspecto);
fclose(uuu);
clear aspecto;
end

```

- (8) The following Matlab routine computes the distance

```

muestra='dens-';
formato='.dat';
%%%%%%%%%%%%% Frecuencia de adquisiciÃ³n de fotos.
frecuencia=5;
factor=500*1.390625/322.58; %conversiÃ³n pixel Âtm.
%%%%%%%%%%%%% Datos iniciales de diÃ¡metros X, Y y centros.
Radios=load('-ascii','ito-RADIO.dat');
Rpixel=round(Radios(:,2)/factor);
nft=1;
inicio=4;
numfoto=size(Radios);
% clear Radios;

```

```
%%%%%%%% INICIA LECTURA DE FOTOS
uuu=fopen('ito-delta.dat','w+');
for nft=inicio:numfoto
  nfoto=num2str(nft);
  nombre=strcat(muestra,nfoto,formato);
  densi=load(nombre);
  famosadelta(nft)=sum(densi(Rpixel:1200) < 0.0047 )*factor;
  fprintf(uuu,'%1.1f %1.4f %1.4f\n',Radios(nft,1),Radios(nft,2),famosadelta(nft));
  clear densi;
end
```


Appendix B

Appendix 2: Characterization of the Condensation Chamber

As a starting work of collaboration between the laboratory of colloids and complex physics at the Science Faculty of University of Navarra and the laboratory of fluid mechanic and turbulence of Science Faculty, National University of Mexico, measurements of the flux inside a new condensation chamber made in México. The main purpose of this collaboration is to investigate from the point of view of hydrodynamics to study the flux of vapors in many situations, like the problem of the flux inside small cavity with walls at different temperature, the flux of immiscible and miscible vapors.

B.1. Characterization

The characterization of the chamber under normal conditions ($T_i < 10$ °C at the surface at flux ≈ 250 ml/min) of operation was done with complementary measurements with the hot-wire anemometry technique in the relevant regions like the zone nearby the inlets, the center of the chamber and the exits at 90° of each inlet. The hot-wire probe is made of tungsten, and it works at temperature and resistance of operation of $T_o = 250$ °C and $R_o = 8.95$ MΩ. The probe is set perpendicular with respect the surface work of the chamber and centered. This has been displaced in X and Y directions. Per position, the acquisition of the velocity values was made for one minute, it has been displaced every 2 mm. It has been proceeded with air and without to decrease the temperature of the copper plate. Also, it has been done as in a normal experiment of BF: the WV produced by bubbling air at room temperature is streamed at certain flux, and the copper plated is cooled down at ≈ 10 °C and a flow of 885 ml/min (per inlet). The results of both techniques will be correlated with the direct observation of the whole work area. A correlation of the magnitude of the velocity and the amount of accumulated water at one coordinate point is expected. The field velocity on the concentric region of 70 cm² exhibits a non symmetric velocity field (Fig. B.2 and Fig. B.3). Due to the aquarium air pump used to flow the vapors, the flow variates in the experiment of air. The flow reported for this case is 1328 ml/min.

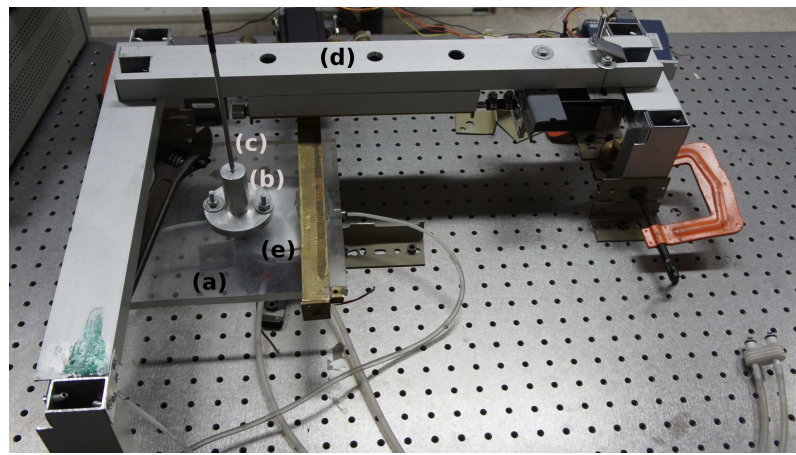


Figure B.1: (a) Support for the probe and cover of the chamber, (b) probe holder, (c) probe extension, (d) X and Y translation stage and (e) condensation chamber.

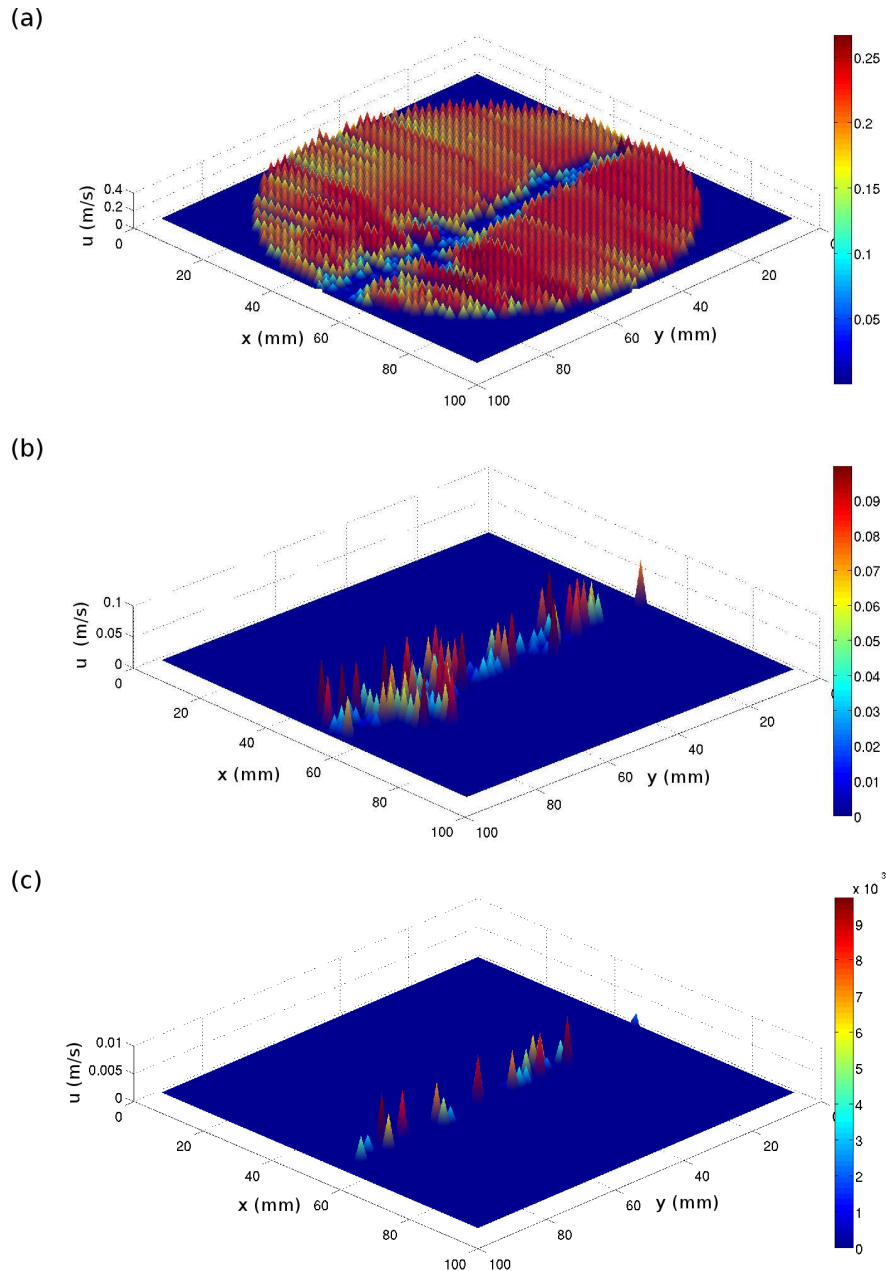


Figure B.2: (a) We can observe that the mean velocity of water vapor is more uniform in comparison with the experiment of air flow (Fig. B.3a). It is due to the water vapor density. If we think the water can have a larger density by a factor of 10^3 in comparison than air, the water vapor at room temperature is 998 Kg/m^3 and the air density is 1.2 Kg/m^3 . (b)-(c) as well, in comparison with (Fig. B.3b-c) no longer vorticity patterns on the velocity field can be observed.

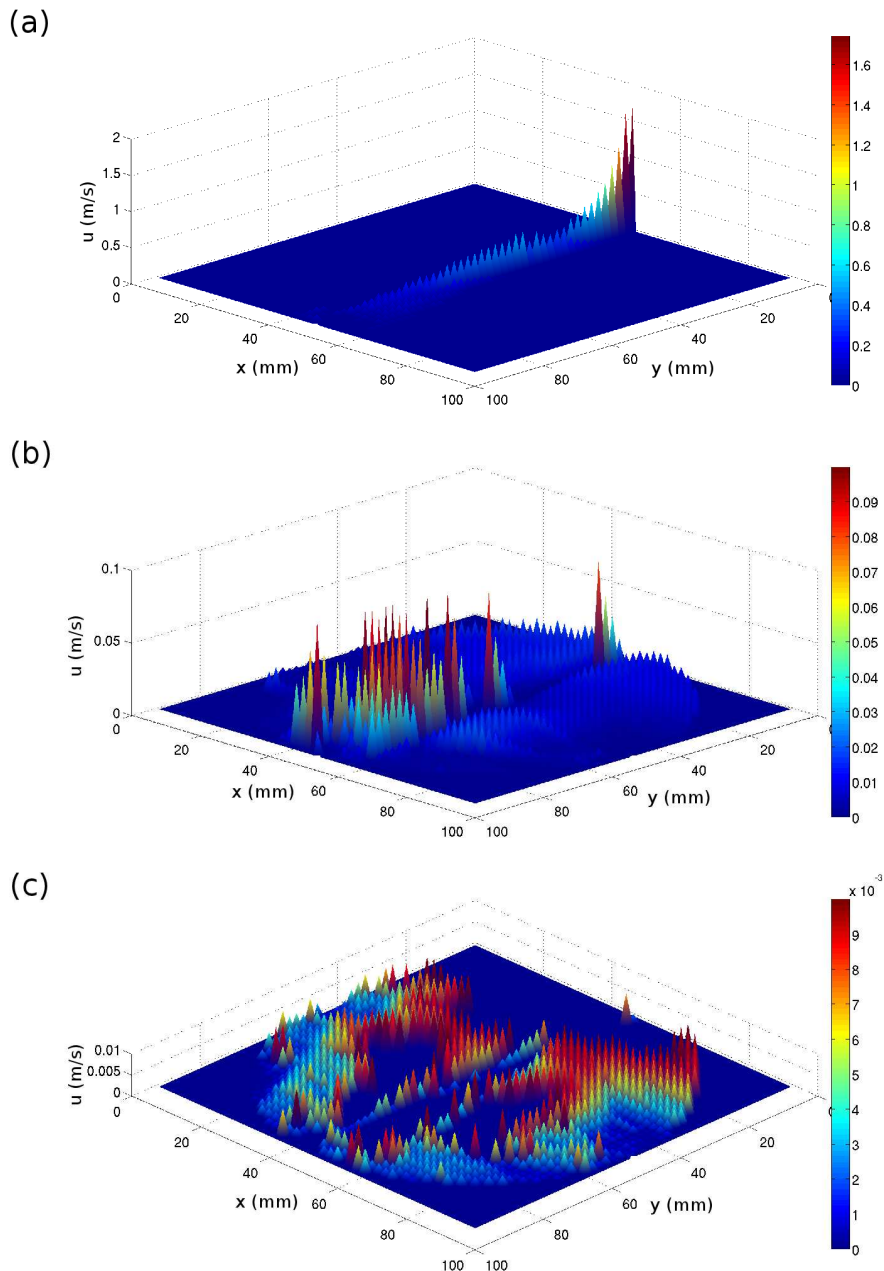


Figure B.3: The inlets are found in position (50,100) and (50,0) mm according the representation of the mean velocity field u . (a) the maximum value obtained during the measurements is 1.7 m/s. The flux is not symmetric respect to the inlets. (b) and (c) for smaller values of u , it is appreciable a region between the work area and one inlet. This region could represent vorticity.

Appendix C

Appendix 3: HVAC Diagram

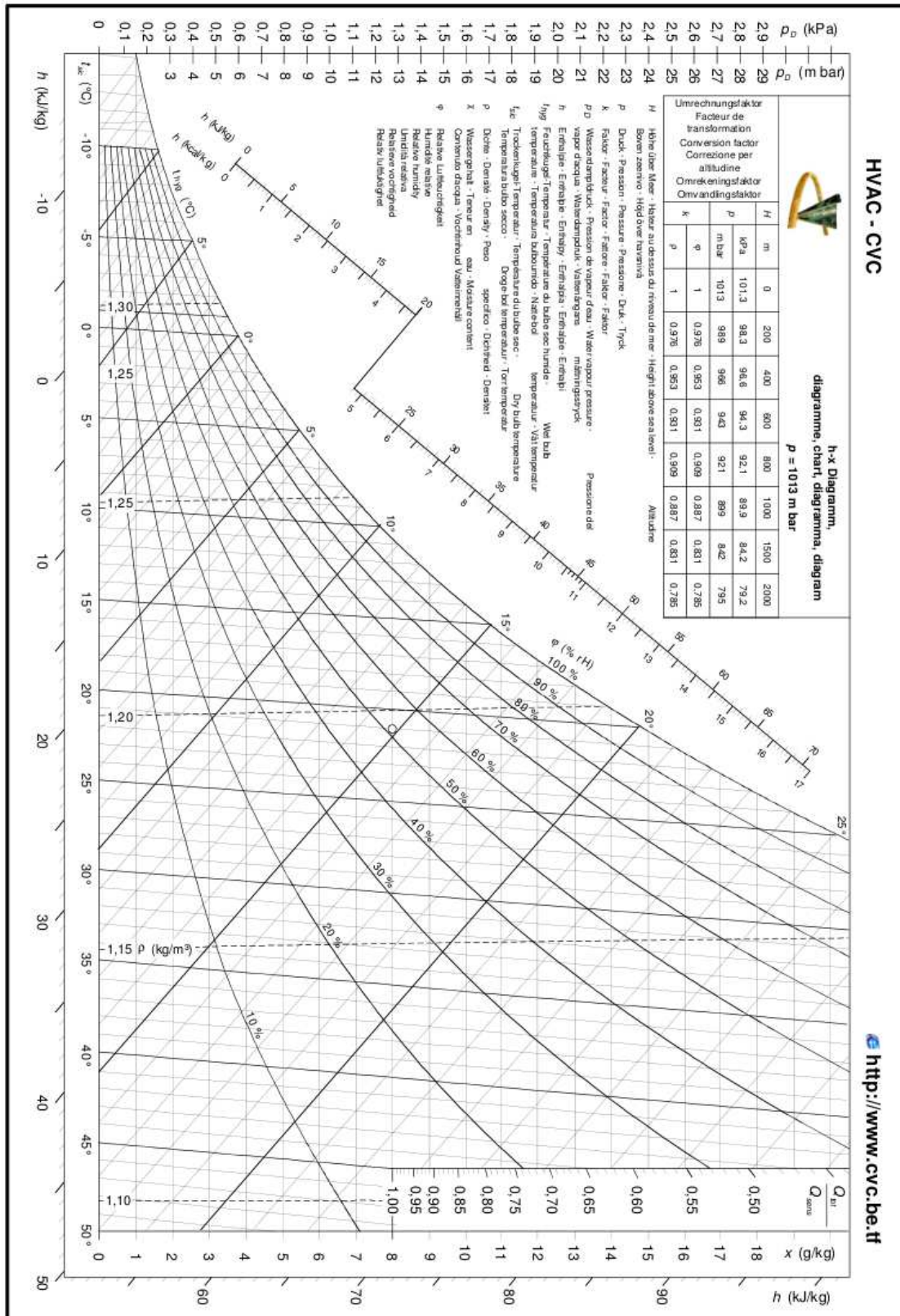


Figure C.1: This diagram shows the values of water vapor partial pressure at different temperatures [39].

Bibliography

- [1] J. Guadarrama-Cetina, R. Narhe, W. González-Viñas, D. Beysens. *Droplet pattern and condensation gradient around a humidity sink*. Submitted .
- [2] J. Guadarrama-Cetina, A. Mongruel, W. González-Viñas, D. Beysens. *Percolation-induced frost formation*. EPL (Europhysics Letters) **101** (1), (2013), p. 16009.
- [3] J. Guadarrama-Cetina, W. González-Viñas. *Breath figures of two immiscible substances on a repellent surface*. Submitted .
- [4] J. Aitken. *Breath figures*. Proceedings of the Royal Society of Edinburgh **20**, (1893), pp. 94–97.
- [5] J. Aitken. *On some nuclei of cloudy condensation*. Roy. Soc. Edin. **39**, (1898), pp. 15–25.
- [6] J. W. Giltay. *Breath figures*. Nature **(86)**, (1911), pp. 585–585.
- [7] J. Aitken. *Breath figures*. Nature **(90)**, (1913), pp. 619–621.
- [8] J. W. Rose, L. R. Glicksman. *Dropwise condensation the distribution of drop sizes*. Int. J. Heat Mass Transfer **16**, (1973), pp. 411–425.
- [9] D. Beysens. *Nucleation/nucléation*. C. R. Physique **12**, (2006), pp. 1082–1100.
- [10] D. Beysens, C. M. Knobler. *Growth of breath figures*. Phys. Rev. Lett. **57** (12), (1986), pp. 1433–1436.
- [11] F. Family, P. Meakin. *Kinetics of droplet growth processes: Simulations, theory, and experiments*. Phys. Rev. A **40** (7), (1989), pp. 3836–3854.
- [12] D. Fritter, D. Beysens. *Experiment and simulation of the growth droplets on a surface (breath figures)*. Phys. Rev. A. **43** (6), (1991), pp. 2858–2869.
- [13] J. L. Katz. *Homogeneous nucleation theory and experiment: A survey*. Pure & Appl. Chern. **64** (11), (1992), pp. 1661–1666.
- [14] A. Saito, Y. Utaka, S. Okawa, K. Matsuzawa, A. Tamaki. *Fundamental research on the supercooling phenomenon on heat transfer surfaces-investigation of an effect of characteristics of surface and cooling rate on a freezing temperature of supercooled water*. Int. J. Heat Mass Transfer **33** (8), (1990), pp. 1607–1709.
- [15] T. Hozumi, A. Saito, S. Okawa, T. Matsumura. *Effect of bubble nuclei on freezing of super-cooled water*. Int. J. of Refrigeration **25**, (2002), pp. 243–249.

- [16] A. W. Hodgson. *Homogeneous nucleation*. Advances in Colloid and Interface Science **21**, (1984), pp. 303–327.
- [17] J. F. Lutsko. *Communication: A dynamical theory of homogeneous nucleation for colloids and macromolecules*. J. Chem. Phys. **135**, (2011), pp. 1–4.
- [18] D. H. Rasmussen. *Energetics of homogeneous nucleation - approach to a physical spinodal*. J. of Crystal Growth **56**, (1981), pp. 45–55.
- [19] A. V. Korolev. *Rates of phase transformations in mixed-phase clouds*. Q. J. R. Meteorol. Soc. **134**, (2008), pp. 595–608.
- [20] K. Varanasi, T. Deng. *Spatial control in the heterogeneous nucleation of water*. App. Phys. Lett. **094101 (95)**, (2009), pp. 1–3.
- [21] K. Varanasi, N. Bhate. *Frost formation and ice adhesion on superhydrophobic surfaces*. App. Phys. Lett. **234102 (97)**, (2010), pp. 1–3.
- [22] A. Stayer, D. Beysens. *Growth of droplets on a substrate by diffusion and coalescence*. Phys. Rev. A. **44 (12)**, (1991), pp. 8271–8277.
- [23] J. D. Ford, A. Lekic. *Rate of growth of drops during condensation*. Int. J. Heat Mass Transfer **16**, (1973), pp. 61–64.
- [24] M. Sokuler, H.-J. Butt. *Dynamics of condensation and evaporation: Effect of inter-drop spacing*. EPL **89**, (1973), pp. 1–6.
- [25] D. Beysens. *The formation of dew*. Atmospheric Research **39**, (1995), pp. 215–237.
- [26] T. M. Rogers, C. Desai. *Droplet growth and coarsening during heterogeneous vapor condensation*. Phys. Rev. A **38 (10)**, (1988), pp. 5303–5309.
- [27] P. L. Krapivsky. *Growth of a single drop formed by diffusion and adsorption of monomers on a two-dimensional substrates*. Phys. Rev. E **47 (2)**, (1993), pp. 5303–5309.
- [28] J. W. Rose. *Condensation heat transfer fundamentals*. Trans. IChem. E **76**, (1998), pp. 143–152.
- [29] R. D. Narhe, D. A. Beysens, Y. Pomeau. *Dynamic drying in the early-stage coalescence of droplets sitting on a plate*. EPL **81**, (2008), pp. 1–6.
- [30] P. Meakin. *Droplet deposition growth and coalescence*. Rep. Prog. Phys. **55 (2)**, (1992), pp. 169–169.
- [31] F. Family, P. Meakin. *Scaling in the kinetics of droplet growth and coalescence: heterogeneous nucleation*. J. Phys. A: Math. Gen. **22**, (1989), pp. 225–230.
- [32] R. D. Narhe, K. P. A. M. D. Khandkar, A. V. Limaye, S. R. Sainkar, S. B. Ogale. *Difference in the dynamic scaling behavior of droplet size distribution for coalescence under pulsed and continuous vapor delivery*. Phys. Rev. Lett. **86 (8)**, (2001), pp. 1–9.

- [33] B. J. Briscoe, K. P. Galvin. *The evolution of a 2d constrained growth system of droplets-breath figures*. J. Phys. D: Appl. Phys. **23**, (1989), pp. 422–428.
- [34] B. J. Briscoe, K. P. Galvin. *Rapid communication: breath figures*. J. Phys. D: Appl. Phys. **23**, (1990), pp. 1265–1266.
- [35] B. J. Briscoe, K. P. Galvin. *Growth with coalescence during condensation*. Phys. Rev. A **43** (4), (1990), pp. 422–428.
- [36] M. Bachman. *RCA-1 Silicon Wafer Cleaning* (1999). Engineering the Microworld at The University of California, Irvine.
- [37] W. Kern, E. J. Vossen. *Thin film processes* (1978).
- [38] B. Elmar. *Microdrops Evaporating on AFM Cantilevers*, vol. 134 of *Progress in Colloid and Polymer Science*. Springer Berlin / Heidelberg (2008). 10.1007/2882_2008_084.
- [39] Unfortunately this information is not available. *HVAC-CVC*, <http://www.cvc.be.tf>.
- [40] D. R. Lide. *CRC Handbook of Chemistry and Physics*. Taylor and Francis Group LLC, 87 edn. (2007).
- [41] A. Quarteroni, F. Saleri. *Scientific computing with matlab and Octave*. Texts in computing science and engineering. Springer, 2 edn. (2006).
- [42] T. M. Inc. *Matlab, the language of technical computing* (1997).
- [43] J. S. Owens. *Condensation of water from the air upon hygroscopic crystals*. Roy. Soc. Proc. **101**, (1922), pp. 738–752.
- [44] R. Williams, J. Blanc. *Inhibition of water condensation by a soluble salt nucleus*. J. Chem. Phys. **74** (8), (1981), pp. 4675–4677.
- [45] C. Schäfle, P. Leiderer, C. Bechinger. *Subpattern formation during condensation processes on structured substrates*. Europhysics Lett. **63** (3), (2003), pp. 394–400.
- [46] D. E. Hare, C. M. Sorensen. *The density of supercooled water. ii. bulk samples cooled to the homogeneous nucleation limit*. J. Chem. Phys. **87**, (1987), pp. 40–45.
- [47] A. Angell. *Highs and lows in the density of water*. Nature Nanotechnology **2**, (2007), pp. 396–398.
- [48] A. Saito, Y. Utaka, S. Okawa, K. Matsuzawa, A. Tamaki. *Fundamental research on the supercooling phenomenon on heat transfer surfaces investigation of an effect of characteristics of surface and cooling rate on a freezing temperature of supercooled water*. Int. J. Heat Mass Trans. **33** (8), (1989), pp. 1697–1709.
- [49] J. Castaing-Lasvignottes, T. David, J.-P. Bédécarrats, F. Strub. *Dynamics modeling and experimental study of an ice generator heat exchanger using supercooled water*. Eng. Conversion and Management **47**, (2006), pp. 3644–3651.

- [50] B. Na, R. L. Webb. *A fundamental understanding of factors affecting first nucleation*. Int. J. Heat Mass Transfer **46**, (2003), pp. 3797–3808.
- [51] J. Qvist, H. Schober, B. Halle. *Structural dynamics of supercooled water from quasielastic neutron scattering and molecular simulations*. J. Chem. Phys. **134**, (2011), pp. 1–9.
- [52] D. M. Murphy, T. Koop. *Review of the vapour pressures of ice and supercooled water for atmospheric applications*. Q. J. R. Meteorol. Soc. **131**, (2005), pp. 1539–1565.
- [53] K. G. Libbrecht. *Morphogenesis on ice: The physics of snow crystals*. Eng. and Sc. **(1)**, (2001), pp. 10–19.
- [54] J. Ji, Y. Zhao, L. Guo, B. Liu, C. Jib, P. Yang. *Interfacial organic synthesis in a simple droplet-based microfluidic system*. Lab on a Chip, The Royal Society of Chemistry **12**, (2012), pp. 1373–1377.
- [55] R. G. Sardesai, D. R. Webb. *Condensation of binary vapours of immiscible liquids*. Chemical Eng. Science **34** **(4)**, (1982), pp. 529–537.
- [56] O. Tutkun. *Condensation of vapours of binary immiscible liquids*. Chem. Eng. and Processing **32**, (1993), pp. 263–212.
- [57] V. D. Rao, V. M. Krishna, K. Sharma, P. M. Rao. *Convective condensation of vapor in the presence of a non-condensable gas of high concentration in laminar flow in a vertical pipe*. Int. J. of Heat. and Mass Transfer **51**, (2008), pp. 6090–6101.
- [58] P. Borckmans, G. Dewel, A. de Wit, E. Dulos, J. Boissonade, F. Gauffre, P. de Kepper. *Diffusive instabilities and chemical reactions*. Int. J. of Bifurcation and Chaos **12** **(11)**, (2002), pp. 2307–2332.
- [59] U. Heiko, F. Bunz. *Breath figures as a dynamic templating method for polymers and nano-materials*. Adv. Mater. **18**, (2006), pp. 973–989.
- [60] R. Kofman, M. Allione, F. Celestini, Z. Barkay, Y. Lereah. *Preparation and analysis of a two-components breath figure at the nanoscale*. Eur. Phys. J. D **50**, (2008), pp. 279–284.
- [61] J. Rayleigh. *Breath figures*. Nature **2174** **(86)**, (1911), p. 416.
- [62] T. J. Baker. *Breath figures*. Philos. Mag. **44**, (1922), p. 752.
- [63] B. Lewis, J. Anderson. *Nucleation and Growth of Thin Films*. Academic London, 87 edn. (1978).
- [64] A. Steyer, P. Guenoun, D. Beysens. *Spontaneous jumps of droplet*. Phys. Rev. Lett **68** **(1)**, (1992), pp. 64–66.
- [65] B. J. Briscoe, K. P. Galvin. *The evolution of a 2d constrained growth system of droplets-breath figures*. J. Phys. D: Appl. Phys. **23** **(68)**, (1990), pp. 422–428.

Summary

We present experimental observations of Breath Figures (BF) which are formed by the dew of water when it condenses on a cold surface. The experiments were done in specific conditions and configurations of temperature, surfaces and mixes in controlled concentration of miscibles and immiscibles substances like the salt saturated solution, alcohol and silicon oil ($C_6H_{18}O_2Si$). The hydrophobic surfaces used on those observations are thin glasses coated with ITO (Indium Tin Oxide), 3M ECG-1700 which is repellent to the silicon oil too, and silane which is hydrophobic. Those observations let us to perform direct geometrical measurements of the droplets like radii r , areas a and with the values of contact angle θ the volume V that form the Breath Figures. Other indirect measurements obtained from the direct measurements are the factor occupation ϵ^2 , the values of concentration of water once it has condensed over a cold surface t_c^{-1} , and when it changes from liquid phase to solid phase and when the BF takes part in a process of deposition, also the fractal dimension of the BF pattern to characterize the geometrical properties in a liquid phase and solid phase. Once the average of direct measurements are obtained we extract laws of growth and the evolution of the phenomena a how outward factors modify the achievement of the process of condensation and what is the observable pattern result.

Resumen

Presentamos observaciones experimentales del fenómeno figuras de aliento (ó BF por Breath Figure) el cual se forma por el rocío de agua cuando esta condensa en una superficie fría. Se han hecho experimentos con condiciones y configuraciones específicas de temperatura, superficies y concentraciones de mezclas de sustancias miscibles e inmiscibles como una solución saturada de sal, alcohol y hexametildisiloxano ($C_6H_{18}O_2Si$). Las superficies hidrofóbicas utilizadas en las observaciones son vidrios recubiertos con óxido titanio e indio, 3M ECG-1700 el cual es repeLENte al hexametildisiloxano también, así como el silano también tiene propiedades hidrofóbicas. Estas observaciones nos permiten llevar acabo mediciones directas de la geometría de gotas, como el radio r y el área a , ángulos de contacto θ y volúmenes V que forman los Breath Figures. Otras medidas indirectas son obtenidas de mediciones directas son el factor de ocupación ϵ^2 , los valores de concentración de agua una vez ha condensado sobre la superficie t_c^{-1} , y cuando esta cambia de fase líquida a sólida y cuando el BF toma parte en el proceso de deposición, también la dimensión fractal de los patrones del BF que caracterizan sus propiedades geométricas en la fase líquida o sólida. Una vez que se ha obtenido el promedio de mediciones directas se esxtraen leyes de crecimiento y la evolución de los fenomenos y como factores externos modifican el desempeño del proceso y las observables del patrón resultante.

